Workshop of
CODE_BRIGHT USERS

4 May 2022
Barcelona, Spain
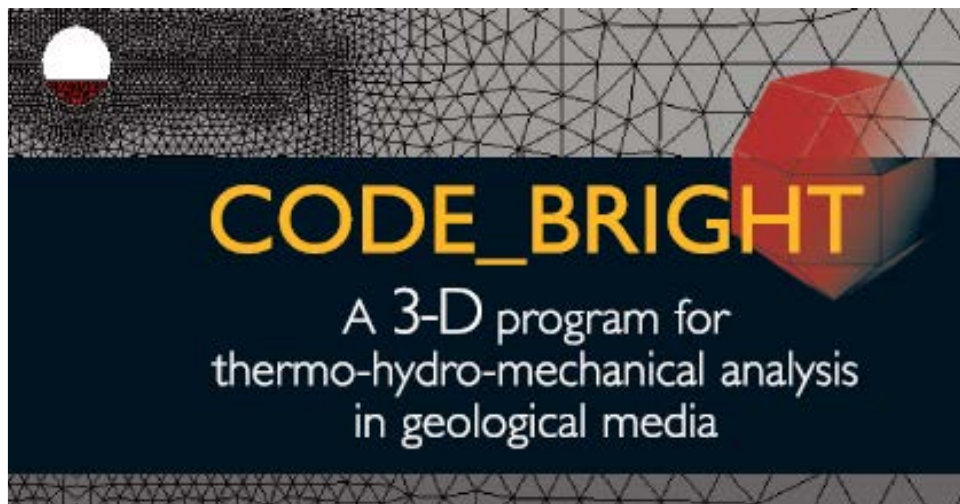
CODE_BRIGHT
A 3-D program for
thermo-hydro-mechanical analysis
in geological media

Department of Civil and Environmental Engineering
UPC-BarcelonaTech
Barcelona, Spain

CIMNE
International Center for Numerical Methods in Engineering
Barcelona, Spain

CODE_BRIGHT

A 3-D program for thermo-hydro-mechanical analysis in geological media

WORKSHOP OF CODE_BRIGHT USERS
Barcelona, 4 May 2022

Department of Civil and Environmental Engineering
(UPC-BarcelonaTech, Barcelona, Spain)

CIMNE
(International Center for Numerical Methods in Engineering,
Barcelona, Spain)

CONTENTS

THM PHENOMENA IN ANISOTROPIC HETEROGENEOUS POROUS MEDIA: FORMULATIONS AND APPLICATION

Yunfeng Zhou[*], **Alfonso Rodriguez-Dono**[*] **and Sebastia Olivella**[*]

[*] Department of Civil and Environmental Engineering
Universitat Politècnica de Catalunya (UPC)
Campus Nord UPC, 08034 Barcelona, Spain

Keywords: Anisotropic heterogeneous model, gas migration, thermo-hydro-mechanical modelling, preferential pathways, CODE_BRIGHT.

Abstract. *The formulation of an* anisotropic *heterogeneous model is introduced. A gas injection simulation is performed considering thermo-hydro-mechanical properties of the rock mass. A matrix decomposition technique is adopted to generate a structured and random field of porosity. The model has been implemented in the Finite Element Method software CODE_BRIGHT. Preliminary results are presented.*

1 INTRODUCTION

Subsurface porous materials typically exhibit a large degree of natural variability in terms of their type and spatial distribution [1]. Geostatistical methods [2] are usually applied to quantify such uncertainty. These methods are optimal when data are normally distributed and stationary (mean and variance do not vary significantly in space) [3]. Algorithms to simulate a gaussian and stationary field can be classified into two categories: exact and approximate ones [4]. Semi-variogram is used to characterize spatial correlation [3]. Exact algorithms can reproduce the semi-variogram precisely, and the LU triangular decomposition approach is one of them [5].

2 MODEL DESCRIPTION

2.1 Isotropic heterogeneous model [5]

If C is the covariance matrix of N_1 grid points to simulate. It is positive-definite and can be decomposed into upper and lower triangular matrices (Cholesky algorithm).

$$C = L \cdot U \text{ with } L = U^T \tag{1}$$

ω is a vector of N_1 independent normally distributed random numbers. The vector y can be defined as:

$$y = L \cdot \omega \tag{2}$$

The mean and covariance of the random variable Y corresponding to y are obtained:

$$E(Y) = 0 \tag{3}$$

$$Cov(Y) = E(L\omega(L\omega)^T) = L \cdot E(\omega\omega^T) \cdot U = C \tag{4}$$

Under the condition of second-order stationarity (spatially constant mean and variance), the relationship between the covariance function and semi-variogram can be given by:

$$C(h) = C(0) - \gamma(h) \tag{5}$$

If the spherical covariance model is adopted below:

$$C(\boldsymbol{h}) = \begin{cases} C_0 + C_1, & |\boldsymbol{h}| = 0 \\ C_1\left[1 - 1.5\dfrac{|\boldsymbol{h}|}{a} + 0.5\left(\dfrac{|\boldsymbol{h}|}{a}\right)^3\right], & 0 < |\boldsymbol{h}| \leqslant a \\ 0, & |\boldsymbol{h}| > a \end{cases} \tag{6}$$

Where C_0 is the nugget, which is due both to measurement errors and to micro-variabilities of the mineralization; a denotes the range, which means that any data value will be correlated with any other value falling within a radius a (as shown in Figure 1 (a)); $|\boldsymbol{h}|$ is the distance between two elements.

(a)   **(b)**
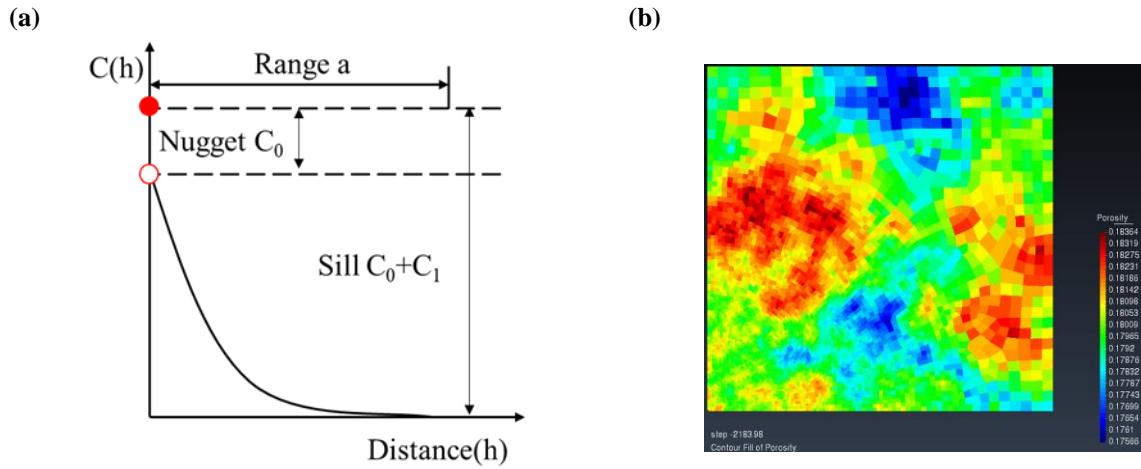
Figure 1 (a) Schematic of the covariance model; (b) An example of isotropic heterogeneous random field

Then, vector y is therefore the autocorrelated simulation with the covariance matrix C.

If a random field for porosity (ϕ) (Figure 1 (b)) is generated with the mean m and covariance C, and the range is a, it can be derived by:

$$\phi = y + m \tag{7}$$

The mean and covariance are given by:

$$E(\phi) = m, \ Cov(\phi) = C \tag{8}$$

2.2 Anisotropic heterogeneous model [6, 7]

The phenomenon is said to be "anisotropic", when the covariance function $C(\boldsymbol{h})$ depends on both the modulus and the direction of vector $\boldsymbol{h}$ [8]. The directional graph of the ranges a is an ellipsoid in three dimensions. It is isotropic if the covariance function depends on the modulus of vector $\boldsymbol{h}$. There are two main types of anisotropy: A geometric anisotropy is the one that has approximately the same sill but different ranges; A zonal anisotropy is one in which the sill value changes with direction while the range remains constant [9]. The latter type can be considered as a particular case of the former one [6], so the geometric anisotropy is introduced in detail.

Two steps are taken to obtain the anisotropic covariance function since the isotropic one has already shown in Eq. (6), which means transforming an ellipsoid into a sphere. The first step is to rotate the coordinate axes by the angle α, β, and γ (Figure 2) so that they become parallel to the main axes of the ellipsoid. The transformation is

$$\begin{bmatrix} h_{x\alpha ni1} \\ h_{y\alpha ni1} \\ h_{z\alpha ni1} \end{bmatrix} = [R] \begin{bmatrix} h_{x\alpha ni} \\ h_{y\alpha ni} \\ h_{z\alpha ni} \end{bmatrix} \tag{9}$$

$$with\ [R] = \begin{bmatrix} 1 & 0 & 0 \\ 0 & \cos(\beta) & \sin(\beta) \\ 0 & -\sin(\beta) & \cos(\beta) \end{bmatrix} \begin{bmatrix} \cos(\gamma) & 0 & \sin(\gamma) \\ 0 & 1 & 0 \\ -\sin(\gamma) & 0 & \cos(\gamma) \end{bmatrix} \begin{bmatrix} \cos(\alpha) & \sin(\alpha) & 0 \\ -\sin(\alpha) & \cos(\alpha) & 0 \\ 0 & 0 & 1 \end{bmatrix}$$

Where $h_{x\alpha ni1}$, $h_{y\alpha ni1}$, and $h_{z\alpha ni1}$ represent the separation distances along the coordinate axis in the new coordinate system; In matrix $[R]$, from left to right, are rotations around the axis x, y and z.

Next is to transform the ellipsoid into a sphere with a radius equal to the major range (major range a_x shown in Figure 2) of the ellipsoid. This is achieved by multiplying the Eq. (9) in step one by the ratio of anisotropy matrix

$$\begin{bmatrix} h_{xiso} \\ h_{yiso} \\ h_{ziso} \end{bmatrix} = [\lambda][R] \begin{bmatrix} h_{x\alpha ni} \\ h_{y\alpha ni} \\ h_{z\alpha ni} \end{bmatrix} with\ [\lambda] = \begin{bmatrix} 1 & 0 & 0 \\ 0 & \lambda_1 & 0 \\ 0 & 0 & \lambda_2 \end{bmatrix} \tag{10}$$

Where $\lambda_1 = a_x/a_y$, $\lambda_2 = a_x/a_z$, a_x, a_y, and a_z are range for axis x, y, and z, respectively;

Substitute Eq. (10) into Eq. (6), the anisotropic heterogeneous random field is obtained (Figure 4(a)).
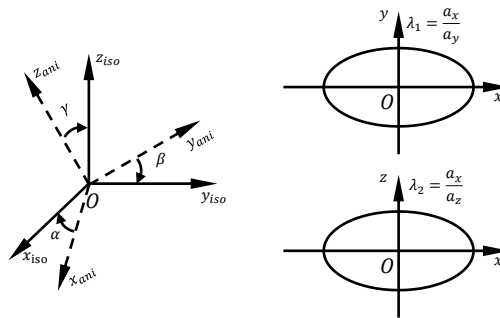
Figure 2 An example of the five parameters needed to define the geometric anisotropy of a covariance function in 3D.

2.3 Generation of thermos-hydro-mechanical random fields

In CODE_BRIGHT, many parameters are functions of porosity. These parameters inherit the anisotropic heterogeneous properties automatically after the generation of random porosity field. They are listed in Table 1.

Parameters		Formulations
Thermal conductivity	λ	$\lambda = \lambda_{sat}^{S_l} \lambda_{dry}^{1-S_l}$, with $\lambda_{dry} = \lambda_s^{1-\phi} \lambda_g$, $\lambda_{sat} = \lambda_s^{1-\phi} \lambda_l$
Intrinsic permeability	k	$k_1 = k_0 \dfrac{(1-\phi_0)^2}{\phi_0^3} \dfrac{\phi^3}{(1-\phi)^2}$, $k_2 = k_0 \exp(b(\phi - \phi_0))$
Capillary pressure	P_c	$P_c = P_0 \exp(b(\phi_0 - \phi))$ if k_2 is used
Retention curve	S_e	$S_e = \left(1 + \left(\dfrac{P_g - P_l}{P_c}\right)^{\frac{1}{1-\lambda_c}}\right)^{-\lambda_c}$
Diffusive flux	$\boldsymbol{i}_f$	$\boldsymbol{i}_f = -(\phi \rho_f S_f \tau D_m \boldsymbol{I}) \nabla \omega_f$
Cohesion	c	$c(\phi) = \dfrac{(a + bs)(f(\phi) + |f(\phi)|)}{2}$ with $f(\phi) = 1 - \left(\dfrac{\phi}{\phi_0}\right)^n$

Table 1 Lists of thermos-hydro-mechanical parameters in CODE_BRIGHT.
Where ϕ and ϕ_0 are porosity and reference porosity, respectively.

2.4 Model geometry and boundary conditions

Figure 3 shows the model geometry and boundary conditions in four stages. Stage 0 is the one for equilibrium, followed by the excavation of a borehole. Temperature is imposed on the borehole wall in stage 1. The interval is installed as a filter in stage 2. In the next stage, gas is injected through the interval to the rock mass.

An anisotropic heterogeneous domain is generated. Its average initial porosity is 0.18 with standard deviation 0.0017. The range is selected as the half length of the domain (5m).
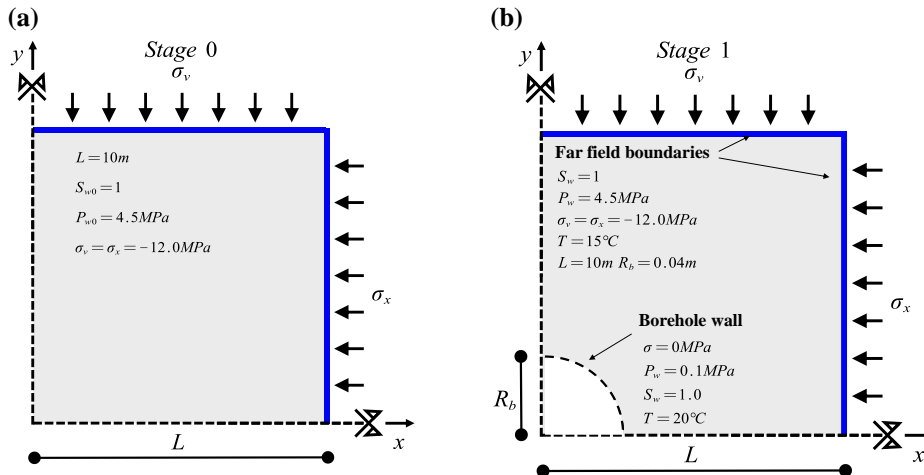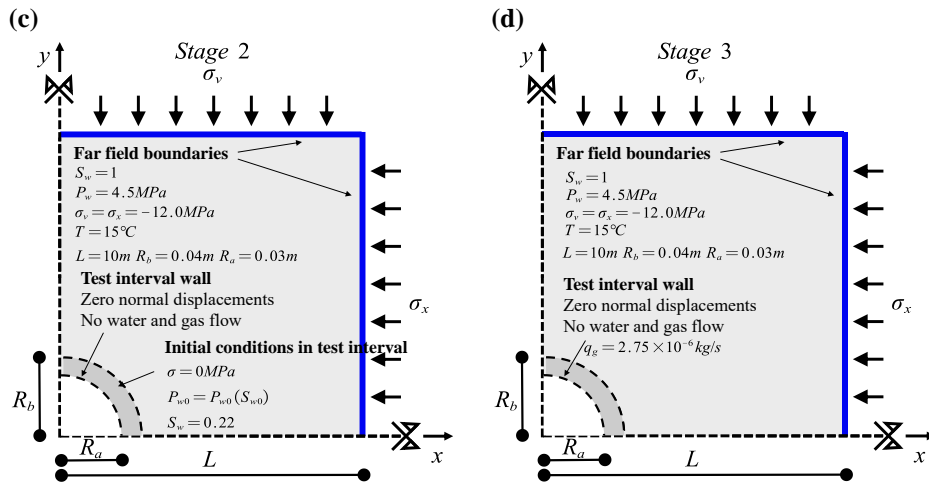
Figure 3 Four stages for the gas injection test.

3 RESULTS

Initial porosity distribution

Final porosity distribution

Gas pressure distribution in the final state

Temperature distribution in the final state
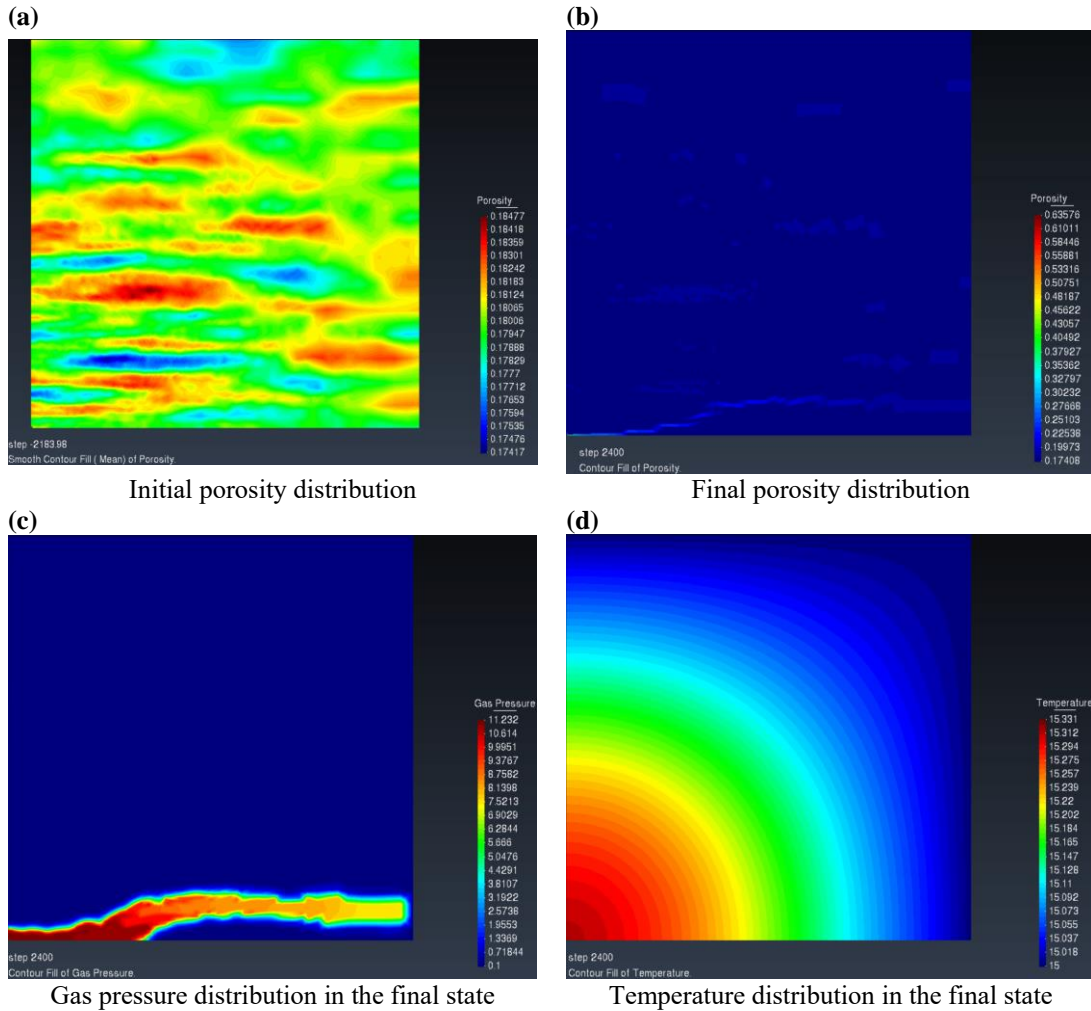
Figure 4 simulation results for porosity, gas pressure and temperature.

Figure 4(a) shows the initial porosity distribution, which is an anisotropic heterogeneous domain. The porosities become larger acting as gas migration channels as shown in Figure

5

4(b). Figure 4(c) presents the gas pressure distribution of the final time step. Gas diffusion takes place in the gas front, and microfractures (Figure 4(b)) are generated afterwards. Preferential pathways appear due to higher porosities in the horizontal beddings. In Figure 4(d), there is no obvious temperature heterogeneity in this case.

4   CONCLUSIONS

- A preliminary study of gas migration simulation has been performed.
- A spatially anisotropic heterogeneous filed can be generated automatically in CODE_BRIGHT, which provides a possible tool to study issues with heterogeneity combined with anisotropy.
- Anisotropic heterogeneous porosity domains can lead to "fingered" gas/water displacement front because gas flows into locations with higher permeabilities.

REFERENCES

1. Tompson, A.F. and L.W. Gelhar, *Numerical simulation of solute transport in three‐dimensional, randomly heterogeneous porous media.* Water Resources Research, 1990. **26**(10): p. 2541-2562.
2. Matheron, G., *The Theory of Regionalized Variables and Its Applications*. 1971: École national supérieure des mines.
3. Bohling, G., *Introduction to geostatistics and variogram analysis.* Kansas geological survey, 2005. **1**(10): p. 1-20.
4. Emery, X. and C. Lantuéjoul, *TBSIM: A computer program for conditional simulation of three-dimensional Gaussian random fields via the turning bands method.* Computers & Geosciences, 2006. **32**(10): p. 1615-1628.
5. Alabert, F., *The practice of fast conditional simulations through the LU decomposition of the covariance matrix.* Mathematical Geology, 1987. **19**(5): p. 369-386.
6. Deutsch, C.V. and A.G. Journel, *Geostatistical software library and user's guide.* New York, 1992. **119**(147).
7. Liu, W.F. and Y.F. Leung, *Characterising three-dimensional anisotropic spatial correlation of soil properties through in situ test results.* Géotechnique, 2018. **68**(9): p. 805-819.
8. Journel, A.G. and C.J. Huijbregts, *Mining Geostatistics*. 1978. 600p.
9. Isaaks, E.H., et al., *Applied Geostatistics*. 1989: Oxford University Press.

LABORATORY AND NUMERICAL ANALYSIS FOR THE SIMULATION OF CRUSHED SALT COMPACTION BEHAVIOR

Larissa Friedenberg [*], Oliver Czaikowski[*], Svetlana Lerche[†]

[*] Gesellschaft für Anlagen- und Reaktorsicherheit (GRS) gGmbH
Theodor-Heuss-Straße 4, 38122 Braunschweig, Germany
E-mail: larissa.friedenberg@grs.de , web page: www.grs.de

[†] Institute of Mineral and Waste Processing, Waste Disposal and Geomechanics
Chair for Waste Disposal Technologies and Geomechanics
Clausthal University of Technology
Erzstraße 20, 38678 Clausthal-Zellerfeld, Germany

Abstract. *The paradigm changes in the safety case for a repository of heat-emitting radioactive waste in Germany and the necessity of a qualified prognosis of its long-term behavior result in extended requirements regarding the understanding and modelling of crushed salt compaction behavior for a possible repository in rock salt. In the current state, some uncertainties with respect to the existing database and process understanding still remain, especially for the numerical modelling of the crushed salt compaction process.*

This paper presents an insight in a PhD work with the objective to improve the numerical simulation of crushed salt compaction with CODE_BRIGHT. First, the role of crushed salt and the necessity of process understanding in its entirely are described. Then the methodological approach is outlined and mainly a re-simulation of a triaxial compaction test on crushed salt is shown.

1 INTRODUCTION

Rock salt is considered as a possible host rock formation for the deep geological disposal of heat-emitting radioactive waste in Germany. The safety concept of a repository in rock salt is based on a multibarrier system including the geological barrier salt, geotechnical seals and the backfill material. Immediately after disposal, the sealing function will be provided by the waste matrix, waste casks and geotechnical barriers. In the long-term, the sealing function will be given by the rock salt as geological barrier and the backfilling of open cavities and shafts with crushed salt.

Crushed salt will be used as long-term stable backfilling material due to its favorable properties and its easy availability (mined-off material). The compaction of crushed salt is driven by the creep of the surrounding rock salt resulting in natural compaction by convergence. It is expected that the porosity and permeability of crushed salt decrease during compaction down to barrier properties comparable to undisturbed rock salt (≤ 1 %).

A qualified prognosis of the long-term behavior of crushed salt is needed, which results in a comprehensive understanding of the compaction behavior involving several thermo-hydro-mechanical (THM) coupled processes[i,ii,iii]. Compaction behavior is influenced by internal properties, like grain size distribution, mineralogy and humidity, as well as boundary conditions such as temperature, compaction rate or stress state. In the current state, some

uncertainties with respect to database and process understanding still remain, especially for the numerical reproduction of crushed salt compaction processes.

2 PROCEDURE

The methodological approach for an improvement of crushed salt compaction process understanding is characterized by a combination of systematically structured laboratory studies with uniform reference material as well as with isolated observation of different influencing factors and numerical investigations with application and analysis of the database generated in this way. First, the existing and well documented database about crushed salt was studied with the aim of carving out laboratory tests suitable for the investigation process. The experiments were chosen considering the complex compaction behavior of crushed salt which is influenced by several parameters like material properties as well as boundary conditions (Table 1).

Internal properties	Boundary conditions	
• Grain size distribution	• Temperature	• Stress state
• Mineralogy	• Compaction rate	o Isotropic stress path
• Humidity	• Pre-compaction	o Deviatoric stress path
• Porosity (compaction state)	- Load pre-history	o Stress type/geometry

Table 1: Influencing factors on crushed salt compaction[ii]

In this paper, the focus lies on the numerical modelling of the triaxial test "TUC-V2" which was performed by the Clausthal University of Technology (TUC)[ii] in the framework of the previous mentioned laboratory program. The handling of the influencing factors within the numerical approach was considered and compared to the laboratory results.

3 NUMERICAL APPROACH

The TUC-V2 triaxial test was executed by the Clausthal University of Technology (TUC) using the KOMPASS reference material. It was started within the KOMPASS-I project and is still running within the KOMPASS-II project. Primarily, the test was planned for the isolated investigation of the influence of the isotropic as well as of the deviatoric stress on viscous volumetric deformations and the influence of porosity on viscous volumetric deformations and viscous shear deformations[ii], however, the test was extended for investigation of long term behavior, thermal influence and expansion of the observed area for the investigated influencing factors. Here, only the first 150 days of the test are considered (phase I), and the loading history is shown in Figure 1. It contains 5 loading stages with variations between isotropic and deviatoric phases. For the simulation, an axially symmetrical model was chosen (Figure 1). The initial parameter for the TUC-V2 sample which are directly derived from laboratory measurements are presented in Table 2 and are adapted in the numerical model exactly. The simulation was performed as an isothermal HM-coupling, since temperature was held constant during the considered 150 days. The hydraulic aspects were included, since liquid saturation is increasing in the sample with decreasing porosity and also the FADT mechanism should be considered. The moisture content in the experiment is quite low, however, it was chosen corresponding to the in-situ relevant conditions in Germany.

2
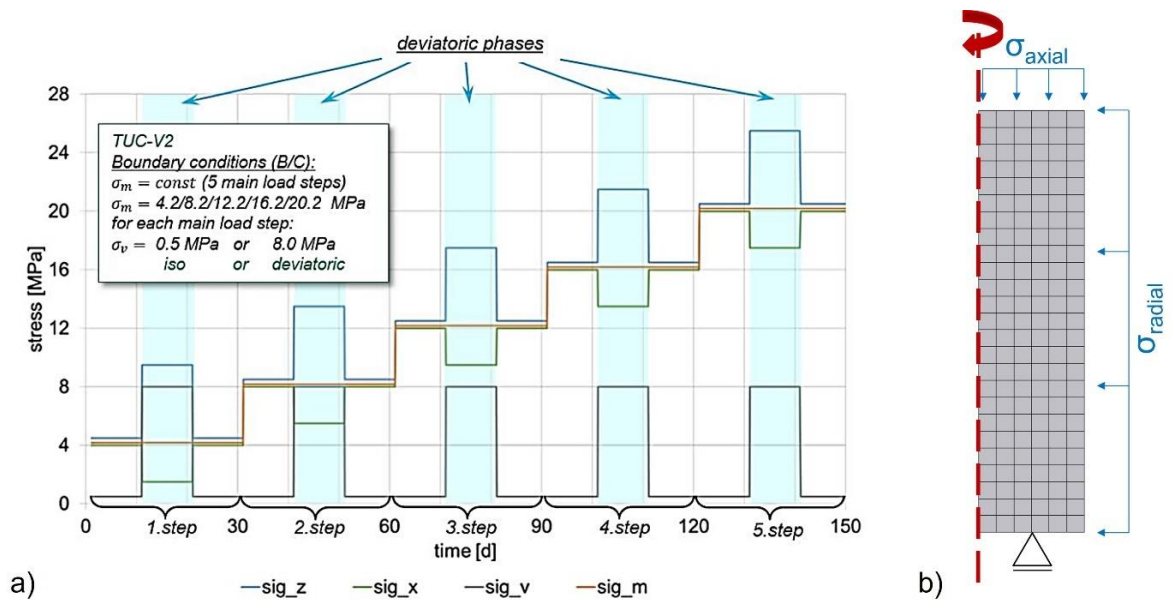
Figure 1: Multi-stage long-term test TUC-V2. a) Loading history. b) Numerical model[ii]

Parameter	Unit	Value
H	mm	180
D	mm	90.1
Φ	-	16.7
w	%	0.5
T	°C	30

Table 2: Initial parameter for the TUC-V2 sample derived in laboratory[ii]

For the numerical modelling CODE_BRIGHT is applied using the models for crushed salt which are described by an additive approach of elastic, creep and viscoplastic strain rates[iv]. The creep part covers two mechanisms: fluid assisted diffusional transfer (FADT) and dislocation creep (DC) which allows to simulate humidity creep, as well as mechanisms described by dislocation theory.

Since no numerical parameter set exists for the KOMPASS reference material[ii] yet, first, parameter which could be derived from the crushed salt material itself were adapted. For the parameter which could not be adapted from the material, initial values were taken from a previous simulation of a triaxial test with Asse mine material ("Speisesalz", As z2SP) ("Initial" parameter set). With these initial parameters the measurements couldn't be reproduced, because the compaction process was underestimated especially in the first 60 days of testing (Figure 2).

Therefore, the influence of the various material parameters in the mechanical constitutive equations was studied and identified due to the sensitivity analysis and parameter improvement was performed. As a result, an "Interim" parameter set was compiled, representing the compaction behavior quite well regarding the porosity within the first 70 days of the test (Figure 2). However, with ongoing testing time, the compaction rate is strongly underestimated with this parameter set. Further parameter adjustment was performed by improving the pre-exponential parameter A_A in the DC model. Actually, A_A is derived directly from the specification of creep class for salt material (creep class 6, A_A = 2.08e-6), however, in this case the value was not representative for modelling the compaction behavior

and therefore was changed in the "Final" parameter set corresponding to creep class 8 (A_A = 1.25e-5).
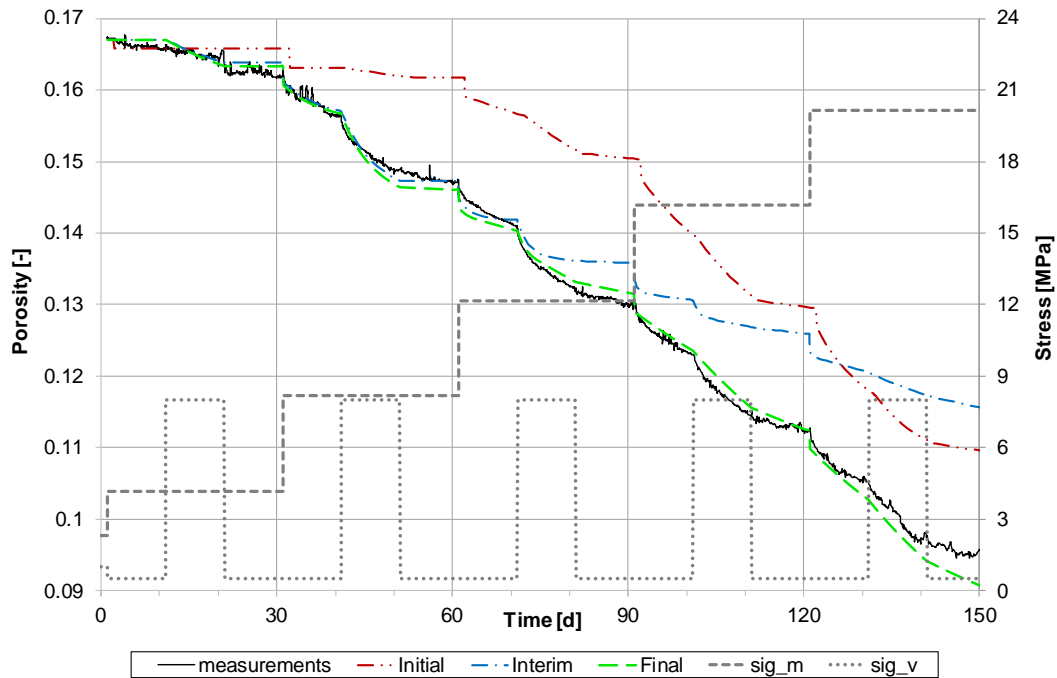
Figure 2: Porosity and stress evolution for the TUC-V2 test. Comparison of measurements[ii] and numerical results. Red: Initial parameter set, blue: interim parameter set, green: final parameter set.

In general, the porosity decrease could be reproduced quite well using the final parameter set (Figure 2), however, a consideration of the volumetric strain rate shows differences between the numerical values and the laboratory data. Figure 3 shows a good reproduction for the parameter sets "Interim" and "Final" for the first 60 days of the test. Up to 60 days, the accordance between laboratory data and these two parameter sets is getting worse. The simulation with the initial parameter set shows very large deviations to the measurements until 60 days, however, when studying the detail in Figure 4 a nice accordance between the initial parameter set and the measurements can be observed for the load levels and for the porosity range presented here. In particular, the tendency in the decreasing of the porosity over time in the red curve is to be considered as best fitting in this area in comparison to the other two alternative parameter sets.

The results from the numerical simulation of the TUC-V2 test show that with ongoing compaction the reproduction of the volumetric strain rate in the numerical model is deviating from the measurements. Due to the low moisture content of the crushed salt specimen, the influence of hydraulic processes might be very low and therefore, the issue of the compaction process lies in the mechanical part. In this frame, it is not yet clear at which porosities the liquid saturation becomes the threshold where the FADT mechanism is the dominating creep process.

Next meaningful steps for the improvement of the calculations may be:
- Further optimization of the parameter set due to combination of the advantages of the "initial" and "final" sets
- Involving additional information in form of the measurements from the further phases of the test TUC-V2 and thus extending the validity of the determined parameter set
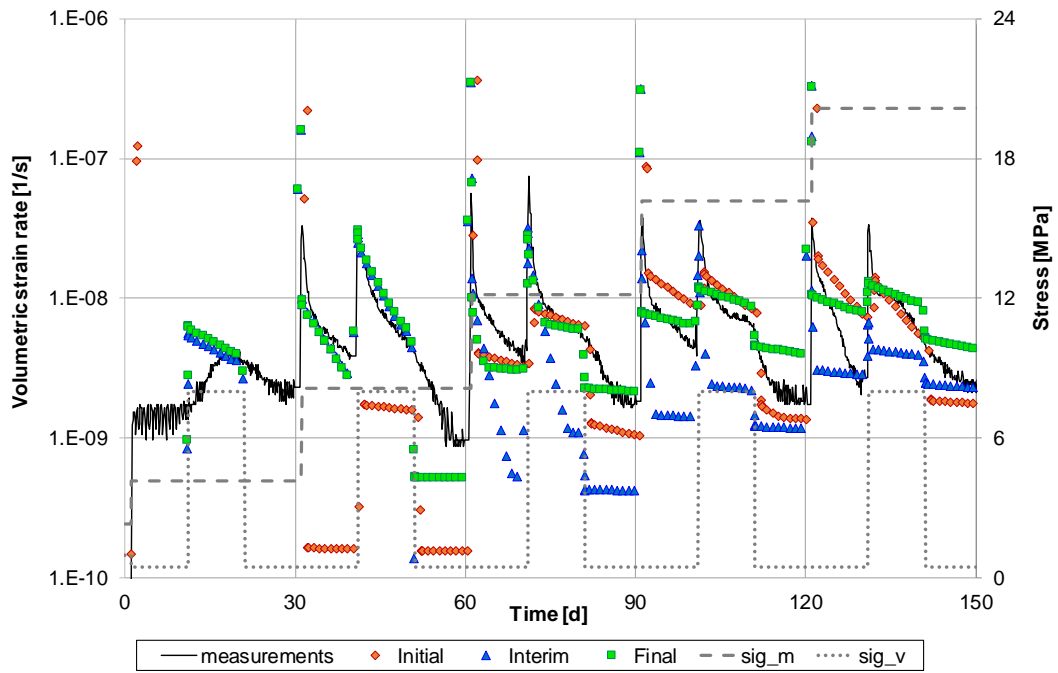
Figure 3: Volumetric strain rate and stress evolution for TUC-V2. Comparison of measurements[ii] and numerical results.
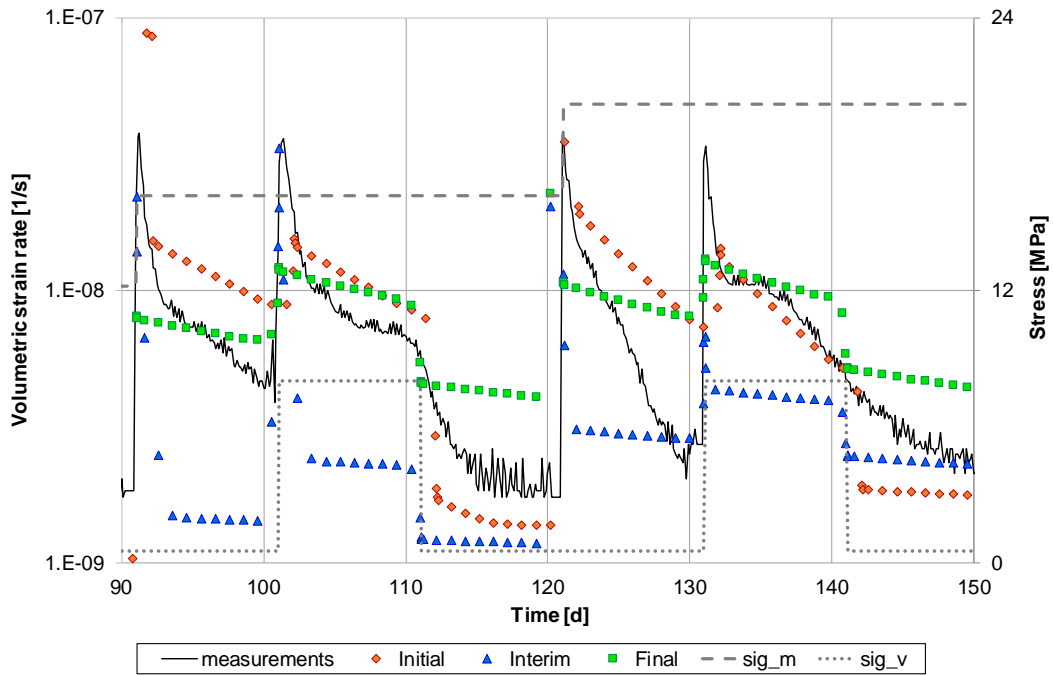
Figure 4: Detail of volumetric strain rate and stress evolution for the testing time between 90 days and 150 days. Comparison of measurement[ii] and numerical results.

4 CONCLUSIONS

The paper presents a re-simulation of the triaxial compaction test TUC-V2 on crushed salt. In general, the porosity decrease could be reproduced quite well, however, for a detailed investigation of the strain rate, deviations between the numerical results and the measurement data could be observed. In the further procedure, reasons for the deviations should be carved out by combining laboratory studies with numerical modelling.

REFERENCES

[i]   Hansen, F.D., Popp, T., Wieczorek, K., Stührenberg, D., 2014. Granular Salt Summary: Reconsolidation Principles and Applications. Fuel Cycle Research & Development, FCRD-UFD-2014-000590. SAND2014-16141R.

[ii] KOMPASS-I, 2020. Czaikowski, O., Friedenberg, L., Wieczorek, K., Müller-Hoeppe, N., Lerch, Ch., Eickemeier, R., Laurich, B., Liu, W., Stührenberg, D., Svensson, K., Zemke, K., Lüdeling, Ch., Popp, T., Bean, J., Mills, M., Reedlunn, B., Düsterloh, U., Lerche S., Zhao, J. Compaction of crushed Salt for the safe Containment. KOMPASS project. Gesellschaft für Anlagen- und Reaktorsicherheit (GRS) gGmbH, GRS-608, Köln.

[iii] Kröhn, K.P., Stührenberg, D., Herklotz, M., Heemann, U., Czaikowksi, O., Wieczorek, K., Müller, Ch., Zhang, C.-L., Moog, H., Schirmer, S., Friedenberg, L., 2017. Mechanical and hydraulic behaviour of compacting crushed salt backfill at low porosities. GRS-450. Gesellschaft für Anlagen- und Reaktorsicherheit (GRS) gGmbH, Köln.

[iv] Olivella, S., Vaunat, J., Rodriguez-Dono, A., 2021. CODE_BRIGHT 2021. User's Guide. Universitat Politècnica de Catalunya, Department of Civil and Environmental Engineering, Division of Geotechnical Engineering and Geosciences, Barcelona.

CONSIDERING ELASTIC JOINTS IN BOUNDARIES USING THE PARAMETERS OF THE BOUNDARY CONDITIONS

X. Pintado*

*Mitta Oy; Riihimiehentie 3, 01720 Vantaa, Finland
Email: xavier.pintado@mitta.fi

Key words: Joint, springs, mechanical boundary condition.

Abstract. *The consideration of boundary conditions using Winkler springs has been recently implemented in CODE_BRIGHT. Combining the parameters that define the boundary conditions, it is also possible to create a second spring orthogonal to the boundary, leaving the first spring with certain capacity of deformation or even, stiff (null displacements). The method proposed here allows to create joints in boundaries. These joints have the advantage that it is not necessary to implement new materials or elements. The main limitation is that these joints can only be elastic.*

1 INTRODUCTION

In some cases, it is necessary to consider relative displacements between two surfaces (2-D) or two volumes (3-D), or between a surface (2-D) or volume (3-D) and a boundary. These relative displacements are mainly due to the friction. CODE_BRIGHT can use elements implemented for dealing with friction, the zero-thickness elements, but only in 2-D geometries. It is also possible to create a material with continuous elements for considering the friction. Due to the 3-D zero-thickness elements are not implemented yet, this is the only option available in 3-D geometries.

Recently, it has been implemented in CODE_BRIGHT the option of fixing the mechanical boundary conditions fixing the displacements instead fixing the velocities. This option allows to use the Winkler springs as boundary conditions, where the nodal forces are now function of the nodal displacements instead function of the displacements rates.

The formulation of the mechanical boundary conditions allows to create boundaries with friction without the implementation of new elements or new materials. The main disadvantage is that the model is elastic, without any option of including plasticity unless it will be implemented by the developers of the computer code.

This implementation might be useful in spent nuclear fuel repositories' design. One of the options for storing the spent nuclear fuel is in vertical deposition holes drilled in caverns at 400-500 m deep, the KBS-3V disposal design alternative[1,2]. These deposition holes will have metal containers with the spent fuel elements surrounded by compacted bentonite. The host rock will be crystalline and it can be expected certain friction between the buffer and the rock. If the rock is not simulated and it defines just the boundary, it could be possible to implement a boundary condition which considers the possible friction rock – buffer.

2 IMPLEMENTATION OF THE FRICTION BOUNDARY CONDITION

The friction problem is presented in a KBS-3V deposition hole (Figure 1). Due to the geometry is clearly axisymmetric, only this geometry will be assessed. Considering friction might be complicated because a new material and new set of elements must be implemented. The elements might be zero-thickness elements[3] or continuous elements[4]. For practical reasons, the gap between the blocks and the rock will be filled with pellets, so in a small region, there will be four different

materials (buffer blocks, pellets, friction material and rock), two of them (pellets and friction material), in thin volumes.
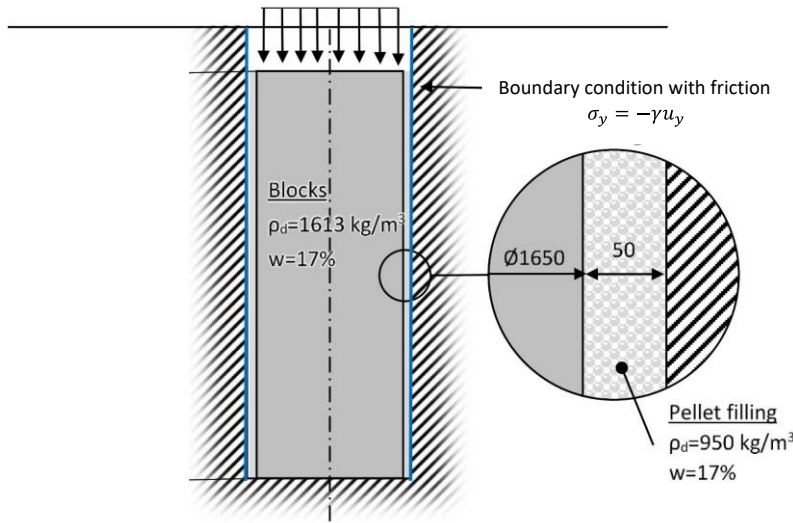
Figure 1. KBS-3V deposition hole.

If the rock is not considered and the contact buffer – rock is just a boundary, it could be possible to use the formulation of the boundary conditions in CODE_BRIGHT for the implementation of springs in order to be able to consider the friction buffer – rock.

The 2-D boundary conditions in CODE_BRIGHT can now be defined as:

$$u_1 = u_x cos(\alpha_1) + u_y cos(\beta_1) \tag{1}$$

$$u_2 = u_x cos(\alpha_2) + u_y cos(\beta_2) \tag{2}$$

$$f_y = f_y^0 + \gamma cos(\beta_1)(u_1^0 - u_1) + \gamma cos(\beta_2)(u_2^0 - u_2) \tag{3}$$

Where u_1 and u_2 are the displacements in two directions, α_1 and α_2 are the angles of the directions respect to x-axis, β_1 and β_2 are the angles of the two directions respect the y-axis, f_y is the nodal force in MN and γ (MN/m) is a parameter. The boundary condition can also be fixed considering stresses, so f_y becomes σ_y and the constant γ is defined in MN/m³. If the displacements at certain direction must be null, γ should be large. It is important to point out that CODE_BRIGHT used to fix the mechanical boundary conditions fixing the velocities $\dot{u}_1$ and $\dot{u}_2$, with γ positive[4]. If the boundary conditions are fixed as function of the boundary displacements, γ must have negative value (just as a flag).

In lateral boundary (buffer – rock contact) $cos(\alpha_2)$ and $cos(\beta_1)$ are null,

$$u_1 = u_x cos(\alpha_1) \tag{4}$$

$$u_2 = u_y cos(\beta_2) \tag{5}$$

Then, if f_y^0, u_1^0 and u_2^0 are also null,

$$f_y = -\gamma cos(\beta_2)u_y cos(\beta_2) = -\gamma\left(cos(\beta_2)\right)^2 u_y \tag{6}$$

It is possible to define a constant spring if the direction of u_2 and u_y are the same (y-axis). The constant of the spring is $\gamma\left(cos(\beta_2)\right)^2$. The value of γ is already fixed with the default value due to $u_1=u_x=0$, and $cos(\alpha_1)=1$.

It is important to point out that this boundary condition cannot consider the plasticity of the joint, so the shear stiffness increases and the plasticity depends on the material in contact with the boundary, the pellets in this case.

3   RESULTS

A friction boundary was implemented considering a K_s of 1531 MPa/m. If the rock is considered stiff in radial sense, a large value of γ should be used. The value used in this analysis was -10^{10} MPa/m. The negative sign is for considering displacements instead velocities (flag). With these values, $cos(\beta_2)$ is 3.9123×10^{-4}. It is also possible to consider springs in both senses (radial and axial), so the γ value might have the expected value in radial sense and it is necessary to choose a proper value of $cos(\beta_2)$. The geometry presented in Figure 1 was simulated considering hydration from the bottom and from the lateral boundary. The problem solved was hydro-mechanical and different options were tested. These options were plastic continuous material (Joint plastic), plastic zero-thickness material (ZT_plastic), plastic continuous material (Joint elastic), elastic zero-thickness material (ZT_elastic) and springs, the proposed method modifying the boundary conditions. The results can be seen in Figure 2.
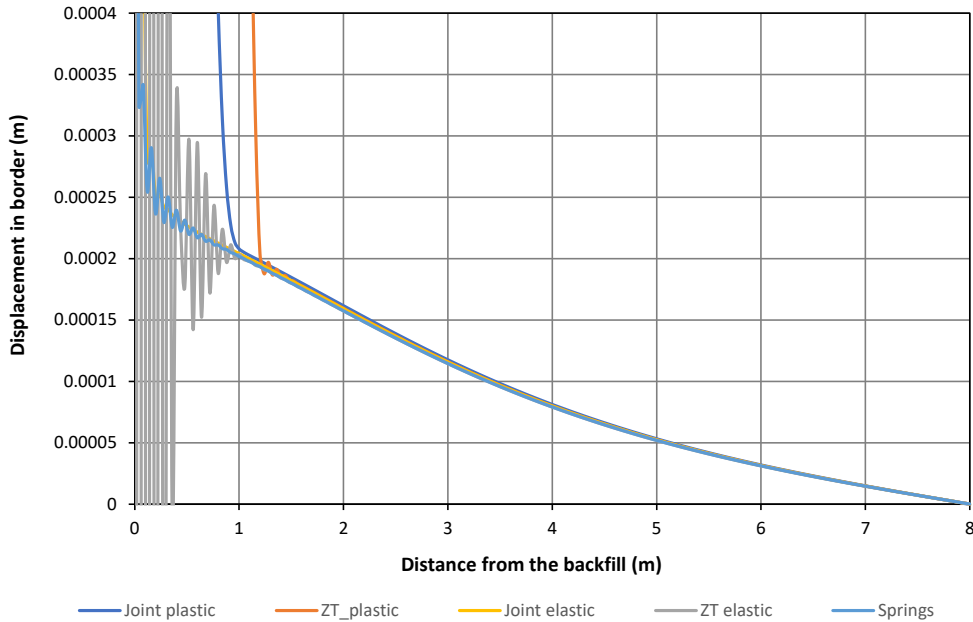
Figure 2. Displacement in the border (contact buffer – rock) as function of the distance from the backfill (on top of the deposition hole).

The plastic models worked well although displacements larger than 0.0004 m are not presented. The elastic model showed instabilities, highlighting the instability showed by the elastic zero-thickness model.

The simulations carried out with the spring boundary conditions are part of a SKB report[5], where more details about the model parametrization and results can be found.

4   CONCLUSIONS

- The comparison of the CODE_BRIGHT results with the analytical solutions obtained from the simulations of the simple shear test and triaxial test using the von Mises and the Modified Cam clay models verify the computer code for these simple geometries and load paths.
- The verification exercise should continue comparing the results obtained in CODE_BRIGHT with the results obtained in other computer codes in more complex geometries and load paths without analytical solution.
- It is not possible to implement this boundary conditions from the pre-process program (GiD). It is necessary to modify the *root_gen.dat* directly.

ACKNOWLEDGEMENTS

REFERENCES

[1] SKB, 2010. Design, production and initial state of the closure. SKB Technical report TR-10-17, Stockholm, Sweden.

[2] Posiva, 2013. Safety case for the disposal of spent nuclear fuel at Olkiluoto. Performance assessment 2012. Posiva Report 2012-04. Eurajoki, Finland.

[3] Zandarin, M.T. 2010. Thermo-hydro-mechanical analysis of joints – A theoretical and experimental study. PhD dissertation. Technical University of Catalonia. Barcelona, Spain.

[4] DECA-UPC, 2020. THM discontinuities in 2D and 3D. Centro Internacional de Métodos Numéricos en Ingeniería (CIMNE). Barcelona. Spain. Available in https://deca.upc.edu/en/projects/code_bright/downloads/documents/thm_discontinuities_3d_2d_v4.pdf/view

[5] Pintado, X. 2022. Parameter study of buffer upwards expansion into backfill. SKB report P-22-08. Solna, Sweden. *To be available in autumn 2022.*

PREDICTION OF THE BUFFER SATURATION IN THE PROTOTYPE REPOSITORY

Daniel Malmberg[*] and Mattias Åkesson[†]

[*] Clay Technology AB
IDEON Science Park, SE-223 70 Lund, Sweden
E-mail: dm@claytech.se, web page: www.claytech.se

[†] Svensk Kärnbränslehantering AB (SKB)
Box 3091, 169 03 Solna, Sweden
E-mail: mattias.akesson@skb.se - Web page: http://www.skb.se

Key words: Prototype repository, Buffer, Bentonite, Numerical modelling

Abstract. *Different pre-modelling activities are being performed as part of the planning of a retrieval operation of the inner section of the Prototype repository. This paper describes a prediction of the current saturation state of the buffer in this section.*

1 BACKGROUND

The Prototype Repository is a full-scale field experiment in crystalline rock at a depth of 450 m in the Äspö Hard Rock Laboratory (Äspö HRL). The experiment aims to simulate conditions largely relevant to the Swedish/Finnish KBS-3V disposal concept for spent nuclear fuel. The experiment consists of six deposition holes with copper canisters (with electrical heaters) and with bentonite (MX-80) buffer. The buffer was installed as compacted blocks and by filling the outer slot between the blocks and the rock wall with bentonite pellets. The test-tunnel was divided into two separate sections and backfilled and finally sealed by two reinforced concrete dome plugs. The inner section, with four deposition holes, was installed in 2001, whereas the outer section, with two deposition holes, was installed in 2003 and subsequently retrieved in 2010/2011. The inner section will be retrieved beginning in 2023, and different pre-modelling activities are currently ongoing as part of the planning of this operation. The aim of this work is to estimate the buffer saturation in the Prototype Repository.

2 EXPERIENCES FROM THE OUTER SECTION

Modelling of outer section. A TH model of the outer section of the Prototype repository was presented by Malmberg and Kristensson[i]. A three-step solution strategy was adopted in order to avoid long computation times and numerical instability: i) A large-scale hydraulic model prior to installation of the experiment, with an empty tunnel and deposition holes, to calibrate the rock material with respect to measured inflow; ii) Large-scale uncoupled thermal and hydraulic models after installation of the experiment to determine boundary conditions for the local model; and iii) a set of local-scale, coupled thermo-hydraulic models for studying the wetting process in the buffer, from installation to excavation. To represent the hydraulic transport properties of the rock without including a complex fracture network, the host rock was represented by a set of volumes equipped with different conductivities calibrated by comparing simulated and measured inflows to tunnel and deposition holes. A deposition hole

in the local models, was embedded in a 1 m thick material with low permeability, which was intersected at different positions by identified local-inflow zones. This solution strategy seemed to work satisfactory. During the work it was however found that "the uncertainties in the measured inflows to the deposition holes were too large to make a precise calibration of the rock surrounding the deposition holes" and that "the buffer wetting process was sensitive to the calibration of the rock surrounding the deposition holes" [ii]. It was therefore not possible to make predictions of any specific part of the buffer.

Dismantling data. An extensive and detailed analysis regarding the water content and the density of the buffer was performed during the course of the dismantling of the outer section of the Protype repository[iii]. These measurements showed that that the buffer had essentially reached saturated conditions in all parts except in the central parts of the cylinder below the canisters, and in the two cylinders above the canisters (Figure 1). Moreover, the distribution of the water content and the dry density in some sections in both deposition holes (Dh5 and Dh6) showed that the wetting and the swelling in one direction was much larger than in the opposite direction, and that this pattern was more pronounced in the upper part of the buffer. This may be correlated with the mapped fractures in the case of Dh5, but this does not seem to be a likely explanation for Dh6. Instead, the potential formation of conducting channels in the pellets-filled slot has been addressed in this modelling task.

Pore pressure evolution. The pore pressure in the backfill in the outer section increased fast from a low level when the drainage of the tunnel was closed in November 2004. After the drainage was opened, the pore pressure increased and a relatively constant pore pressure (of ~ 1 MPa) was measured during the second half of the operation period[iv], thereby indicating that the backfill was fully saturated at the time of dismantling. This was also confirmed from the subsequent sampling and analysis. Similar trends have been measured in backfill in the inner section, although the pore pressure has stabilized at a higher level (~ 2 MPa).
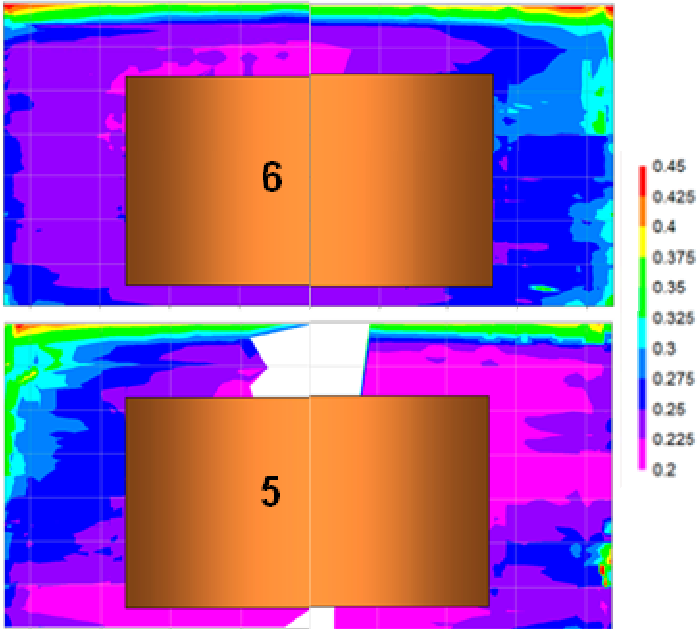
Figure 1: Contour plots of measured water content; composite plot for two opposite directions in deposition hole 6 (upper) and 5 (lower).

3 MODEL DESCRIPTION

General strategy. The water uptake of the buffer in different depositions holes of the Prototype repository has been modelled with a 3D-geometry by solving the coupled thermal and the hydraulic problems, and by using the FEM-code Code_Bright v2021[v]. The strategy for this modelling task has been: i) to simplify the geometry as far as possible by limiting the rock volume surrounding the buffer, representing it with a hollow cylinder with a thickness of 0.3 m; ii) by using measured rates of inflow for calibration of permeable fracture materials, which intersects a low permeability matrix rock; iii) by using the measured pore pressure in the backfill as an input to the hydraulic boundary condition; iv) by using an analytical solution for line sources as an input to the outer thermal boundary condition; v) by adapting a porosity distribution which corresponds to an expected level of remaining heterogeneity; iv) by considering the formation of a permeable channel in the pellets filled slot, by adapting a permeable channel material in the upper half of the buffer.

Finally, the modelling approach was first tested on deposition hole 6 (Dh6), which was dismantled in 2010/2011 and for which data on water content and density distributions are available (Figure 1), after which some calibrations were made (see below). Finally, the approach was applied, as a blind prediction, on the case of deposition hole 4 (Dh4),

Geometry. The model includes representations of the canister, the buffer (corresponding to the height of the 14 blocks) and the rock cylinder which is intersected by channels. The width of the rock cylinder is calculated as the inverse of the fracture intensity (P_{32}). A motivation for this approach was presented by Malmberg and Åkesson[vi], and a total fracture intensity value of 3.41 m^{-1} for the Prototype repository was reported by Stigsson et al. [vii].

Initial conditions. Instead of simply assigning a porosity distribution which corresponds to the installed block and pellets filling, an approach has been followed in which an expected level of remaining heterogeneity has influenced the porosity distribution. By assuming that the inner slot between the buffer rings and the canister has been filled, and that the remaining void ratio difference between the block and pellets is 0.15. This means that the dry density of the swelled blocks was set to 1620 kg/m^3, whereas the corresponding value for the compressed pellets was set to 1490 kg/m^3. The motivation for this approach was to enable the calculation of a water content that can be compared with the water content measured after dismantling.

Boundary conditions. The heat load from the canister followed the actual heat output from each canister considered in the modelling task. The temperature at the outer boundary was derived from an analytical solution for a set of line sources[viii], in which the output from all heaters were included.

The hydraulic boundary pressure for the open deposition hole, for which the fracture material was calibrated, and also for the initial phase of the operational period was set to 0.25 MPa. This was assessed to be representative for a drawdown at a distance of 0.3 m from the tunnel wall. The boundary pressure was replaced with the measured pressure evolution for the backfill in each tunnel section considered in the modelling task, once the initial level was exceeded.

Measured inflows from mapped fractures and total inflow into deposition holes were reported by Rhén and Forsmark[ix]. The total flow rates were generally much higher than the fracture flow rates, and it is not obvious how this discrepancy should be handled. In this work, the main approach has been to calibrate the fracture materials from the measured fracture flow rates. The remaining contribution to the total inflow was in the case of Dh6 allocated to the bottom of the deposition hole. The motive for this was the quite extensive water uptake

observed in the dismantling data for this part. This approach has however not been used as a general rule, since it appears to be unjustified in the case of Dh5, which display only limited water-uptake in the bottom. In such cases, the discrepancy between total and fracture inflow was simply overlooked.

Constitutive laws and parameter values. The thermo-hydraulic processes were described by the following three transport processes: i) heat transport, controlled by the temperature gradients (Fourier´s law); ii) liquid transport, controlled by the liquid pressure gradients (Darcy´s law) and; iii) vapor diffusion, controlled by vapor mass fraction gradients (Fick´s law). Parameter values for the different constitutive laws and for the different materials are compiled in Table1.
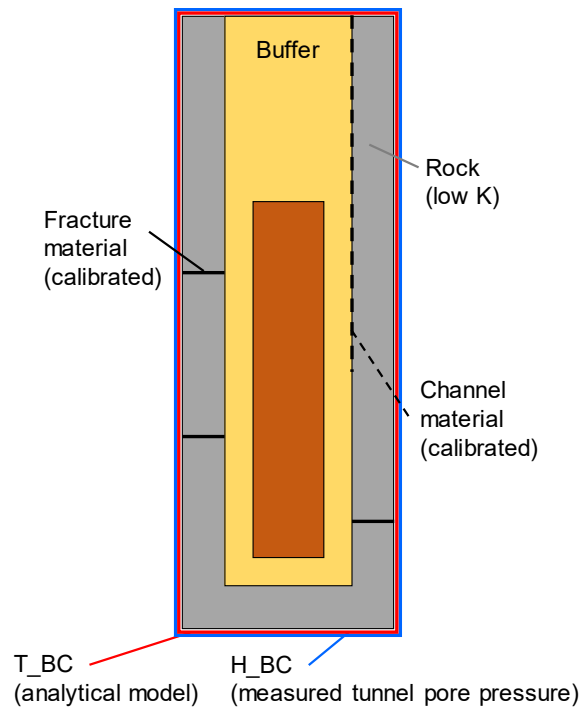
Figure 2: Simplified 3D-geometry and boundary conditions

Parameter			Buffer High density	Buffer Low density	Buffer Channel	Rock Matrix	Rock Fracture
Porosity	n (--)		0.417	0.464	0.464	0.001	0.001
Specific heat	c (J/kgK)		800	800	800	770	770
Particle density	ρ_s (kg/m^3)		2780	2780	2780	2770	2770
Thermal conductivity	λ_{dry} λ_{sat} (W/mK)		0.7 1.3	0.7 1.3	0.7 1.3	2.685 2.685	2.685 2.685
Intrinsic permeability	$k0$ (m^2)		4.13×10^{-21}	1.14×10^{-20}	10^{-16}	5×10^{-20}	[1]
Relative permeability	kr (-)		S^4	S^4	S^4	0.24 [2]	0.24 [2]
Vapor diffusion tortuosity	τ (-)		0.5	0.5	0.5	1	1
Water retention curve (van Genuchten)	$P0$ (MPa) λ (-)		7.551 0.18	3.067 0.20	3.067 0.20	0.6 0.24	0.6 0.24
All values were essentially adopted in line with the methodology outlined by Åkesson et al[x]. Minor adjustments were however made following the calibration of the model case of Dh6 (see below).							
1)The value ranges between 2×10^{-16} – 1×10^{-17} for the different fractures in the model.							
2)The van Genuchten Mualem relation was used (see CODE_BRIGHT manual[v]), the value given is that of λ							

Table 1: Parameter values for the different materials

4   RESULTS

Model results for the case with Dh6 shows that the chosen modelling strategy with a minimized 3D geometry is reasonably efficient. Comparisons with experimental data has motivated some calibrations of the model concerning: i) the thermal boundary condition in the upper part; ii) the permeability of the rock matrix material; and iii) the width of the channel in the low-density bentonite.
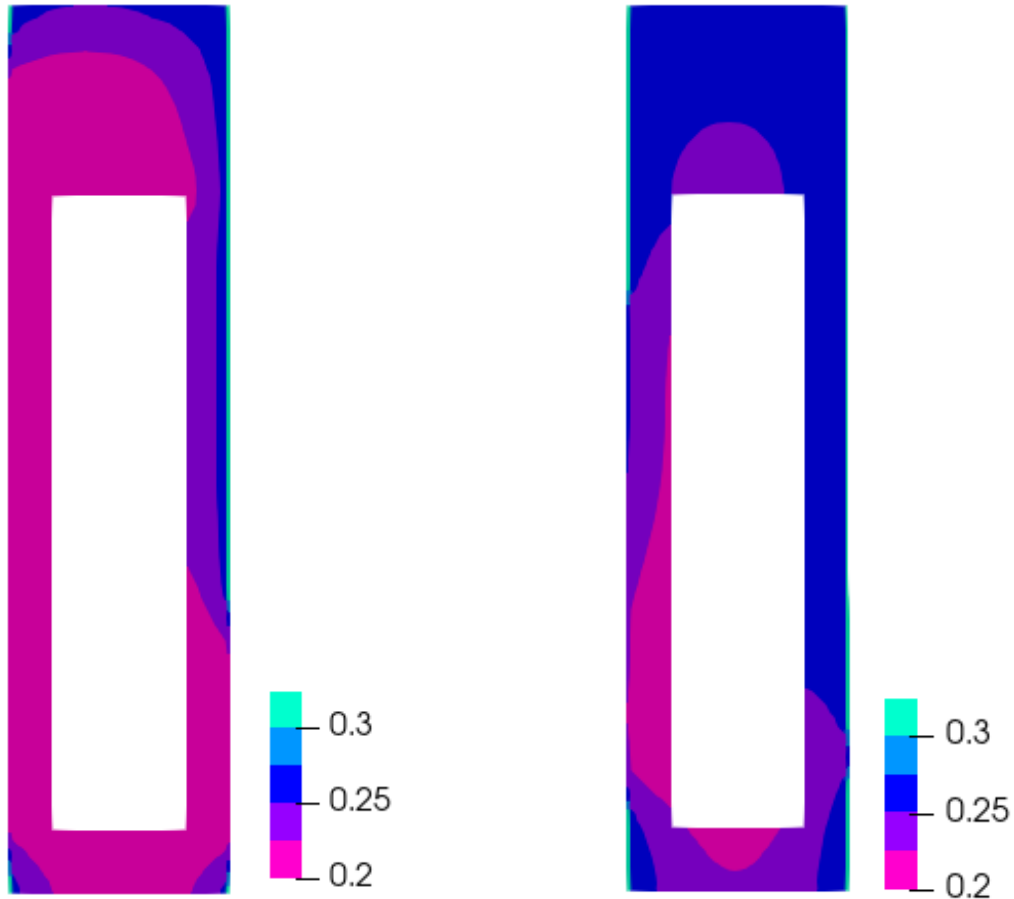
Figure 3: Final water content in the model of DH6 (left) and DH4 (right). The frame is orientated such that the right side of the plot cuts through the middle of the pellet channel.

The final water content in the model of Dh6 is shown to the left in Figure 3. The color scale was chosen to agree with the colors inFigure 1. When comparing between the model and measured results it is important to remember that the density differs significantly between the two. In the model, the high-density bentonite is fully saturated at a water content of 0.258, whereas the water content at full saturation in the experimental data varies. Nevertheless, it's clear that the model is drier than the experimentally measured values. The reason for this difference is not clear, but is, at least in part probably due to that the model was constructed by assuming that the buffer was in its final semi-homogenized state from the start, which tends to slow down the water-uptake rate. Furthermore, comparison with experimental data suggests that the channel in the low-density part of the bentonite may need to be significantly wider to reproduce the conditions in the experiment. The model of Dh4 shows that the buffer will achieve a high degree of saturation, although some parts of the buffer may not be fully saturated at the time of dismantling. In order to achieve a better agreement with the

5

dismantling data from Dh6, and thereby improve the prediction of the final state in Dh4, further models will be constructed.

REFERENCES

[i]   Malmberg D, Kristensson O, 2014. Thermo-hydraulic modelling of the bentonite buffer in deposition hole 6 of the Prototype Repository. In: Clays in Natural and Engineered Barriers for Radioactive Waste Confinement. Geological Society, London, Special Publications, 400, 251–263.

[ii] Svemar C, Johannesson L-E, Grahm P, Svensson D, Kristensson O, Lönnqvist M, Nilsson U,2016. Prototype Repository. Opening and retrieval of outer section of Prototype Repository at Äspö Hard Rock Laboratory. Summary report. SKB TR-13-22, Svensk Kärnbränslehantering AB.

[iii] Johannesson L-E, 2014. Prototype Repository. Measurements of water content and density of the excavated buffer material form deposition hole 5 and 6 and the backfill in the outer section of the Prototype Repository. SKB P-13-14, Svensk Kärnbränslehantering AB.

[iv] Goudarzi R, 2021. Prototype Repository – Sensor data report Period 2001-09-17 to 2020-01-01, Report No 31. SKB P-20-33, Svensk Kärnbränslehantering AB.

[v]   DECA-UPC, 2021. CODE_BRIGHT. A 3-D program for thermo-hydro-mechanical analysis in porous media. USER'S GUIDE. Centro Internacional de Métodos Numéricos en Ingeniería (CIMNE). Barcelona. Spain.

[vi] Malmberg D, Åkesson M, 2018. Modelling the Interactions between Engineered and Natural Barriers. Task 8 of SKB Task Forces EBS and GWFTS. SKB P-17-03, Svensk Kärnbränslehantering AB.

[vii] Stigsson M, Outters N, Hermansson J, 2001. Äspö Hard Rock Laboratory. Prototype Repository. Hydraulic DFN model no:2. SKB IPR-01-39. Svensk Kärnbränslehantering AB.

[viii] Ikonen K, 2003. Thermal analyses of spent nuclear fuel repository. Posiva report 2003-44.

[ix] Rhén I, Forsmark T, 2001. Äspö Hard Rock Laboratory, Prototype Repository, Hydrogeology. Summary report of investigations before the operation phase. SKB IPR-01-65, Svensk Kärnbränslehantering AB.

[x]   Åkesson M, Börgesson L, Kristensson O, 2010. SR-Site data report. THM modelling of buffer, backfill and other system components. SKB TR-10-44. Svensk Kärnbränslehantering AB.

COUPLED THM RESPONSES OF CALLOVO-OXFORDIAN CLAYSTONE SUBJECT TO THERMAL LOADING

Fei Song[*]**, Stefano Collico**[*] **and Antonio Gens**[*]

[*]Department of Civil and Environmental Engineering
Universitat Politècnica de Catalunya (UPC)
Campus Nord UPC, 08034 Barcelona, Spain
E-mail: fei.song@upc.edu, stefano.collico@upc.edu, antonio.gens@upc.edu

Keywords: THM coupled analysis, Geological radioactive waste disposal, Thermal loading, Strain localization, Callovo-Oxfordian claystone

Abstract. *This paper describes the numerical simulation of the gallery response to excavation and thermal loading, in the context of geological radioactive waste disposal. The coupled thermal-hydro-mechanical (THM) formulations developed by Code_Bright have been used. Furthermore, an elastoplastic constitutive model with damage and nonlocal formulation is used to characterise the mechanical behaviour of argillite rocks. Numerical results show that the obvious shear bands and preferential pathways can be developed subject to thermal loading. The numerical simulations have significantly enhanced the understanding of the THM response in the construction of geological disposal of radioactive waste.*

1 INTRODUCTION

Argillite rocks, such as Callovo-Oxfordian claystone (COx) and Opalinus clay (OPA), are considered potential host rocks for underground repositories of high-level radioactive waste disposal (Gens 2003). These materials exhibit favourable characteristics, such as low permeability, significant retardation properties for solute transport and no foreseeable economic value. Regarding their mechanical properties, they usually have strain-softening behaviour, stiffness and strength anisotropy, rate-dependency and time-dependency, which meet challenges from the modelling point of view (Mánica et al. 2021).

On the other hand, geological high-level radioactive waste is heat-emitting and therefore, the applications of argillite rocks exhibit the coupled thermal-hydro-mechanical (THM) behaviour. Furthermore, the temperature rise in argillite rocks can induce thermal pressurization, *i.e.*, overpressure response. Therefore, a comprehensive analysis of the coupled THM responses and more actual mechanical behaviours of argillite rocks is crucial to performing a proper numerical simulation.

This study focuses on analysing the coupled THM responses of the gallery subject to underground excavation and thermal loading. This work was carried out in the framework of the European Joint Programme on Radioactive Waste Management (EURAD) project. The THM formulations and constitutive models are first introduced in Section 2. Then, the numerical model and numerical results are described in Sections 3 and 4, respectively.

2 BASIC THEORY

Figure 1 shows the coupled THM phenomena for the porous medium with low permeability developed by the finite element method software Code_Bright. In this study, saturated

condition is considered, *i.e.*, the porous medium is composed of solid and liquid phases. The coupled THM problem is based on the simultaneous solution of the following balance equations: (1) the mass balance of the solid phase in the medium, (2) the total mass balance of water in the liquid, (3) the balance of internal energy for the medium, (4) the equilibrium equation. A more detailed finite element formulation utilized in Code_Bright can be found in Olivella et al. (1996, 2022).

The liquid advective flux related to phase motion is governed by the generalised Darcy's law, and the heat conduction is governed by Fourier's law. To account for the observed permeability increase due to damage evolution, the intrinsic permeability develops with the accumulated plastic deformation increases. The well-known Van Genuchten-Mualem model is adopted for the relative permeability law. Water viscosity depends on temperature.

The dependences of the liquid and solid densities on temperature, solid pressure and liquid pressure are considered (Gens et al. 2007). In the micromechanical analysis, the solid and fluid contents, and the pores can be explicitly modelled (Vu et al. 2020). The mean stress on the solid phase (p_s) can be expressed by the total mean stress (p), the porosity (ϕ) and the liquid pressure (p_l), as shown in Equation. (1) (Vu et al. 2020).

$$p_s = \frac{(p+\phi p_l)}{1-\phi} \qquad (1)$$
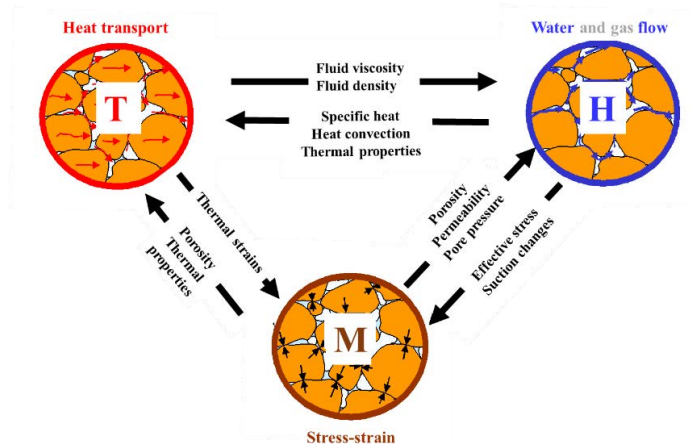
Figure 1: THM coupled phenomena in the finite element method software Code_Bright. Based on the work of Olivella et al. (2022), Tourchi (2020) and Alonso et al. (2021).

An elastoplastic model with damage and nonlocal formulation is used in this study. This constitutive model has been developed for hard soils-soft rocks, as described in Manica et al. (2021). The following features are considered: (1) hyperbolic approximation to the Mohr-Coulomb model, (2) anisotropy of stiffness and strength, (3) strain-softening behaviour of geomaterials, and (4) non-local integral type approach for the plasticity model, to simulate the localised plastic deformations. Details of the constitutive model can be found in the references (Mánica 2018; Mánica et al. 2021).

3 NUMERICAL MODEL

3.1 Geometry and mesh

The model consists of a cross-section of a gallery and the host rock perpendicular to the gallery axis. The numerical model developed using Code_Bright is calculated under plane-strain conditions. Only a quarter of the gallery cross-section is modelled in the numerical model,

2

because of the double symmetry of the geometry and the boundary conditions at both x- and y-axes. The simulated region measures 100 m in both x- and y- directions. In addition, the normal displacements along the bottom (y = 0) and the left (x = 0) boundaries are restrained.

A representation of the domain is shown in Figure 2(a) together with the specified study points. Table 1 lists the locations of these study points. Figure 2(b) shows the mesh of the numerical model. A mesh of 47933 quadrilateral elements is adopted, with smaller elements near the excavation. The generalised selective integration procedure implemented in Code_Bright can eliminate locking mesh and hour glassing issues of linear quadrilateral elements (Olivella et al., 1996).

Figure 2: (a) Basic features of the two-dimensional plain-strain numerical model and study points (conceptual model). (b) finite element mesh (47933 quadrilateral elements).

P_1	(1.25, 0)	P_2	(1.875, 0)	P_3	(2.5, 0)	P_4	(6.25, 0)
P_5	(50, 0)	P_6	(100, 0)	P_7	(0, 1.25)	P_8	(0, 1.875)
P_9	(0, 2.5)	P_{10}	(0, 6.25)	P_{11}	(0, 50)	P_{12}	(0, 100)
P_{13}	(0.884, 0.884)	P_{14}	(1.326, 1.326)	P_{15}	(1.768, 1.768)		

Table 1: Locations of the study points. Units: meters.

3.2 Initial and boundary conditions, modelling stages

Initial total stress (σ_{xx} = 12.4 MPa, σ_{yy} = 12.7 MPa, σ_{zz} = 16.4 MPa), pore pressure (p_0 = 4.7 MPa) and temperature (T = 22°C) are considered within the whole domain of the numerical model. The modelling stages are reproduced in three main steps:

Excavation stage: which extends from T_0 to T_0+24 hours, with T_0 = 0 in this study. As shown in Figure 3, the pore pressure at the gallery wall is linearly reduced in 24 hours from its initial value to 0.1 MPa, while on boundaries BC and CD a constant pore pressure is prescribed. Impervious boundaries are assigned on AB and DE. No thermal flux is applied at this stage.

Waiting stage: which extends from T_0+24 hours to T_0+6 months. The total stress is maintained at 5% of the initial in-situ stress, and constant stress is applied to BC and CD. The pore pressure is fixed and equal to the atmospheric one (0.1 MPa), allowing water to drain towards the tunnel while a constant pore pressure is applied on BC and CD. No thermal flux is applied at this stage.

Heating stage: which extends from T_0+6 months to T_0+10 years. Constant stress is applied to BC and CD. Impervious hydraulic boundaries are assigned to the borehole wall, while a constant pore pressure is applied on BC and CD. A heat flux of 200 W/m is applied to the gallery wall over ten years.

Figure 3: Boundary conditions in different modelling stages: (a) excavation stage, (b) waiting stage, and (c) heating stage.

3.1 Main physical, thermal-hydro-mechanical properties

The elastoplastic model with damage and nonlocal formulation is used in the numerical simulation and the input parameters are shown in Table 2. Table 3 lists input parameters of the main physical properties for Callovo-Oxfordian claystone and the liquid properties.

Elastic	Young's modulus	$E_{//}$ = 8000 MPa, $E_\perp$ = 4000 MPa
	Poisson's ratio	$\nu_{// //}$ = 0.25, $\nu_{// \perp}$ = 0.3
	Shear modulus	$G_\perp$ =2010 MPa
Plastic	Peak strength	φ_{peak} = 20°, c_0 = 4 MPa, p_{t0} = 1.5 MPa
	Residual strength	r_{post} = 0.3, φ_{res} = 16°
	Post-rupture	b_{post} = 160, b_{res} = 2
	Associativity	ω = 0.2
Viscoplastic	Viscosity	η_{vp} =1.3×10^7 MPa.s
	Stress power	m = 1
Strength anisotropy	Ω_{90} = 1.3, Ω_m =0.819, δ_m = 49.7°, n = 0.1	
Hydraulic	β^k = 4×10^7, λ^r = 0.32, P = 17.6 MPa	

Table 2: Input parameters of the Callovo-Oxfordian claystone. Based on the work of Mánica (2018).

Intrinsic permeability	$K_{//}$ = 3.9×10^{-20} m^2, $K_\perp$ = 1.3×10^{-20} m^2	
Thermal conductivity	$\lambda_{//}$ =1.88 W/m/K, $\lambda_\perp$ = 1.25 W/m/K	
Solid phase density	ρ_s [kg/m^3]	2690
Bulk density	ρ [kg/m^3]	2386
Porosity	ϕ [-]	0.18
Biot coefficient	B [-]	0.8
Thermal expansion coefficient	α_s [K^{-1}]	1.25×10^{-5}
Solid phase specific heat	c_p [J/Kg/K]	790
The inverse of solid compressibility	$1/\beta_s$ [1/MPa]	2.3×10^{-5}
Water density	ρ_l [kg/m^3]	1000
Specific heat of water	c_s [J/Kg/K]	4180
Compressibility of water [40°C]	β_w [MPa^{-1}]	4.5×10^{-4}

Table 3: Input parameters of the main physical properties for Callovo-Oxfordian claystone and liquid properties.

4 NUMERICAL RESULTS

The evolution of temperature and pore pressure are presented in Figure 4. Numerical results are plotted in the semi-logarithmic scale to better highlight their variation with time. As observed in Figure 4(a), a maximum temperature of around 80°C has been obtained on the

4

gallery wall, while the temperature decreases as the distance from the gallery increases. As shown in Figure 4(b), during the excavation stage, overpressure is generated along the x-direction. Meanwhile, the pore pressure linearly decreases at the gallery wall during the waiting stage, because of the applied drained boundary condition. Note that, relative low pore pressure is observed in the heating stage since big plastic deformations and big volumetric strains occur.
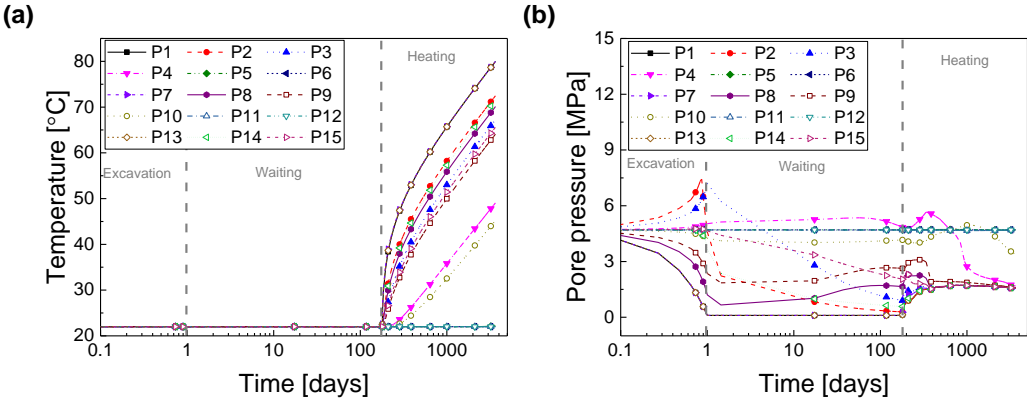
Figure 4: Evolution of (a) temperature, and (b) pore pressure.

Contours of plastic shear strains can be employed to observe the configuration of localised plastic deformations and to assess the extension of the fracture zone. Figure 5 presents the evolution of the plastic shear strain contours. It can be observed that no obvious shear bands develop in the excavation stage, and the shear bands just start to be developed during the waiting stage. In the heating stage (from 180 to 3650 days), more obvious shear bands can be identified. Shear bands extend from the gallery wall (r = 1.25 m) in the horizontal direction up to around 5.8 m into the host rock.

The evolution of permeability with damage would be essential to properly capture the pore water pressure response (Mánica 2018). Therefore, the preferential pathways for the water flux occur due to the increase in permeability. The increase of permeability concentrates within the shear bands where close to the gallery wall, because the plastic deformations concentrate there. Figure 6 shows the groundwater flux at time t = 3650 days, where the preferential pathways and the localized can be observed.
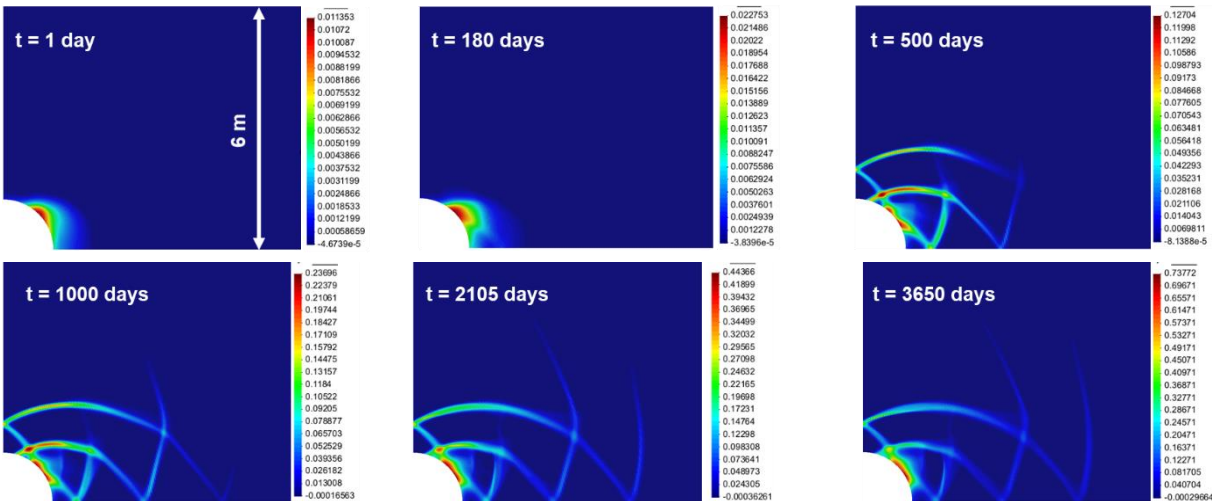
Figure 5: Evolution of the plastic shear strains.
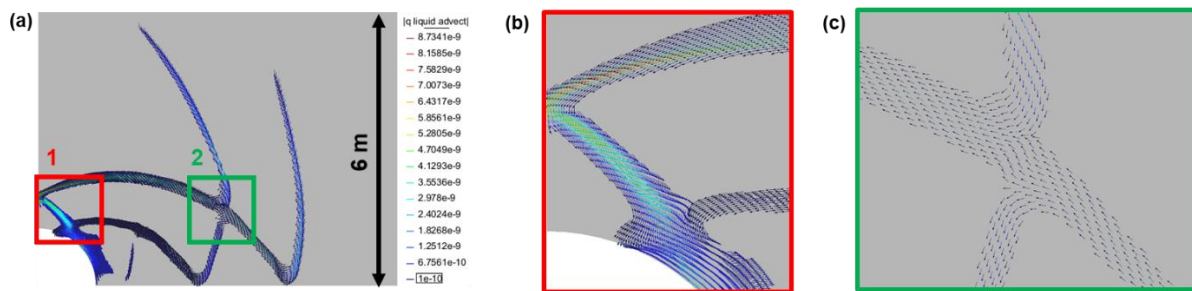
Figure 6: (a) Groundwater flux at time *t* = 3650 days. (b) and (c) show the zoom-in results of zone 1 and zone 2.

5 CONCLUSIONS

Numerical simulations have been performed to analyse the coupled THM responses of the gallery subject to underground excavation and thermal loading. Fully coupled THM formulations developed by Code_Bright have been considered in this study. An elastoplastic constitutive model with damage and nonlocal formulation is used to represent the mechanical behaviour of the host rock. Overpressure has been observed in excavation and heating stages. The obvious shear bands can be identified in the heating stage, but not in the excavation stage. The preferential pathways for the water flux occur where close to the gallery wall, because the increase of permeability induced by plastic deformations concentrates there.

ACKNOWLEDGEMENTS

REFERENCES

[i]   Alonso M, Vu MN, Vaunat J, et al (2021) Effect of thermo-hydro-mechanical coupling on the evolution of stress in the concrete liner of an underground drift in the Cigéo project. In: IOP Conference Series: Earth and Environmental Science, 833, 012200.

[ii]   Gens A (2003) The role of geotechnical engineering for nuclear energy utilisation (Special Lecture). Proc. 13th Eur. Conf. Soil Mech. Geotech. Engng, Prague 3, 25-67.

[iii] Gens A, Vaunat J, Garitte B, Wileveau Y (2007) In situ behaviour of a stiff layered clay subject to thermal loading: Observations and interpretation. Géotechnique 57:207–228.

[iv]   Mánica M (2018) Analysis of underground excavations in argillaceous hard soils - weak rocks. PhD thesis, Universitat Politècnica de Catalunya (UPC).

[v]   Mánica M, Gens A, Vaunat J, et al (2021) Numerical simulation of underground excavations in an indurated clay using non-local regularisation. Part 1: Formulation and base case. Géotechnique 1–21.

[vi]   Olivella S, Gens A, Carrera J, Alonso EE (1996) Numerical formulation for a simulator (CODE_BRIGHT) for the coupled analysis of saline media. Eng Comput (Swansea, Wales) 13:87–112.

[vii] Olivella S, Vaunat J, Rodriguez-Dono A (2022) CODE_BRIGHT USER'S GUIDE. https://deca.upc.edu/en/projects/code_bright

[viii] Tourchi S (2020) THM analysis of argillaceous rocks with application to nuclear waste underground storage. PhD thesis, Universitat Politècnica de Catalunya (UPC).

[ix]   Vu MN, Armand G, Plua C (2020) Thermal Pressurization Coefficient of Anisotropic Elastic Porous Media. Rock Mech Rock Eng 53:2027–2031.

6

COUPLED THM BEHAVIOUR OF CALLOVO-OXFORDIAN CLAYSTONE UNDER THERMAL LOADING

Stefano Collico[*], Fei Song[*] and Antonio Gens[*]

[*]Department of Civil and Environmental Engineering
Universitat Politècnica de Catalunya (UPC)
Campus Nord UPC, 08034 Barcelona, Spain
E-mail: stefano.collico@upc.edu, fei.song@upc.edu, antonio.gens@upc.edu

Abstract. *This work reports numerical results of the CRQ in-situ heating experiment in the context of geological radioactive waste disposal. A coupled thermal-hydro-mechanical (THM) formulation within by Code_Bright software is employed. An anisotropic elastic constitutive model is considered to assess and localize potential failure during heating phases due to thermal pressurization. Numerical results, validated against in-situ observations, highlight a good prediction of pore pressure trend at observational study points. The numerical simulations aim to enhance the understanding of the THM response in the construction of geological nuclear waste disposal.*

1 INTRODUCTION

Stiff clayey materials such as Callovo-Oxfordian claystone (COx) are considered potential host rocks for underground repositories of high-level radioactive waste disposal mainly due to their low permeability and degree of self-healing capacity (Gens, 2003; Gens et al., 2007).

Geological high-level radioactive waste is heat-emitting, requiring the understanding of heat effect on hydro-mechanical behaviour leading to a fully coupled Thermal-Hydraulic-Mechanical (THM) analysis of the host rock. Of particular interest is the understanding of pore pressure development during heating which might result in COx fracturing.

This study focuses on THM responses of the in-situ experiment CRQ conducted at the MHM URL. The numerical simulation consists of reproducing main drift excavations, heater boreholes' excavation, first and second heating-cooling phases. The second heating phase is of a particular interest since COx fracturing was experimentally observed.

2 THM FORMULATION

This work considers a saturated condition such that the medium is composed by two phases: solid (s) and liquid (l). The coupled THM problem is computed by simultaneously solving the mass balance of the solid phase in the medium, the total mass balance of water in the liquid, the balance of internal energy for the medium and the equilibrium equation (see Olivella et al., 1996). A generalised Darcy's law and Fourier's law to account for liquid advection flux and heat conduction are considered. Due to the simple elastic model here employed, no damage evolution is applied. Concerning water properties, an exponential water viscosity dependence on temperature (Figure 1-A) and non-linear evolution of thermal expansion coefficient of liquid

phase with temperature (Figure 1-B) are considered. Liquid and solid densities that depend on temperature are also accounted for.

A Biot's isotropic tensile strength p_t a value of 0.5 MPa (Figure 2-A) and a Terzaghi strength cut-off of 2.8 MPa (Figure 2-B) are employed as a reference strength cut-off. However, such values are characterized by a great uncertainty due to the limited amount of available data.
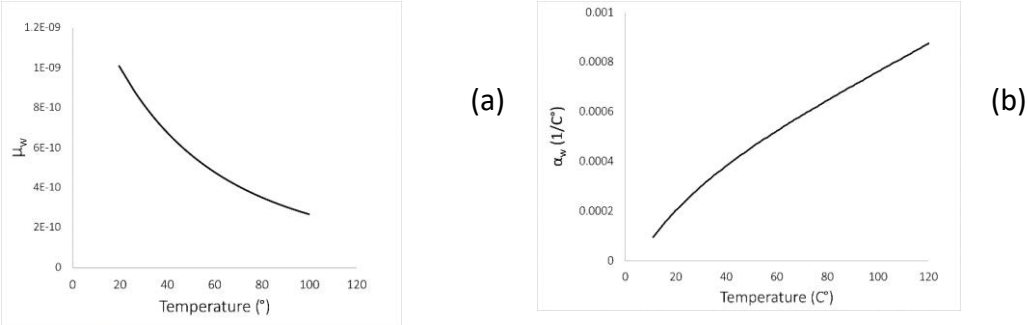
Figure 1. Variation of water viscosity with temperature (A), Variation of volumetric thermal expansion coefficient of water with temperature (B).
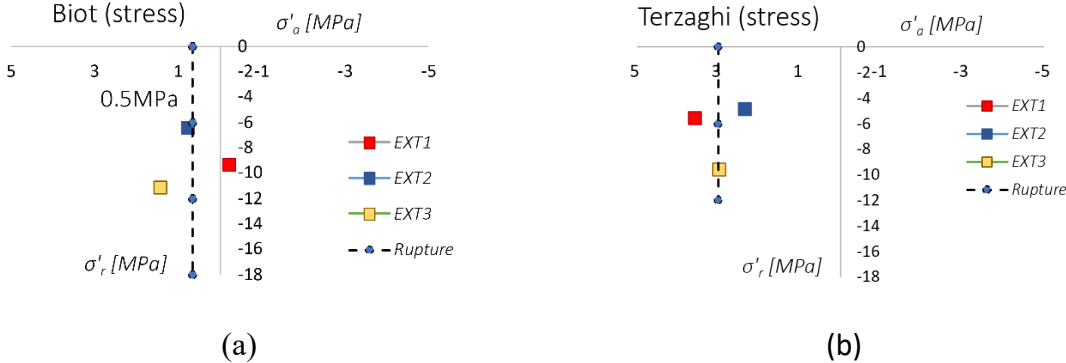
Figure 2. Biot strength cut-off established from extension tests (A), Terzaghi strength cut-off established from extension tests (B).

3 NUMERICAL MODEL

3.1 Geometry and mesh

The domain consists of a 3D cube with a side length of 50 m (Figure 3-A). The geometry includes the main GCs drift with 5.2 m of diameter, the heater boreholes (CRQ1701-CRQ1710) with 0.172 m of diameter. The temperature /pore pressure boreholes and the acoustic boreholes were not represented. Concerning the geometry, in order to reproduce the Excavation Damaged Zone (EDZ) around GCS drift and heater boreholes and to account for the potential longitudinal flow toward the GCS drift during heating phases, a material that surrounds the main gallery and heater boreholes is introduced as reported in Figure 3-B and Figure 3-C. The dimension of EDZ around the GCS drift is 4.7 m, while for EDZ around heater boreholes a d=0.3 m is considered according to values reported by Armand et al., (2014). Concerning the mesh, linear tetrahedral elements are considered. For refined mesh here reported a maximum element size of 0.05 m is applied to heater's boreholes surface, while a maximum value of 0.07 is applied to surface of EDZ heater boreholes. In such a case, the mesh consists of a total of about 169.000 nodes

(Figure 3-D). In section 4 numerical simulation by considering EDZ material with same characteristics of COx is reported.
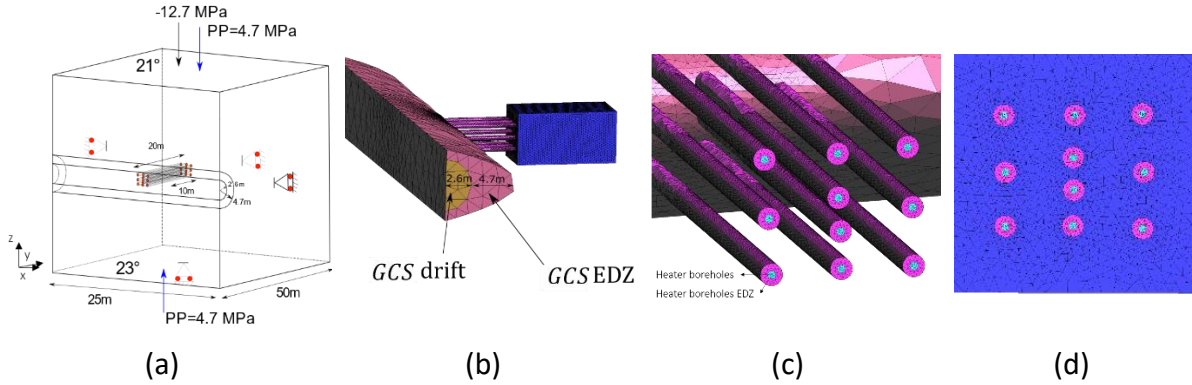
Figure 3. Qualitative 3D representation of the geometry (A), Geometry around GCS drift (B), Geometry around heater boreholes (C), Refined mesh section (D)

3.2 Initial and boundary conditions, modelling stages

Initial conditions in terms of stresses, pore pressure and temperature are assigned according to specifications and reported in Table 1. Negative values refer to compressive stress states. According to specifications, the minor principal total stress is parallel to x-axis, the intermediate parallel to z-axis and the major principal total stress parallel to y-axis. Specified boundary conditions are initially applied as reported in Table 2 and Figure 3-A.

Table 1. Initial stress, pore pressure and temperature for the three specimens according to specifications.

σ_x	σ_y	σ_z	p_w	T_0
MPa	MPa	MPa	MPa	C°
-12.4	-16.1	-12.7	4.7	22

Table 2. Initial boundary conditions according to specification.

Boundary condition	Thermal	Hydraulic	Mechanical
Lateral faces	No heat flux	No fluid flux	zero normal displacements
Top Faces	21 °C	4.7 MPa	σ_v=12.7 MPa
Bottom Faces	23 °C	4.7 MPa	zero normal displacements
CGS drift before excavation	No heat flux	No fluid flux	zero normal displacement

For each stage the following boundary conditions are applied:

- GCS drift excavation: a linear decrease of pore pressure from 4.7 MPa to 0.1 MPa is applied to main gallery surfaces and a linear stress decrease up to 0% of initial stress state is considered;
- Waiting time after GCS drift excavation: 0.1 MPa pore pressure is applied on GCS drift surfaces;
- Drilling stage: boreholes excavation is sequentially simulated according specified dates. During the excavation of each borehole, a pore pressure of 0.1 MPa is applied on boreholes surfaces and linear stress decrease up to 0% of in-situ stress state is applied;
- Waiting phase after boreholes excavation: a 0.1 MPa pore pressure is applied on boreholes surfaces until the first heating phase start;
- 1st and 2nd Heating and cooling stage: impervious boundary conditions are applied on boreholes surfaces and heat flux is applied according to specifications (Figure 4).

3
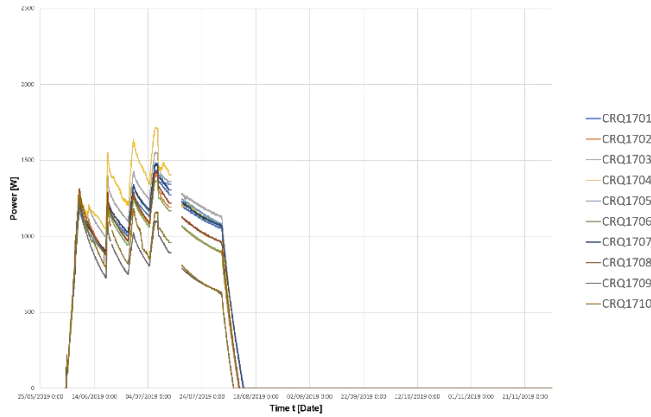
Figure 4. Heat Power applied on heater boreholes surfaces.

3.1 COx THM properties

THM properties of COX employed are reported in Table 3.

Table 3: Input parameters of the Callovo-Oxfordian claystone according to specifications.

Young's modulus	$E_{//}$ = 6 GPa, $E_{\perp}$ = 4 GPa	
Poisson ratio	$\nu_{//}$ = 0.3, $\nu_{\perp}$ = 0.3	
Cross shear modulus	G_{vh}=1.7 GPa	
Intrinsic permeability	$K_{//}$ = 4×10^{-20} m^2, $K_{\perp}$ = 1.33×10^{-20} m^2	
Thermal conductivity	$\lambda_{//}$ =1.95 W/m/K, $\lambda_{\perp}$ = 1.28 W/m/K	
Solid phase density	ρ_s [kg/m^3]	2690
Bulk density	ρ [kg/m^3]	2386
Porosity	ϕ [-]	0.18
Biot's coefficient	B [-]	0.8
Thermal expansion coefficient of solid	α_s [K^{-1}]	1.5×10^{-5}
Solid phase specific heat	c_p [J/Kg/K]	800
Water density	ρ_l [kg/m^3]	1000
Specific heat of water	c_s [J/Kg/K]	4180
Compressibility of water [40°C]	β_w [MPa^{-1}]	4.5×10^{-4}

4 NUMERICAL RESULTS

Results of the entire process in terms of pore pressure and temperature evolution for the most solicited section (i.e., located at 15m distance from the GCS gallery) are reported in Figure 5 for the elastic anisotropic case. It can be observed that temperature evolutions due to applied heat flux well match in-situ observations at each study point. The pore pressure evolution due to heating is reported in Figure 6. By applying specified COx parameter and no EDZ around heater boreholes it can be observed that the trend of pore pressure is well reproduced by numerical simulation. However, an overestimation of pore pressure can be observed at study points 1720_03, 1721_03 where higher temperature is expected. By analysing the minor Terzaghi effective stress σ'_{III} it can be observed that during the first heating phase a tensile state of stress is obtained, however, it is such that it does not meet the strength cut-off of 2.8MPa considered (as also observed experimentally). During the second heating, the state of stress is such that strength cut-off is met at the two study points 1720_03 and 1721_03 (Figure 7).

4
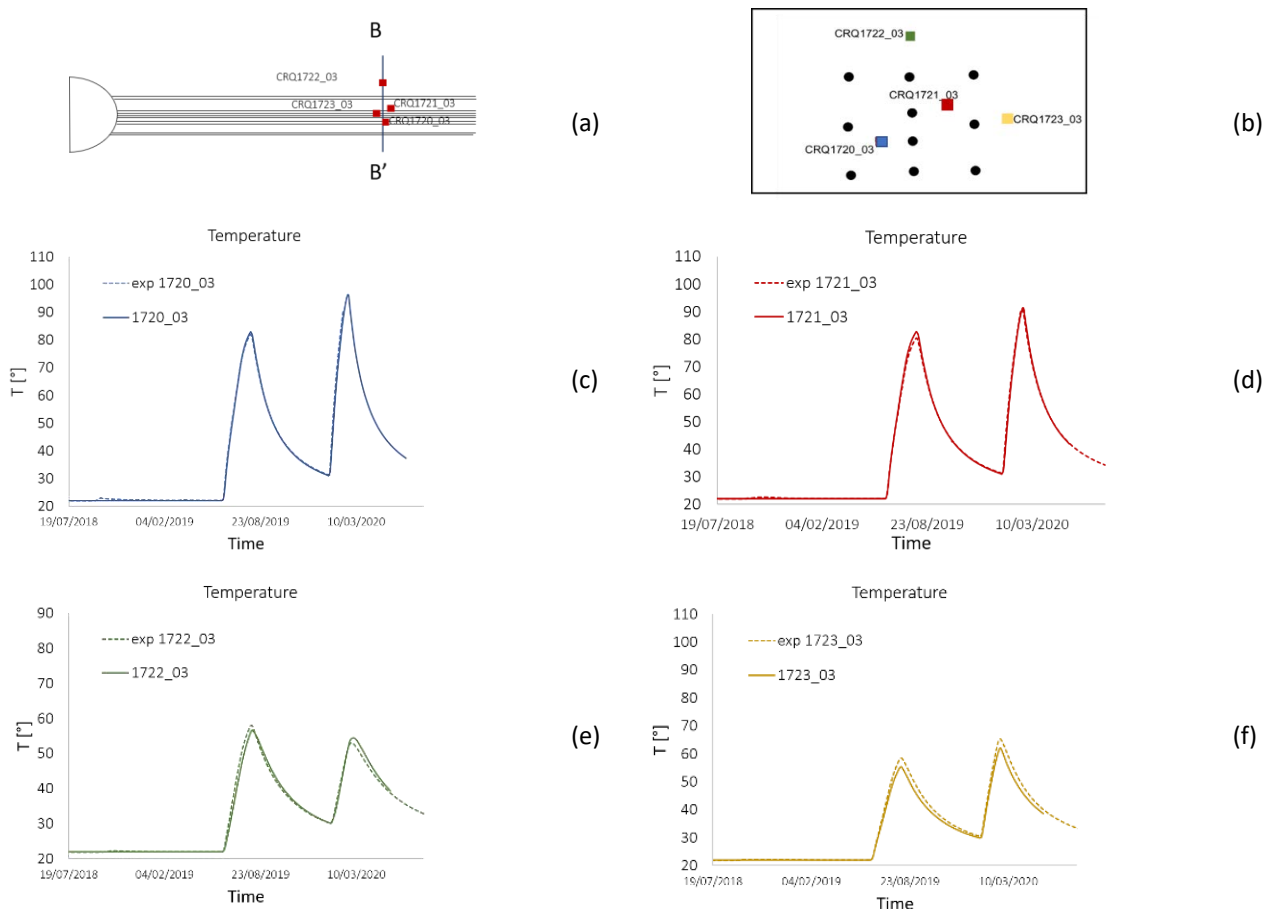
Figure 5. Qualitative representation of section BB' (A), location of study points for section BB'(B), temperature evolution at study point CRQ1720_03 (C), temperature evolution at study point CRQ1721_03 (D), temperature evolution at study point CRQ1722_03 (E), temperature evolution at study point CRQ1723_03 (F).
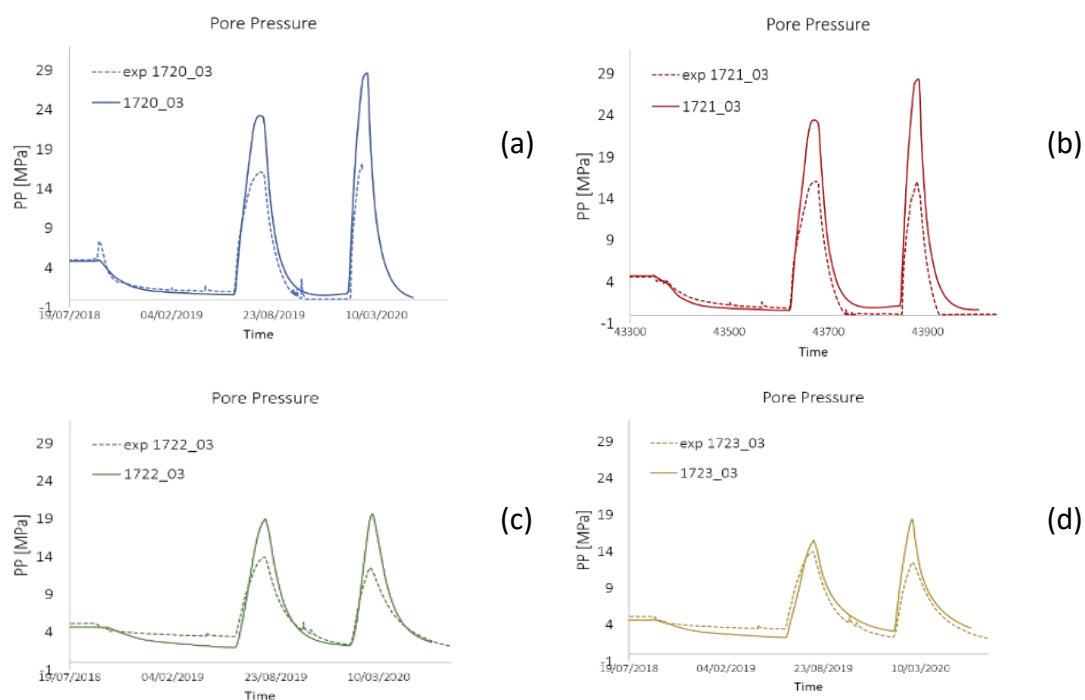
Figure 6. Pore pressure evolution at study point CRQ1720_03 (A), pore pressure evolution at study point CRQ1721_03 (B), pore pressure evolution at study point CRQ1722_03 (C), pore pressure evolution at study point CRQ1723_03 (D).
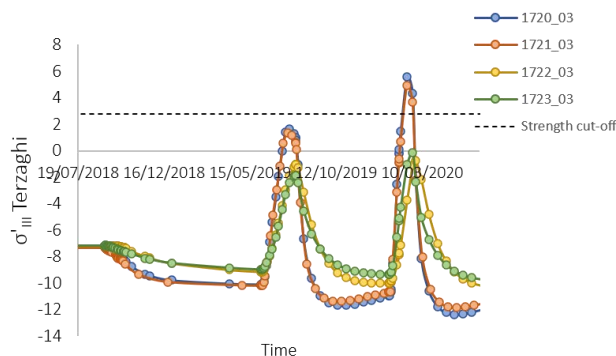
Figure 7. Terzaghi σ'_{III} evolution at different study points.

To improve pore pressure prediction the more permeable material around heater boreholes can be activated by increasing the intrinsic permeability up 1e-17 m^2. For such analyses a better prediction of pore pressure is obtained, however it results in slightly tensile state of stress during the second heating phase, which does not meet the established strength cut-off. This would suggest the application of a more complex constitutive model such as perfect elastoplastic or elastoplastic with hardening.

5 CONCLUSIONS

An anisotropic elastic constitutive model is applied to model THM responses of CRQ in-situ experiments. A coupled THM formulation developed by Code_Bright is employed in this study. Results highlight a good prediction of pore pressure trend with respect in-situ observation. However, overestimation of liquid pressure is obtained at both heating phases requiring the introduction of a more permeable material around hater boreholes, or more complex constitutive modelling.

ACKNOWLEDGEMENTS

REFERENCES
[i]   Gens A (2003) The role of geotechnical engineering for nuclear energy utilisation (Special Lecture). Proc. 13th Eur. Conf. Soil Mech. Geotech. Engng, Prague 3, 25-67.
[ii]   Gens A, Vaunat J, Garitte B, Wileveau Y (2007) In situ behaviour of a stiff layered clay subject to thermal loading: Observations and interpretation. Géotechnique 57:207–228.
[iii]   Olivella S, Gens A, Carrera J, Alonso EE (1996) Numerical formulation for a simulator (CODE_BRIGHT) for the coupled analysis of saline media. Eng Comput (Swansea, Wales) 13:87–112.
[iv]   Armand, G., Leveau, F., Nussbaum, C., De La Vaissiere, R., Noiret, A., Jaeggi, D., Landrein, P., & Righini, C. (2014). Geometry and properties of the excavation-induced fractures at the meuse/haute-marne URL drifts. Rock Mechanics and Rock Engineering, 47(1), 21–41. https://doi.org/10.1007/s00603-012-0339-6

PERFORMANCE OF 3D LARGE DIAMETER SEALING STRUCTURES IN DEEP NUCLEAR WASTE REPOSITORY

Matias Alonso[*], Jean Vaunat[*], Minh-Ngoc VU[†] and Jean TALANDIER[†]

[*] Department of Civil and Environmental Engineering
Technical University of Catalonia (UPC)
Campus Nord UPC, 08034 Barcelona, Spain
E-mail: matias.alonso@upc.edu

[†] French National Radioactive Waste Management Agency (Andra),
1 rue Jean Monnet, 92290 Châtenay-Malabry, France

Abstract. *Modelling work have been carried out to simulate numerically the phenomenology behind the response of large diameter sealing structures in the context of nuclear waste disposal. 3D and axisymmetric large scale models were created for this purpose, using advanced constitutive models, accounting for complex coupled phenomena, and representing geometric details at decimetre scale. These challenging simulations provided qualitative and quantitative results on key questions related to the design of this kind of structures, such as the extension of the damaged zone around the gallery, the duration of the natural hydration phase, the swelling pressure development of the sealing core, and the seals system global stability.*

1 INTRODUCTION

Deep geological disposal appears to be one of the most appropriated solution to store radioactive nuclear waste. Argillaceous rocks and stiff clay formations have great potential as possible geological host medium[i]. These geomaterials have very low permeability, significant retention capacity for radionuclide, a significant capacity of hydraulic self-sealing of fractures, and no economic value in most cases.

The French National Radioactive Waste Management Agency (Andra) is leading the design of The Industrial Centre for Geological Disposal (Cigéo), a deep geological disposal facility for radioactive waste to be built in eastern France. The disposal life is split into three phases: construction, operational and post-closure. After 100-150 years of operational phase, the disposal will be closed by sealing systems at some positions.

The present work is developed in the context of a sealing system at the main level of the disposal, where the tunnel is excavated (~10 m of diameter) and lined by a double layer 50 cm concrete covered by 20 cm of compressible material. In situ observations showed the creation of an excavation-induced damaged zone around the galleries (EDZ), where the properties of the host rock such as permeability and strength are altered[ii]. The sealing structures are intended to recompress the EDZ and limit the flow of water during the entire storage life (thousands of years).

This work aims to assess numerically the performance of these large diameter sealing structures under real disposal conditions. In general, the sealing systems consist of an expansive core made by a bentonite-based material, concrete and/or backfill plugs, and different backfill materials (see current French concept of sealing structure in Figure 1).

An appropriated simulation of these facilities implies accounting for several complex phenomena involved (denoted in Fig. 1). In general terms, after the construction of the sealing,

water slowly flows from the host rock to the sealing materials (process named natural hydration). The core hydration process and its duration are mainly controlled by the permeability of the host rock, and more incidentally by the hydraulic state of the damage zone around the excavation. As the saturation degree of the core increases, it swells. The final value of swelling pressure that can be reached depends basically on the material initial dry density and the volume restriction during hydration.

As the core swells, it exerts a pressure on the host rock (which is the desired effect to effectively compress the EDZ and to promote the self-sealing of existing fractures within EDZ reducing its permeability) and on the concrete plugs. As a result, the concrete plugs will move and compress the backfill. In turn, the displacement of the concretes plug will release the swelling capacity of the core. Global stability will be reached when the pressure exerted by the swelling core in the longitudinal direction (direction parallel to the gallery) is equilibrated by the sum of the backfill reaction and the friction with the lining (stabilizing forces).

The swelling potential of the core is thus strongly related to the global stability of the entire structure. If the stability is poor, the structure will suffer large longitudinal displacements, a significant loss of swelling potential, and a significant loss of core homogenization. The stability depends mainly on the quality and strength of the interface between the different materials of the sealing structure and the lining, and also on the stiffness and strength of the backfill material reacting to the compression.
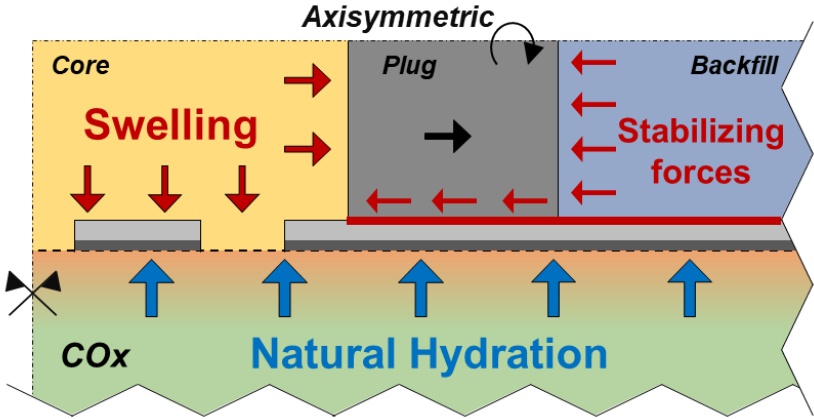
Figure 1: Current French concept of sealing structure and phenomena involved

2 MODEL DESCRIPTION

As described, the response of the sealing structures is affected by several coupled processes and different materials response. The industry is encouraging the development of increasingly sophisticated simulations, including strong coupling effects, advanced constitutive models, and large geometries including low-scale details. Advanced large scale pseudo-3D axisymmetric and fully 3D models were created (see Figure 2).

For the host rock, an elasto-visco-plastic model provided with creep was considered. It includes important aspects that allow to simulate the argillite behavior[iii, iv]. An hyperbolic approximation of the Mohr-Coulomb criterion was used for both yield and failure limits. Strength anisotropy is included by assuming that strength parameters depend on the relative orientation between bedding plane and the principal effective stress. After reaching the failure surface, non-linear hardening-softening behaviour is considered, driven by the evolution of the strength parameters controlled by a state variable.
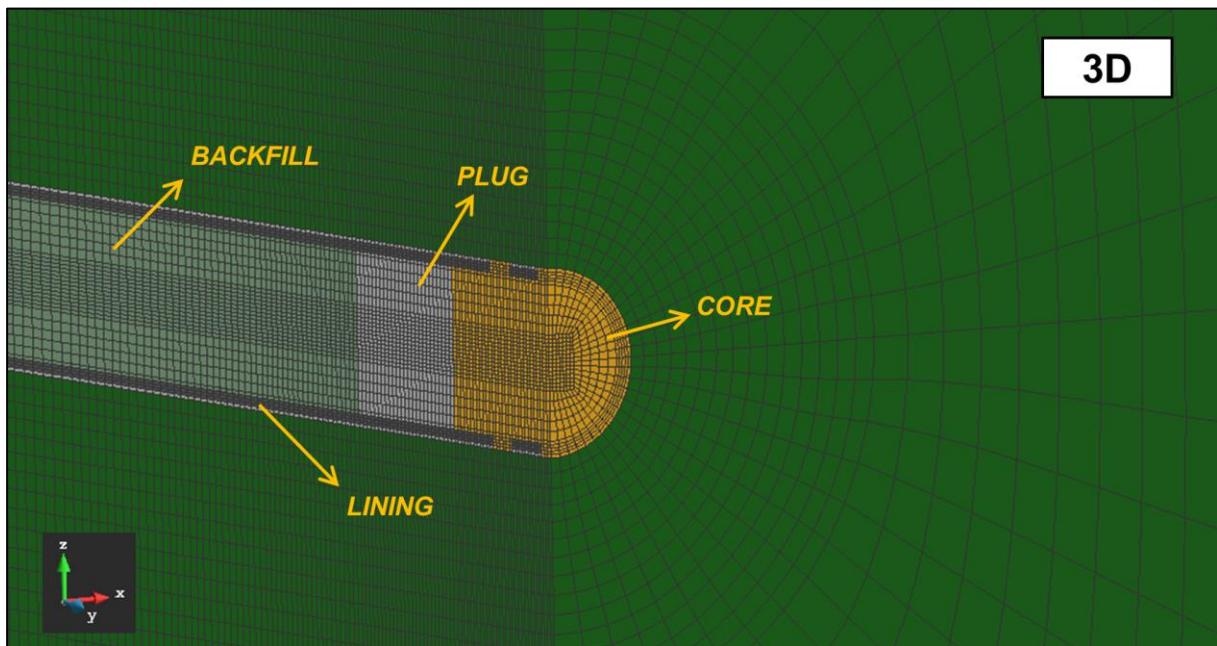
Figure 2: Partial view of the 3D model created

The behaviour of the expansive core material is simulated through the Barcelona Expansive Model [v]. Two structure levels are distinguished in this model: the microstructural level at which swelling of active minerals takes place and the macrostructural level responsible for major structural rearrangement. Microstructural swelling affect the structural arrangement of the macrostructure, inducing an irreversible increase or decrease of the void ratio. In general, the final value of swelling pressure that can be reached in a constant volume swelling pressure test (around 4 MPa in this case) depends basically on the expansive material initial dry density. For this work, the parameters were calibrated in order to reproduce this dependency observed from several swelling pressure tests performed with the bentonite-based material of the sealing core.

Four phases were considered (see Figure 3). The first phase corresponds to the excavation, which induces an important extension of a damaged zone around the gallery. The second phase is the lining construction, which is placed immediately after the excavation. It consists of two layers: the external one is a compressible material constituted from the excavated argillite (20 cm), and the internal one is precast concrete (50 cm). The objective of the compressible material is to delay in time the increase of stresses in concrete and the simulation of its behaviour is crucial to assess the response of the entire system.

The third phase is called the waiting phase, which could last up to hundred years. During this period, the gallery remains empty, serving as a connection and circulation gallery while waiting for the sealing construction. The interaction between the host rock and the humidity conditions inside the gallery, and the creep strains of the rock must be taken into account. The last phase can be named "sealing or long term phase". Before sealing construction, the lining is partially removed at certain points to ensure the direct contact between the host rock and the expansive core. After that, the sealing materials are placed.

3
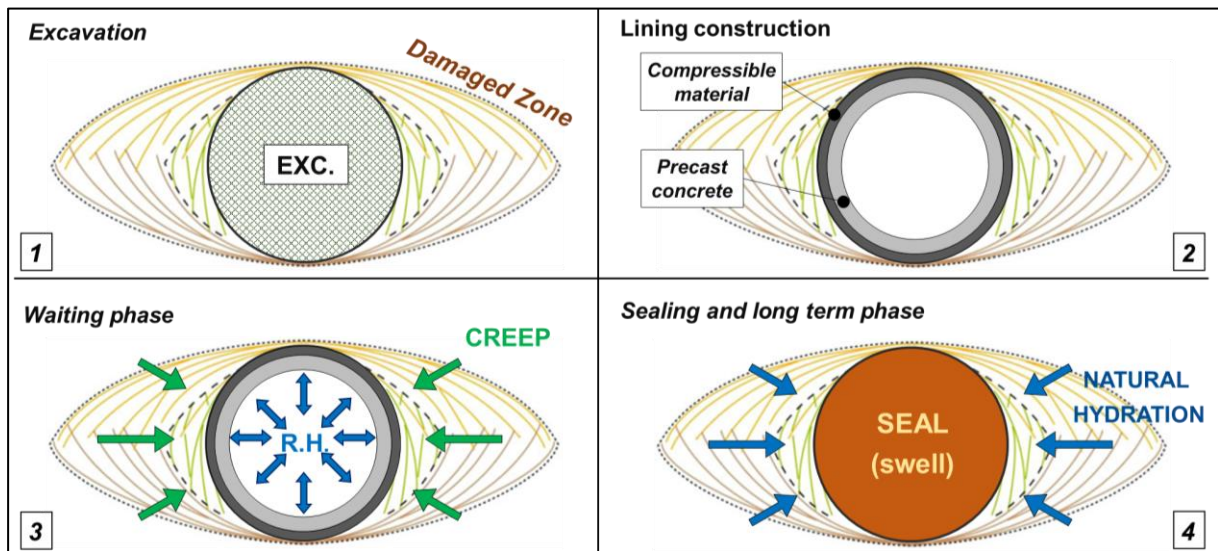
Figure 3: Main phases

3 RESULTS

In Figure 4 are presented the saturation degree evolution for several points within the core. It can be observed that almost all the points reach full saturation state more or less at the same time, around 1000 years after sealing construction. Differences observed between points during natural hydration process concerns the kinetics of hydration but not to the duration of it.

Longitudinal displacements of the plugs provide information on the global stability of the sealing system. This value always increases, even after the core has reached full saturation. It stabilizes around 2000 years after sealing construction, reaching a maximum value of around 0.5 m.

In Figure 5 are presented the time evolution of swelling pressure (radial and longitudinal components) for several points within the core. Due to the loss of density due to the plugs displacements, the swelling pressure obtained after the transition phase close to the plugs are limited: around 1 MPa and around 2 MPa for the longitudinal and radial component respectively. On the other hand, for the central part of the core, the performance appears to be much better, reaching a value of around 3 MPa for the radial component ($\approx$ 75% of the maximum swelling pressure corresponding to the initial dry density of the material).

Finally it is observed that the recompression of the damaged zone is effective in the part where the lining was removed and there is direct contact between the rock and the core.
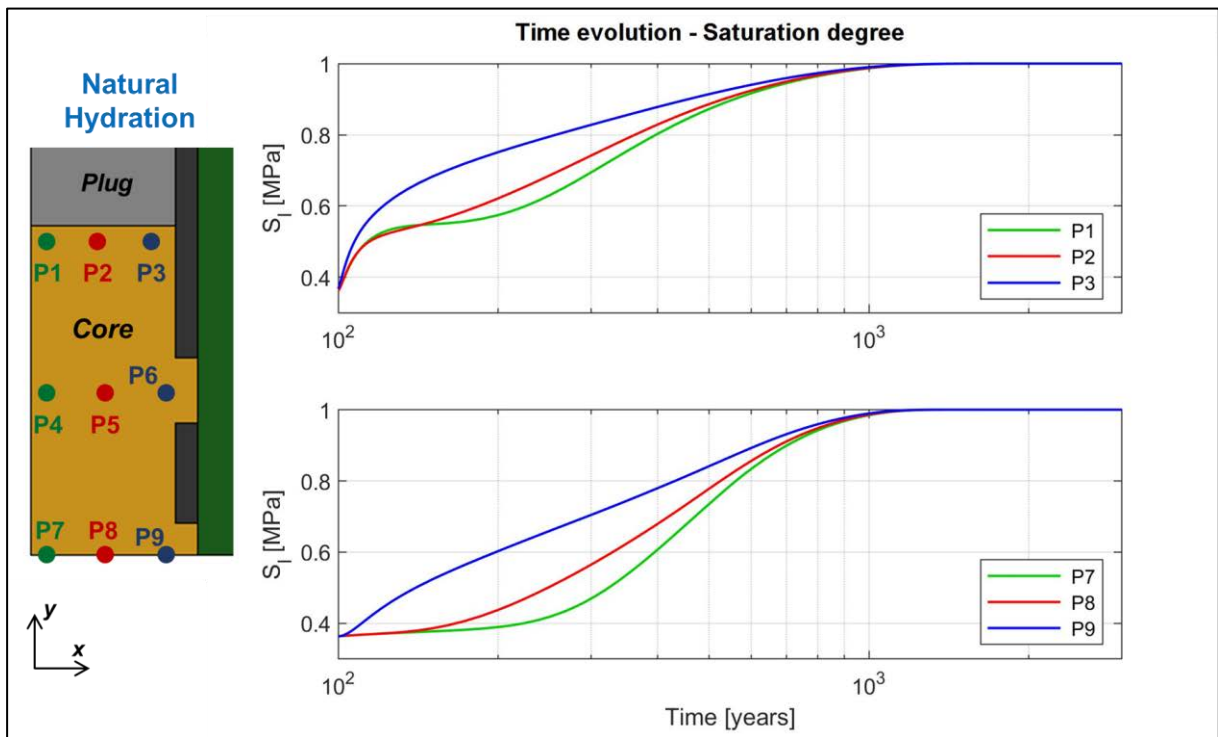
Figure 4: Time evolution - saturation degree
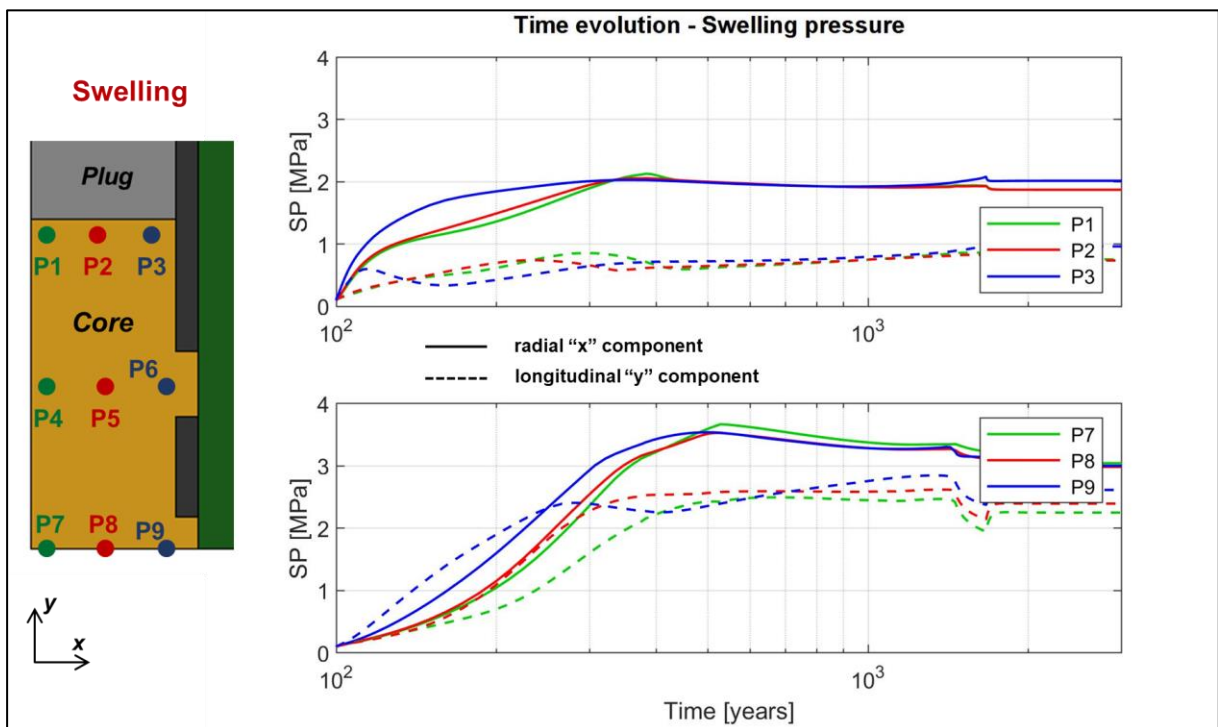
Figure 5: Time evolution - swelling pressure

5

11 CONCLUSIONS

The simulations presented provided qualitative and quantitative results on key aspects about the performance and integrity of the sealing systems, proving to be a useful tool to support the design of a safe nuclear waste repository. They also provide a step forward in addressing the complexity of the problem of gallery seals as settled in the current French nuclear waste disposal concept, by considering in the same simulation large 3D geometries, more realistic complex nonlinear and time-dependent constitutive laws, and crucial details like gaps and contacts between materials.

The main concluding remarks of this work include:

- The natural hydration phase is mainly controlled by COx permeability. Therefore, the expansive core as a whole reaches full saturation around 1000 years after sealing construction (for this diameter and host rock permeability).
- Relatively large displacements of the plugs are obtained (around 550 mm), and the bentonite core loses density near them. Despite this, a value of around 75% of the target swelling pressure in the radial direction is reached in the central part of the core.
- The recompression of the damaged zone is effective in the parts where the lining is removed.

REFERENCES

[i] Gens A. The role of geotechnical engineering for nuclear energy utilisation. In: Vanicek I et al., editors. Proc 13th European conference on soil mechanics and geotechnical engineering, vol. 3. Prague: CGtS; 2004. p. 25–67

[ii] Armand, G., Leveau, F., Nussbaum, C., de La Vaissiere, R., Noiret, A., Jaeggi, D., Landrein, P. & Righini, C. (2014). Geometry and properties of the excavation-induced fractures at the Meuse/ Haute-Marne URL drifts. Rock. Mech. Rock. Engng 47, No. 1, 21–41.

[iii] Mánica MA, Gens A, Vaunat J, Ruiz DF (2017). A time-dependent anisotropic model for argillaceous rocks. Application to an underground excavation in Callovo-Oxfordian claystone. Computers and Geotechnics 85, 341-350.

[iv] Mánica M.A., Gens A, Vaunat J., Ruiz D.F. 2018. Nonlocal plasticity modelling of strain localisation in stiff clays. Computers and Geotechnics 103, 138-150.

[v] Alonso E.E., Vaunat J., Gens A. 1999. Modelling the mechanical behaviour of expansive clays. Engineering Geology 54, 173–183.

IMPLEMENTATION OF A HYSTERETIC WATER RETENTION CURVE IN CODE_BRIGHT

Jean Vaunat[*], Ehsan Badakhshan[*] and Riccardo Scarfone[†]

[*] Department of Civil and Environmental Engineering
Technical University of Catalonia (UPC)
Campus Nord UPC, 08034 Barcelona, Spain

[†] Geotechnical Consulting Group, London, United Kingdom

Key words: Hysteresis, Water retention curve, Unsaturated soil, Low saturation degree.

Abstract. *The soil water retention curves (SWRC) present a relationship between the volumetric soil water content and the matric suction. SWRC plays a crucial role as input data for the simulation of unsaturated soils. Due to the inhomogeneity of the shapes and sizes of the pores in the soil skeleton, the ink bottle effect is an inevitable interaction for unsaturated soils. The wetting process relies on the larger pores, and drying depends on the smaller pores, which causes unsaturated soils to behave differently during wetting and drying paths. In this paper, the utilized hysteretic water retention curve (HWRC) based on the bounding surface approach is defined, and then the model is implemented in CODE_BRIGHT. The new HWRC model, ITYCL 20, is validated against the analytical solution.*

1 INTRODUCTION

The soil water retention curve (SWRC), which relates the saturation degree to a particular suction, plays an essential role in predicting the unsaturated soil behavior. The SWRC is an intrinsic principle for unsaturated soils to interpret the moisture migration conductivity, hydraulic, and water retention capacity [1,2]. The SWRCs for an unsaturated soil are related to several features such as the void ratio, soil fabric and texture, stress state, and connectedness of pore spaces, which makes the hysteresis effect. In other words, the SWRC relies on the path of saturation or desaturation. These two procedures make different SWRC, while at the same suction, the water content of the wetting branch is typically lower than the water content of a drying curve. This phenomenon is related to several reasons, and the most significant sake is the ink bottle effect [1-3]. The ink bottle effect relies on the inhomogeneity of the interconnected pores in terms of size and shape. In other words, the SWRC varies with the water flow process, which waters out (drying) or into (wetting) the soil skeleton. Smaller pores control the drying progress while the wetting process handles larger pores (large pores drain first but fill up last). The hysteretic water retention curve (HWRC) has a crucial influence on water flow and solute mobility in unsaturated porous media. Therefore, this paper briefly defines a new HWRC utilizing a bounding surface approach, improved at a low degree of saturation by Scarfone et al. [1]. Then, the new HWRC is implemented and validated in the CODE_BRIGHT, version 2022.

2 DESCRIPTION AND CHARACTERISTICS OF HYSTERETIC SWRC

For a typical soil, the SWRC for the wetting process from the initial stage of the oven-dry condition until the fully saturated situation is unique curve named the main wetting curve. In

the same way, the main drying curve is provided from a draining process of fully saturated soil until the soil is oven-dried. The drying and wetting processes of the water retention curves between oven-dried and saturated conditions make the scanning curves, as shown in Figure 1. These two main wetting and drying curves form the boundaries for all scanning curves, knowns as the bounding surface.

The proposed HWRC in this paper is also developed based on the concept of bounding surface, which associates the tangent of the scanning curves to the slope of the corresponding main curve at same value of saturation degree. The current version of the model, which is the focus of this paper, is only proposed for non-deformable unsaturated soils and thermohydraulic simulations, whereas the updated version of the model includes the effect of void ratio and deformation due to the suction changes.
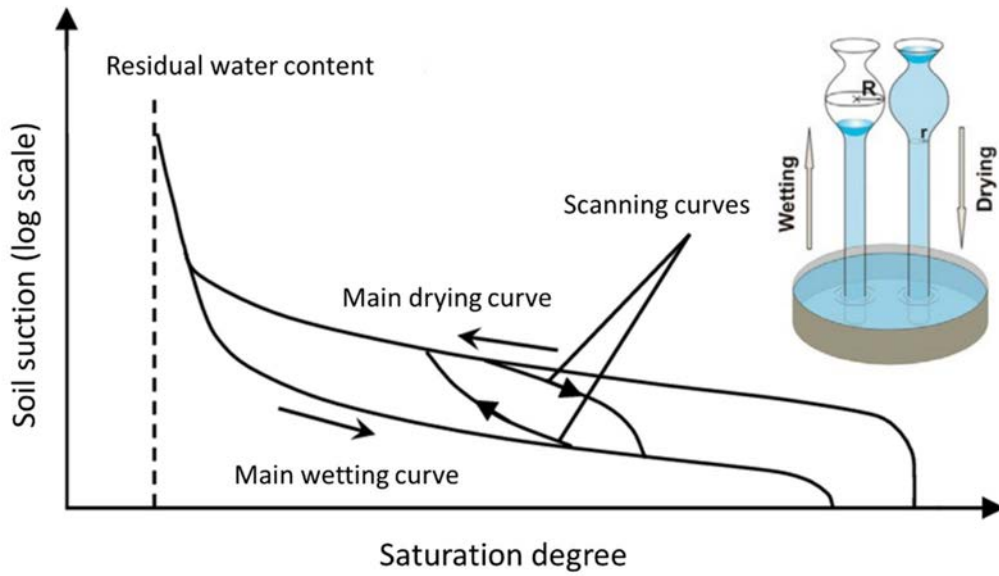
Figure 1: Schematic HWRC for different hydraulic paths.

2.1 Main drying and main wetting

The main drying and main wetting are based on the modified van Genuchten as:

$$S_l = S_{lr} + (S_{ls} - S_{lr}^{FS}).S_{le} \tag{1}$$

where S_l is the saturation degree, and S_{lr} and S_{ls} are the residual saturation degree and the maximum saturation degree, respectively, which are soil constants. S_{le} is the effective saturation degree, which is related to the suction (s) according to Equation (2) with a value between 0 (oven-dry condition) and 1 (saturated condition):

$$S_{le} = \left[1 + \left(\frac{s}{P}\right)^n\right]^{-m} \tag{2}$$

where P, σ_0, n and m are parameters of the model (soil constants). The m and n are corresponded as $m = 1-1/n$. To utilize the model for high suction or at low saturation degree the modified

residual saturation degree proposed by Fayer and Simmons [2] (S_{lr}^{FS}) is included:

$$S_{lr}^{FS} = S_{lr} \cdot \xi \cdot \ln\left(\frac{s_{dry}}{s}\right) \tag{3}$$

where ξ is a fitting parameter, s_{dry} is the suction at oven-dried condition, i.e. $s_{dry} = 1$ GPa. Gallipoli [3] proposed a power law for parameter P_0 in the base van Genuchten model. Also, the Gallipoli equation represents an interesting contribution towards taking to account the effect of void ratio, but its results is unrealistic when used to model cyclic variations of suction. Hence, based on the regression analysis, the following relationships are considered that better consider the dependency of degree of saturation not only on suction but also on deformation.

$$P_d = P_{0d} \frac{e^{-\psi_d}}{n_d m_d \phi_d} \frac{\sigma}{\sigma_0} \quad \text{(for drying)} \quad ; \quad P_w = P_{0w} \frac{e^{-\psi_w}}{n_w m_w \phi_w} \frac{\sigma}{\sigma_0} \qquad \text{(for wetting)} \tag{4}$$

2.2 Scanning retention curves

Scanning retention curves are modelled using a bounding surface approach by considering that the gradient of a scanning drying curve and the gradient of a scanning wetting curve are related to the corresponding gradient of the main drying curve or main wetting curve, respectively as:

$$\left(\frac{dS_{le}}{d\ln s}\right)_d = \left(\frac{s}{s_d}\right)^{\gamma d} \left(\frac{dS_{le}}{d\ln s_d}\right)_{Md} \qquad \text{for drying} \tag{5}$$

$$\left(\frac{dS_{le}}{d\ln s}\right)_w = \left(\frac{s}{s_w}\right)^{\gamma w} \left(\frac{dS_{le}}{d\ln s_w}\right)_{Mw} \qquad \text{for wetting} \tag{6}$$

Image values of suction s_d and s_w in terms of the current effective degree of saturation S_{le} results in:

$$s_d = \frac{e^{-\psi_d}}{n_d m_d \phi_d}\left(S_{le}^{-1/m_d} - 1\right)^{\frac{1}{n_d}} \qquad \text{for drying} \tag{7}$$

$$s_w = \frac{e^{-\psi_w}}{n_w m_w \phi_w}\left(S_{le}^{-1/m_w} - 1\right)^{\frac{1}{n_w}} \qquad \text{for wetting} \tag{8}$$

By combination of s_d and s_w in gradients,

$$S_{led} = \left\{1 + \left[\frac{(s^{\gamma d} - A_d)^{1/\gamma d}}{\dfrac{e^{-\psi_d}}{n_d m_d \phi_d}}\right]^{nd}\right\}^{-md} \qquad \text{for drying} \tag{9}$$

3

$$S_{lew} = \left\{ 1 + \left[\frac{\left(s^{\gamma w} - A_d \right)^{1/\gamma w}}{\dfrac{e^{-\psi_w}}{n_w m_w \phi_w}} \right]^{nw} \right\}^{-mw} \qquad \text{for wetting} \qquad (10)$$

where, the integration constants A_d and A_w are calculated by imposing the condition that the scanning curve passes through the reversal point (s_0, S_{le0}).

$$A_d = s_0^{\gamma d} - \left[\frac{e^{-\psi_d}}{n_d m_d \phi_d} \left(S_{le0}^{-1/md} - 1 \right)^{1/n_d} \right]^{\gamma d} \qquad \text{for drying} \qquad (11)$$

$$A_w = s_0^{\gamma w} - \left[\frac{e^{-\psi_w}}{n_w m_w \phi_w} \left(S_{le0}^{-1/mw} - 1 \right)^{1/n_w} \right]^{\gamma w} \qquad \text{for wetting} \qquad (12)$$

and

$$S_{le0} = \frac{S_{l0} - \xi_d \ln\left(\dfrac{s_{dry}}{s} \right)}{S_{lsd} - \xi_d \ln\left(\dfrac{s_{dry}}{s} \right)} \qquad \text{for drying} \qquad (13)$$

$$S_{le0} = \frac{S_{l0} - \xi_w \ln\left(\dfrac{s_{dry}}{s} \right)}{S_{lsw} - \xi_w \ln\left(\dfrac{s_{dry}}{s} \right)} \qquad \text{for wetting} \qquad (14)$$

Therefore, the variation of S_l along a scanning drying curve (S_{ld}) or a scanning wetting curve (S_{lw}) is given by:

$$S_{ld} = \xi_d \ln\left(\frac{s_{dry}}{s} \right) + \left[S_{lsd} - \xi_d \ln\left(\frac{s_{dry}}{s} \right) \right] S_{led} \qquad \text{for drying} \qquad (15)$$

$$S_{lw} = -\xi_w \ln\left(\frac{s_{dry}}{s} \right) + \left[S_{lsd} + \xi_w \ln\left(\frac{s_{dry}}{s} \right) \right] S_{lew} \qquad \text{for wetting} \qquad (16)$$

3 IMPLEMENTATIONS IN CODE_BRIGHT

In CODE_BRIGHT, the physical properties are functions of the different unknowns as gas pressure (pg), liquid pressure (pl), and temperature (T). Also, every constitutive law is identified by two codes: ICL and ITYCL. The code ICL characterizes the type of constitutive law (e.g., for the SWRC, ICL=6). The code ITYCL describes the specific model utilized for the constitutive laws (e.g., for the current implemented hysteretic retention curve, ITYCL=20).

The "hyst_liquid_saturation" subroutine is written in the code by consuming several assumptions on the material parameters. Firstly, for the maximum saturation degree and

4

residual saturation degree the same values are selected for wetting and drying, i.e., $S_{ls,w}=S_{ls,d}=S_{ls}$ and $S_{lr,d}=S_{lr,w}=S_{lr}$, respectively. Secondly, the slopes of the main wetting and drying curves are the same, i.e., $m_w=m_d=m$. Finally, the main wetting and drying curves coincide in the pendular state, i.e., $\xi_d = \xi_w = \xi$. History variables are the hydraulic state at the previous time step (s_0 and S_{l0}) and the current parameters of the unknowns (T, pg, and pl). This subroutine is activated in the code by the value corresponding to the flag parameter iopthys (=1 for the hysteretic model, =0 for the non-hysteretic model). By making some changes in the Trans code, the model is adjusted hysteretic (1 is assigned to iopthys) if ITYCL=20 (HWRC model), and else, the model is assumed non-hysteretic (0 is assigned to iopthys). If the suction value ($pg-pl$) is $s > 0$, the soil is in an unsaturated condition, and the subroutine identifies the current hydraulic state on whichever drying or wetting curve. If $s > s_0$, the suction at the current step is higher than the previous step, the current hydraulic state is on a drying curve, otherwise, it is on a wetting curve. Moreover, some partial derivatives as $\partial S_{le}/\partial s$, $\partial S_{le}/\partial P_{0d}$ or $\partial S_{le}/\partial P_{0w}$, $\partial A_d/\partial P_{0d}$ or $\partial A_w/\partial P_{0w}$, and $\partial P_{0d}/\partial \sigma$ or $\partial P_{0w}/\partial \sigma$ should be computed at this point. These derivatives are utilized at the end of the subroutine for computing $\partial S_l/\partial T$, $\partial S_l/\partial pg$, and $\partial S_l/\partial pl$. Table 1 demonstrates the parameters required to utilize the hysteretic water retention model implemented in the CODE_BRIGHT.

Model	P1	P2	P3	P4	P5	P6	P7	P8	P9	P10
HWRC	P_{0d}	σ_0	m	$S_{lr}.\xi$	S_{ls}	P_{0w}	γ_d	s_0	S_{l0}	γ_w
ICL=6, ITYCL=20	MPa	Nm^{-1}	-	-	-	MPa	-	MPa	-	-

Table 1: Parameters for the HWRC implemented in CODE_BRIGHT.

4   VALIDATION OF THE IMPLEMENTED MODEL

The implementation validation of the new HWRC model is ensured through some numerical tests, which one of these tests is provided in this chapter. A 2D simulation, at constant $pg=0.1$ MPa and $T=20$°C, is conducted considering a 5×10 cm specimen of soil, illustrated in Figure 2. The used parameters are presented in Table 2. The initial conditions in the first interval are a uniform distribution of pore-liquid pressure with $pl=0.08$ MPa corresponding to the suction value of $s=0.02$ MPa. Twelve cycles of drying and wetting are considered beginning from the $pl=0.08$ MPa applying the same time history of pore-liquid pressure, pl, at all elements as a flux boundary condition.

In the Figure 3, the liquid saturation degree obtained through the CODE_BRIGHT simulations are compared with the hydraulic paths computed analytically by the same material parameters. It is clear that the implemented model can precisely predict the various cycles involving the main wetting and main drying curves and scanning curves. The accurate coincidence of the numerical results and analytical solution confirmed the implementation validation of the new HWRC model in the CODE_BRIGHT.
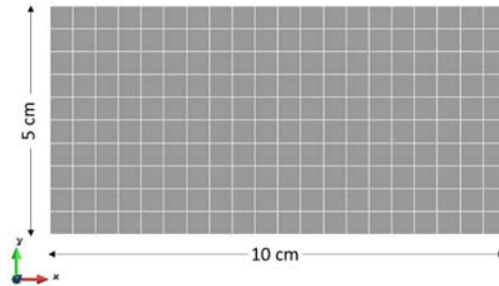
Figure 2: Mesh and geometry of the model.

Model	P1	P2	P3	P4	P5	P6	P7	P8	P9	P10
HWRC	0.01962	0	0.5	0.0268	1	0.00491	3	0.01	0.685	3
ICL=6, ITYCL=20	MPa	Nm^{-1}	-	-	-	MPa	-	MPa	-	-

Table 2: HWRC Model parameters for the implementation validation in CODE_BRIGHT.
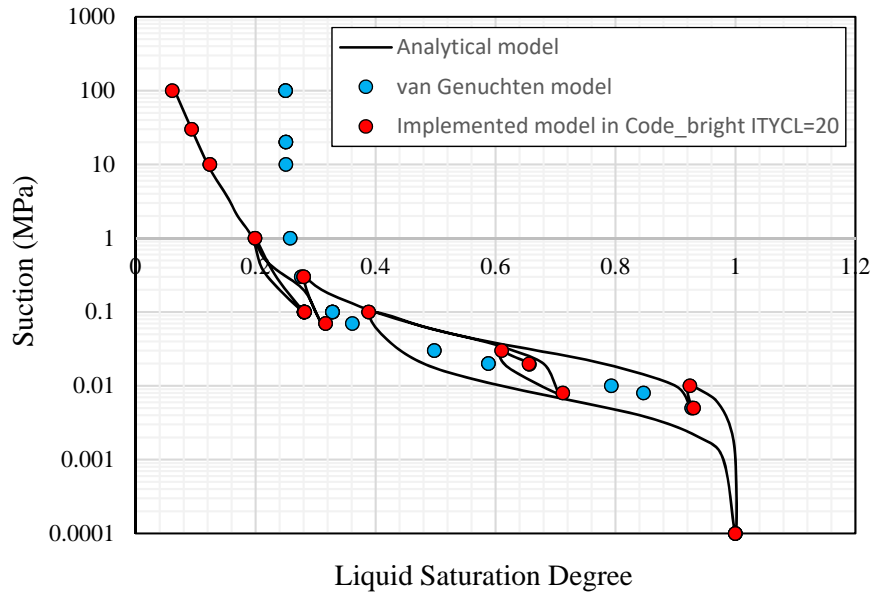
Figure 3: Comparison between the CODE_BRIGHT results with the hydraulic paths computed analytically.

5 CONCLUSIONS

A hysteretic soil water characteristic model using a bounding surface approach is implemented in this paper to predict the behavior of unsaturated soils. The new HWRC for calculating the scanning wetting and drying curves requires the inverse function of the main wetting and main drying curves at the position of the last reversal point (s_0, S_{l0}). The new model is implemented as ICL=6 and ITYCL=20 by a new subroutine named "hyst_liquid_saturation". The input parameters of this subroutine are P_{0d}, P_{0w}, σ_0, m, $S_{lr}.\xi$, S_{ls}, γ_d, and γ_w. The (s_0, S_{l0}) only to initialize the model at the beginning of the analysis are input manually at the first interval, while during the process, these two parameters are recorded from the previous time step as a history variable. The comparison between the numerical simulation through the implemented HWRC and the analytical solution, shows the accuracy of the implementation process.

REFERENCES

[1] Scarfone, R., Simon, J., Wheelera, M., 2020. A hysteretic hydraulic constitutive model for unsaturated soils and application to capillary barrier systems. Geomechanics for Energy and the Environment, In Press.

[2] Fayer, M.J., Simmons, C.S., 1995. Modified soil water retention functions for all matric suctions. Water Resour Res., 31(5), 1233:1238.

[3] Gallipoli, D., 2012. A hysteretic soil-water retention model accounting for cyclic variations of suction and void ratio. Géotechnique, 62(7), 605:616.

MODELLING OF LONG-TERM INTERACTIONS BETWEEN IRON AND BENTONITE

M. Carme Chaparro[*], Nicolas Finck[*], Volker Metz[*] and Horst Geckeis[*]

[*] Institute for Nuclear Waste Disposal (INE),
Karlsruhe Institute of Technology (KIT),
P.O. Box 3640, 76021 Karlsruhe, Germany
E-mail: carme.chaparro@kit.edu

Key words: Reactive Transport, Radioactive Waste Disposal, Numerical Model

Abstract. *A 1D radial reactive transport model has been developed in order to better understand the processes occurring during long-term iron-bentonite interaction. The numerical model takes into account diffusion, aqueous complexation reactions, mineral dissolution/precipitation and cation exchange at a constant temperature of 25 ºC under anaerobic conditions. Our results reveal that Fe is retained by montmorillonite via cation exchange in the short-term, and it is consumed by formation of secondary phases in the long-term. Results also show a significant increase of pH in the long-term. The numerical model predicts precipitation of nontronite, magnetite and greenalite as corrosion products. Calcite precipitates due to Ca release from montmorillonite consecutive to cation exchange with Fe in the short-term and due to montmorillonite dissolution in the long-term. Dissolution/precipitation reactions result in limited variations of the porosity.*

1 INTRODUCTION

Geological disposal in deep bedrock repositories is the preferred option for long-term management of high-level radioactive waste. In some of these multi-barrier disposal concepts for argillaceous and crystalline host rocks, carbon steel is considered as potential canister material and bentonites are planned as backfill material to protect the canisters and to prevent radionuclides from migrating to the far-field following an eventual canister failure. Groundwater will saturate the bentonite, thus, reactive transport processes such as diffusion due to chemical gradients, mineral dissolution/precipitation and adsorption will occur. These processes result in considerable alterations of the bentonite and the canister. Hence, deep understanding of reactive transport processes that will occur during the long-term of high-level radioactive waste disposal is imperative in order to test and demonstrate the long-term safety of the final disposal system. To do so, reactive transport models have been developed with the objective to study canister-bentonite interactions at repository scale[i]. Due to the lack of long-term experimental data, our results are compared with other published numerical studies on iron-clay / bentonite interaction[ii,iii,iv].

2 REACTIVE TRANSPORT MODEL

The simulations are carried out using Retraso-CodeBright[v]. Our conceptual model considers a cylindrical carbon steel canister surrounded by bentonite (Figure 1). For simplification, we assume that carbon steel is composed only of metallic iron, which is the main phase of carbon steel.
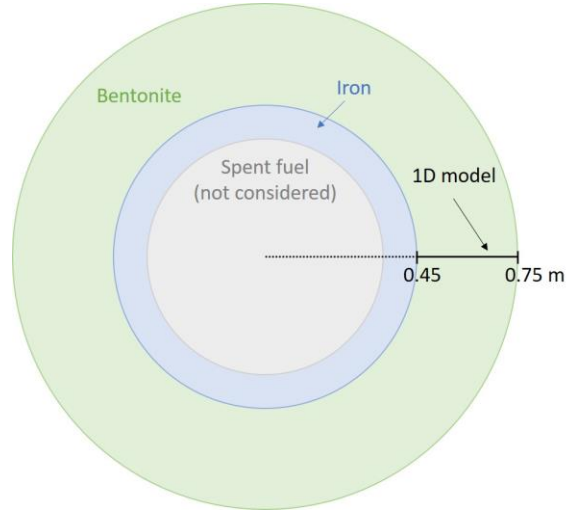
Figure 1: Geometry and materials of the 1D radial model. The axisymmetric model considers the iron-bentonite interface at x=0.45 m, and a thickness of 0.3 m of bentonite (from x=0.45 to x=0.75 m).

The conceptual model assumes that the bentonite is fully water-saturated and the heat pulse of the high-level waste is already dissipated, therefore anaerobic conditions at a constant temperature of 25ºC are considered. The model accounts for diffusion as transport mechanism, iron corrosion, aqueous complexation reactions, mineral dissolution/precipitation and cation exchange reactions. Therefore, the mass balance of reactive transport can be written as:

$$\mathbf{U}_a \frac{\delta \varphi \rho_l c_a}{\delta t} + \mathbf{U}_d \frac{\delta \varphi \rho_l c_d}{\delta t} + \mathbf{U}_m \frac{\delta (1-\varphi) \rho_s c_m}{\delta t} = \mathbf{U}_a i(c_a) + \mathbf{U} \mathbf{S}_k^t r_m(c_a) \tag{1}$$

Where φ is the porosity, ρ_l and ρ_s are the liquid and solid densities, respectively (kg m^{-3}). Vectors c_a, c_d and c_m (mol kg^{-1}) are the concentrations of aqueous species, adsorbed species and minerals respectively. Matrix $\mathbf{S}_k^t$ and vector r_m contain the stoichiometric coefficients and the rates of the kinetic reactions, which can be considered as functions of all aqueous concentrations. Matrices $\mathbf{U}_a$, $\mathbf{U}_d$ and $\mathbf{U}_m$ are called the component matrices for aqueous, adsorbed and mineral species and relate the concentrations of the species with the total concentrations of the components. The matrix $\mathbf{U}$ is the component matrix for all species. These matrices can be computed from the stoichiometric coefficient of the chemical reactions. i is the diffusion term, and according to Fick's law[vi] can be written as:

$$i(c_a) = \nabla \cdot (D_p \varphi \rho_l \nabla(c_a))$$
$$D_p = \tau 1.1 \text{x} 10^{-4} \exp\left(\frac{-24530}{R(273.15 + T)}\right) \tag{2}$$
$$D_e = \varphi D_p$$

where D_p is the molecular diffusion coefficient in porous media (m^2 s^{-1}), τ is the tortuosity factor, $R = 8.31$ J mol^{-1} K^{-1}, T is the temperature (ºC) and D_e is the effective diffusion coefficient (m^2 s^{-1}).

The bentonite considered here is MX-80 with the mineral composition and the volumetric fractions of each mineral as reported in literature[vii]. The primary phases considered are montmorillonite, quartz, muscovite, albite, illite, pyrite and calcite. Reported corrosion products that were found experimentally[viii,ix,x] are considered as potential secondary phases, consisting of magnetite, greenatite, cronstedtite, Na-nontronite, Mg-nontronite and siderite. The

2

initial porewater used in the numerical model corresponds to a clay groundwater[ix] equilibrated with montmorillonite, because it is the main phase of the bentonite. The thermodynamic data is taken from the Geochemist's Workbench database thermo.com.V8.R6.full[xi]. We consider a constant iron corrosion rate of 2µm/year. The kinetic data of other mineral reactions are the same as in recent reported modelling studies[ii,iii,iv].

3 RESULTS AND DISCUSSION

3.1 Solution composition

The numerical model results show that during the first 100 years, the Fe concentration in the porewater increases due to iron dissolution. However, Fe is partly adsorbed by montmorillonite and partly consumed by formation of Fe-bearing secondary phases (magnetite and nontronite). At 1000 years the aqueous Fe concentration decreases considerably in the porewater because it is mainly consumed by formation of secondary phases (magnetite, nontronite and greenalite) rather than being adsorbed. The aqueous Si concentration increases in the short-term due to dissolution of montmorillonite and other (alumo-)silicates of bentonite, in the long-term it decreases because of the relatively rapid precipitation rate for Fe-silicates and the slow dissolution rate of montmorillonite. The Ca and HCO_3^- concentrations in solution decrease with time due to calcite precipitation. The pH of the porewater increases progressively from 7.5 to 10.9 because dissolution of metallic iron and bentonite minerals (such as montmorillonite and feldspar) consume protons. Such an increase in pH has also been reported in literature[ii].

3.2 Mineral composition of the bentonite

The model predicts dissolution of primary minerals of bentonite that dissolve because increase in pH makes the alumosilicate unstable. Montmorillonite dissolution releases Ca yielding calcite precipitation, however, especially in the first 100 years, Ca in the montmorillonite interlayer can also be exchanged by Fe and thereby likewise induce calcite precipitation. Dissolution of the primary mineral phases of bentonite as well as precipitation of calcite are more prominent at 10,000 years when the pH is higher. The corrosion products predicted by the numerical model are nontronite, magnetite and greenalite (Figure 2). At 5 years, nontronite precipitates because Fe and Si are available in the porewater due to dissolution of metallic iron and of primary minerals of bentonite, respectively. Magnetite starts precipitating at 100 years when enough Fe is available in the porewater. At 1000 years, Mg-nontronite and magnetite are the principal corrosion products of the system. However, at 10,000 years, magnetite and nontronite dissolve, then, Fe and Si are consumed by precipitation of greenalite, which is then the main corrosion product. The secondary Fe-bearing minerals (nontronite, magnetite and greenalite) precipitate quite close to the iron-bentonite interface, and calcite also precipitates along the first 5 cm. The numerical model does not predict neither precipitation of cronstedtite nor that of siderite. Precipitation of magnetite, calcite and greenalite has been recently found in the Iron Corrosion in Bentonite (IC-A) experiment in the Mont-Terri laboratory (Switzerland)[x], which supports our numerical results. Other iron corrosion experiments reported in literature[viii,ix], which were performed at 90ºC with Callovo-Oxfordian clay, also found precipitation of siderite and cronstedtite. Thus, the temperature, bentonite and porewater compositions could have a significant impact on the nature of formed corrosion products.
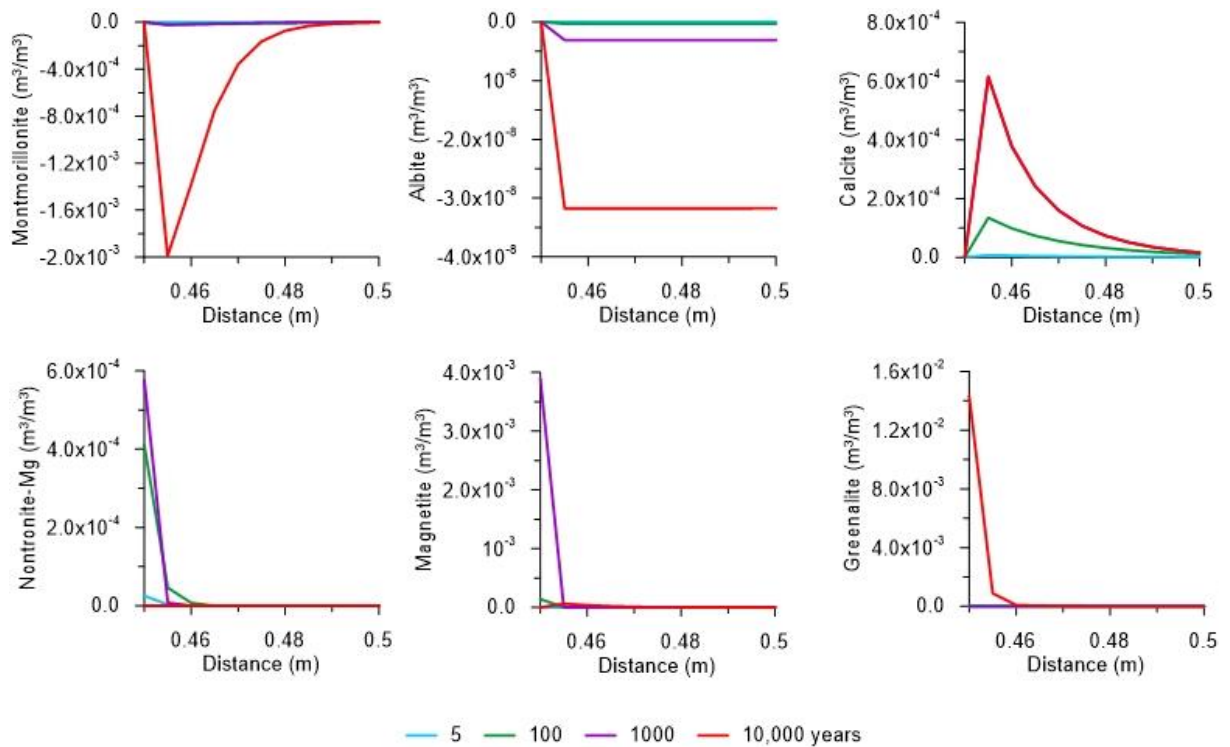
Figure 2: Volumetric fraction of minerals against distance for the reference model ($r_c=2\mu m\ y^{-1}$). For the primary mineral phases of bentonite (montmorillonite, albite and calcite) the variation of the volumetric fraction is plotted. The interface between iron and bentonite is at 0.45m. Results at 5, 100, 1000 and 10.000 years are compared.

3.3 Porosity

In general, the model does not predict considerable changes in porosity, being unnoticeable after 5 years (Figure 3). At the end of the calculations, at 10,000 years, there is a decrease in porosity right after the interface due to the precipitation of greenalite, followed by an increase of porosity due to dissolution of montmorillonite. Dissolution of montmorillonite and precipitation of greenalite take place at the same time, both with similar pore volumes, therefore, calculated changes in porosity are only marginal.
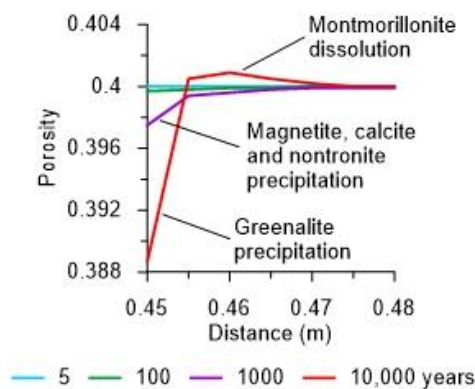
Figure 3: Porosity versus distance for the reference model ($r_c=2\mu m\ y^{-1}$). The interface between iron and bentonite is at 0.45m. Results at 5, 100, 1000 and 10.000 years are compared.

4

4 SENSITIVITY ANALISIS

A sensitivity analysis has also been performed to study the effect of selected parameters, such as corrosion rate, diffusion coefficient and composition of the porewater, on the corrosion products. Results from the sensitivity analysis suggest that a larger corrosion rate would provoke a rapid precipitation of greenalite due to the rapid Si supply from the dissolution of primary (alumo-)silicate minerals of bentonite. On the contrary, when a lower corrosion rate is considered, the model predicts lower dissolution of these bentonitic minerals, hence only nontronite and magnetite precipitate. When a larger diffusion coefficient is considered, transport dominates, therefore, a larger thickness of the alteration zone is predicted, but with less mineral dissolution / precipitation. The composition of the porewater can affect the secondary phases forming during the iron-bentonite interaction: if concentration of Si in the porewater is larger, then Fe-silicates will be more relevant rather than magnetite.

5 CONCLUSIONS

- Results from the 1D reactive transport model suggest that Fe is partly adsorbed in the short-term, and consumed by corrosion products in the long-term.
- Calcite precipitates due to Ca / Fe cation exchange in the short-term and due to montmorillonite dissolution in the long-term.
- The main secondary phases formed in the long-term are magnetite and greenalite.
- Porosity slightly decreases at the iron / bentonite interface due to greenalite precipitation, and then slightly increases because of montmorillonite dissolution.
- Results of the sensitivity analysis reveal that higher Si contents in the porewater, due to higher corrosion rate or a different porewater composition, can affect the secondary phases forming during the iron-bentonite interaction, Fe-silicates being more relevant rather than magnetite. On the contrary, when a lower corrosion rate is considered, only nontronite and magnetite precipitate.
- Our results can differ from other reactive transport calculations reported in the literature because of the assumptions considered in the conceptual model, such as the selected secondary phases, considering the canister as porous material or the temperature of the system.

REFERENCES

[i]   Chaparro, M.C., N. Finck, V. Metz, H. Geckeis, 2021. Reactive Transport Modelling of the Long-Term Interaction between Carbon Steel and MX-80 Bentonite at 25ºC. Minerals, 11, 1272. doi:10.3390/min11111272.

[ii] Bildstein, O., L. Trotignon, M. Perronnet, M. Jullien, 2006. Modelling iron-clay interactions in deep geological disposal conditions. Physics and Chemistry of the Earth, Parts A/B/C, 31, 618:625. doi:10.1016/j.pce.2006.04.014.

[iii] Wilson, J.C., S. Benbow, H. Sasamoto, D. Savage, C. Watson, 2015.Thermodynamic and fully-coupled reactive transport models of a steel-bentonite interface. Applied Geochemistry, 61, 10:28. doi: 10.1016/j.apgeochem.2015.05.005.

[iv] Samper, J., A. Naves, L. Montenegro, A. Mon, 2016. Reactive transport modelling of the long-term interactions of corrosion products and compacted bentonite in a HLW repository

in granite: Uncertainties and relevance for performance assessment. Applied Geochemistry, 67, 42:51. doi:10.1016/j.apgeochem.2016.02.001.

[v] Saaltink, M.W., F. Batlle, C. Ayora, J. Carrera, S. Olivella, 2004. RETRASO, a code for modeling reactive transport in saturated and unsaturated porous media. Geol. Acta, 2, 235:251.

[vi] Olivella, S., A. Gens, J. Carrera, E.E. Alonso, 1996. Numerical formulation for a simulator (CODE_BRIGHT) for the coupled analysis of saline media. Eng. Comput. 13, 87:112. doi:10.1108/02644409610151575.

[vii] Karnland, O, 2010. Chemical and Mineralogical Characterization of the Bentonite Buffer for the Acceptance Control Procedure in a KBS-3 Repository. Technical Report SKB-TR-10-60.

[viii] Schlegel, M.L., C. Bataillon, F. Brucker, C. Blanc, D. Prêt, E. Foy, M. Chorro, 2014. Corrosion of metal iron in contact with anoxic clay at 90ºC: Characterization of the corrosion products after two years of interaction. Applied Geochemistry, 51, 1:4. doi:10.1016/j.apgeochem.2014.09.002.

[ix] Martin, F., C. Bataillon, M. Schlegel, 2008. Corrosion of iron and low alloyed steel within a water saturated brick of clay under anaerobic deep geological disposal conditions: An integrated experiment. J. Nucl. Mater. 379, 80:90. doi:10.1016/j.jnucmat.2008.06.021.

[x] Morelová, N., D. Schild, F. Heberling, N. Finck, K. Dardenne, V. Metz, H. Geckeis, 2021. Anaerobic Corrosion of Carbon Steel in Compacted Bentonite Exposed to Natural Opalinus Clay Porewater: Bentonite Alteration Study. Goldschmidt Virtual.

[xi] Johnson, J., S. Lundeen, 1994. GEMBOCHS Thermodynamic Datafiles for Use with the EQ3/6 Software Package; Technical Report, Yucca Mountain Laboratory, Milestone Report M0L72.

COUPLED MODELLING OF ENVIRONMENTAL IN-SOIL CONDITIONS AND THEIR EFFECTS OVER POLYESTER STRAPS REINFORCED SOIL STRUCTURES

A. Moncada[*†], I.P. Damians[*†], S. Olivella[*†] and R.J. Bathurst[§]

* Department of Civil and Environmental Engineering (DECA), Universitat Politècnica de Catalunya·BarcelonaTech (UPC); Campus Nord UPC, 08034 Barcelona, Spain
Email : anibal.moncada@upc.edu

† International Centre for Numerical Methods in Engineering (CIMNE)
Campus Nord UPC, 08034 Barcelona, Spain (http://www.cimne.com)

§ Geoengineering Centre at Queen's-RMC, Civil Engineering Department, Royal Military College of Canada, Canada

Abstract. *Polyester (PET) strap reinforcement materials are being routinely used as soil reinforcement for mechanically stabilized earth (MSE) walls. Strength and stiffness of the polyester fibres can be expected to decrease with increasing temperature and in the presence of moisture. By using numerical simulations, mean in-soil temperature values could be approximated to the mean atmospheric yearly value with diminishing fluctuation with increased depth. In-depth relative humidity values were found to present a constant behaviour for three of the four imposed boundary condition. Temporal variations in the response of PET straps were adequately modelled with viscous models within different soil environments.*

1 INTRODUCTION

In polyester (PET) reinforced mechanically stabilized earth (MSE) wall structures, the critical role of temperature and relative humidity on the mechanical and chemical degradation of PET fibres due to hydrolysis is well documented in the literature [i], [ii]. Strength and stiffness of the PET fibres can be expected to decrease with increasing temperature and in the presence of moisture. These reductions modify the partial factor for creep and chemical degradation that is used in internal stability limit state design for PET strap MSE walls. Hence, local atmospheric and in-soil conditions should be accounted for at the design phase.

In order to analyze the long-term behaviour of PET straps, the present study proposes a coupled finite element model based on the software CODE_BRIGHT [iii] in which the in-soil distribution of temperature and relative humidity for four different atmospheric conditions are evaluated first. Next, visco-elastic and visco-plastic models are implemented to simulate PET strap long-term response calibrated using the laboratory results of You-Kyum et al. [iv] for GECO's FASTEN FS products [v]. Finally, a 2D linear coupled thermo-hydro-mechanical (THM) MSE wall model is proposed as a preliminary approach.

2 NUMERICAL MODEL

The mesh geometry and components of the thermal-Hydraulic coupled (TH) model is presented in Figure 1, composed of 5536 structural quadrilateral elements with 5714 nodes. The proposed model included all mechanical elements such as the 1.5 m-high concrete facing

panels, the 20 mm-thick bearing pads and the 3 mm-thick PET reinforcement layers with 0.7H length. The water table was located at 10 m from the base of the model. The bottom base temperature was constant at +2°C higher than the mean annual temperature reported from the atmospheric temperature registry used for each analysis. Staged construction was not used in this study as to simplify the model.
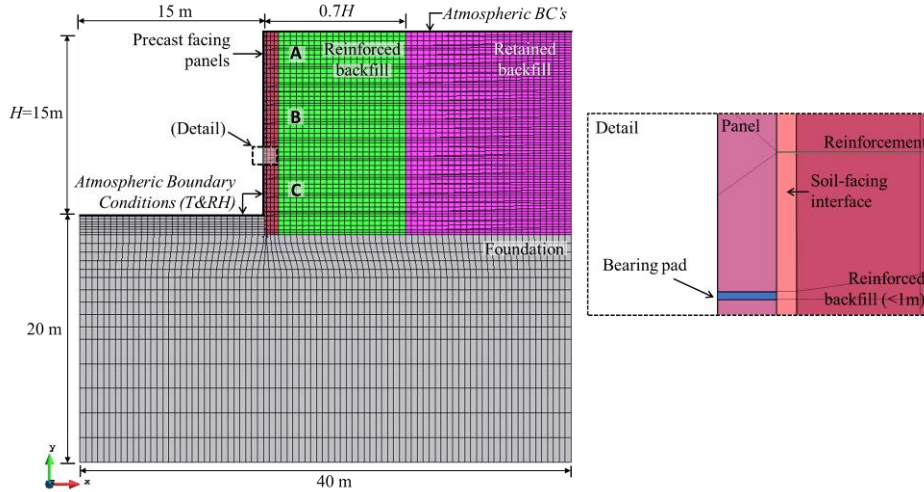
Figure 1: 2D model domain and finite element mesh used for analyses.

Boundary conditions (BC) consist of atmospheric in-air data records composed of real time series data of temperature (T) and relative humidity (RH) for each control location [vi] over the upper boundaries. To compare and analyze results, points A, B and C, located 2 m from facing and at 1, 7 and 14 m-depth, respectively, were selected. BC included four different geographic locations, corresponding to continental (Toronto), Mediterranean (Barcelona), desert (Abu Dhabi) and tropical (Singapore) climates. Analyses for each model were for 5-year periods using daily records from years 2016 through 2020.

A granular soil was considered in this study. Soil thermal dispersion is modeled by Fick´s law with horizontal and vertical dispersivity of $d_l = 5$ m and $d_t = 0.5$ m. Thermal conductivity was modelled using Fourier´s law, with dry and saturated conductivity values of $\gamma_{dry} = 0.5$ W/mK and $\gamma_{sat} = 1$ W/mK. Default values for solid phase specific heat ($c_s = 1000$ Jkg^{-1}K^{-1}) and density ($\rho_s = 2700$ kgm^{-3}) were used. Water retention curve (Van Genuchten model) for soil and concrete facing panels was modelled with a reference pressure $P_0 = 0.005$ MPa and $P_0 = 0.001$ MPa and shape parameter $\lambda = 0.8$ and $\lambda = 0.4$ respectively. Initial porosity values of $\phi_0 = 0.3$, $\phi_0 = 0.15$, $\phi_0 = 0.01$ and $\phi_0 = 0.4$ and intrinsic permeability values of $K = 1\times10^{-12}$, $K = 1\times10^{-12}$, $K = 1\times10^{-16}$ and $K = 1\times10^{-10}$ were considered for soil, precast facing panels, PET strap reinforcement layers and HDPE materials respectively. Values for the PET strap reinforcement layers, precast facing panels and HDPE bearing pads have been adjusted to equivalent values for a 2D plane strain 1-m slice.

To incorporate in-soil conditions over the PET strap reinforcement behavior, temperature- and saturation-dependent visco-elastic (VE) and vico-plastic (VP) constitutive models were used to account for creep and strain softening over long-term constant load, respectively. The mechanical parameters used to model the PET straps are presented in Table 1. Stiffness was calculating considering an average width of 89 mm per strap and two connections every 2.5 m in the wall face direction. A linear model with an elastic modulus E=32 GPa and Poisson´s

ratio ν=0.2 was used for the precast concrete facing panels. Two scenarios were analyzed to model laboratory obtained creep master curves. First, elements with bi-linear elastic moduli and VE properties were subjected to an initial tension, followed by a ramp increase up to the desired load representing a selected fraction of the ultimate tensile strength (UTS). Second, elements with linear elastic modulus, VE and VP properties were subjected to a constant initial load.

Table 1: Model parameters for PET strap reinforcement.

Constitutive model	Parameter	Value
Linear elasticity	Elastic modulus, E [MPa]	$2.2 - 4.8$
	Poisson's ratio, ν [-]	$0.30 - 0.34$
Bi-linear elasticity	1st elastic modulus, E_1 [MPa]	$1.7 - 3.9$
	2nd elastic modulus, E_2 [MPa]	$45 - 100$
	Poisson ratio, ν [-]	$0.20 - 0.33$
	Volumetric strain limit for E_i change, $\varepsilon_{v\text{-limit}}$ [-]	$0.0078 - 0.086$
Visco-elasticity (VE)	Fluidity, B [s^{-1}MPa^{-1}]	$5.3\times10^{-14} - 2.1\times10^{-10}$
Visco-plasticity (VP)	Power of stress function, m [-]	$2.6 - 3.8$
	Fluidity, Γ [s^{-1}MPa^{-m}]	$3.6\times10^{-4} - 1.4\times10^{-3}$
	Softening parameter, η^*, [-]	$1\times10^{-3} - 8\times10^{-2}$
	Peak & residual adhesion parameters, a_{peak} & $a_{res.}$ [MPa]	$0.05-0.12$ & $0.03-0.12$
	Peak & residual friction parameters, δ_{peak} & $\delta_{residual}$ [^{o}]	1×10^{-4} & 1×10^{-5}

3 RESULTS

3.1 Atmospheric effect modelling

Figure 2 show in-depth (a) T and (b) RH distribution over a 5-year period for Barcelona atmospheric registry. Model results show an important variation of temperature within the first 2 meters from the domain air boundaries, followed by a 4-meter zone in which variations are visible but less pronounced. As depth increases, in-soil T appears to remain unaffected and converges to the imposed lower BC. Regarding RH, a zone of influence of 1 m can be identified at the superior boundaries in which BC modify in-soil RH values. After initial variations, in-soil RH values remain constant throughout the analysis within 99% to 100%.
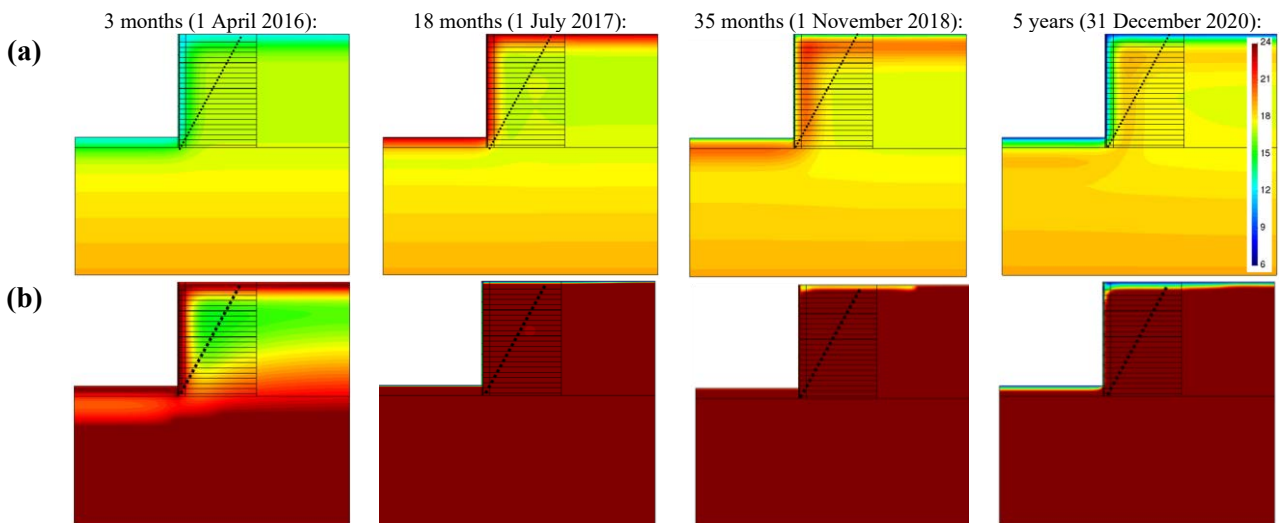
Figure 2: TH model 5-year (a) temperature (ºC) and (b) relative humidity (-) results using the Barcelona atmospheric registry.

Figure 3 shows the variation of T and RH at points A, B and C for all locations ambient air

conditions after 2 years of analysis. As depth increases, variations in T go from approximately ±6°C at point A to a stable ±3°C variation at points B and C for all but Singapore cases, which remains at a steady 28°C at all observed points. As depth increases the peaks of T and RH distribution curves are present later with respect to surface values. Mean in-soil T and RH values were 29.7°C, 17.9°C, 28.4°C, and 9.9°C and 63%, 94%, 86% and 97% for Abu Dhabi, Barcelona, Singapore, and Toronto, respectively. Results show air saturation (RH = 100%) occurs for extended periods for Barcelona and Toronto. RH tends to higher values as depth increases. The current model does not account for surface precipitation which could potentially change the in-soil T and RH distributions.

Figure 5(a) shows the temperature variation of a vertical soil profile at 4 meters from the wall facing over a 5-year period using the Barcelona registry. Results show that T changes within the first 3 meters constitute the largest fluctuations matching the prescribed BC (3°C to 30°C). From 3 to 15 meter-depth, T fluctuations diminish to ±2°C oscillations with respect to the annual mean atmospheric temperature (17°C). Below 15 meters, T stabilizes with less than ±1°C variation and approaches a constant value matching the lower BC.
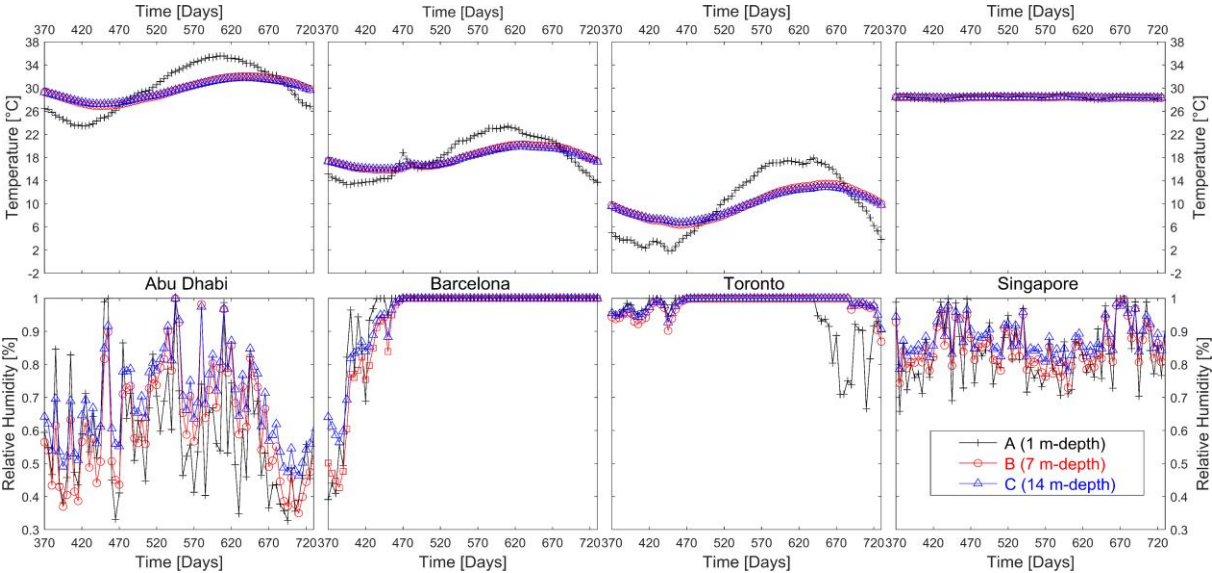
Figure 3: Evolution of temperature and relative humidity at points A, Band C for the four different locations and climates considered for year 2 of a 5-year analysis

3.2 PET strap modelling

Figure 4(a) depicts the adjustment of the proposed models with creep laboratory measurements for grade 30, 50 and 70 kN straps under loads of 66% and 70% of UTS. The adjustment is deemed adequate for both studied scenarios Figure 4(b) illustrates the influence of T on creep behavior for a grade 30 reinforcement material under 70% UTS load at constant T. Values correspond to the maximum and minimum mean values obtained using the TH models with different BC. Due to T variations, the VE and VP models update their equivalent fluidity, thus, long-term deformation varies within a range of 1-1.5% for a 19°C variation over a 50-year period. By including a linear expansive model, an initial change in temperature (from 20°C to 10°C or 20°C to 29°C), followed by a constant temperature modelling, shifts the creep curve to higher or lower deformation for increasing or decreasing temperatures, respectively.

Figure 5(b) presents horizontal displacements of the deformed mesh for a 1-year analysis

period using Barcelona atmospheric BC with the bi-linear elastic and VE PET strap model together with linear elastic concrete and backfill materials. Since the analysis is limited to one year, no significant variations were observed between different BC cases. When comparing linear elastic and VE model results, the maximum displacement increases by about 4% over a 1-year period for the VE model.
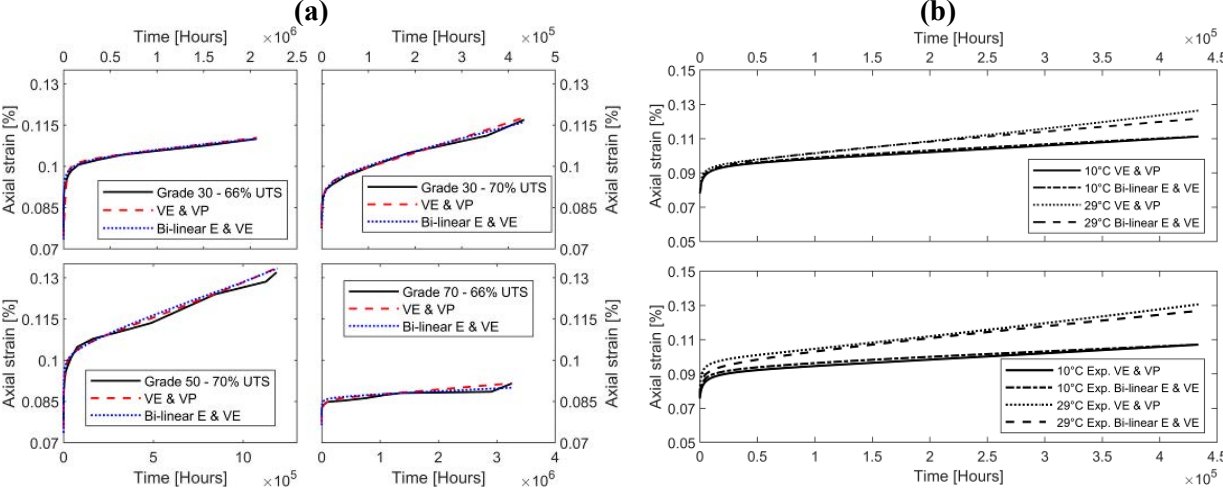
Figure 4: (a) Long-term deformation model results for grades 30, 50 and 70 kN at 66 or 70% of UTS load compared to accelerated laboratory creep tests, and (b) creep behavior changes due to temperature variations from 20°C to 10°C or 29°C for a grade 30 strap at 70% UTS load.
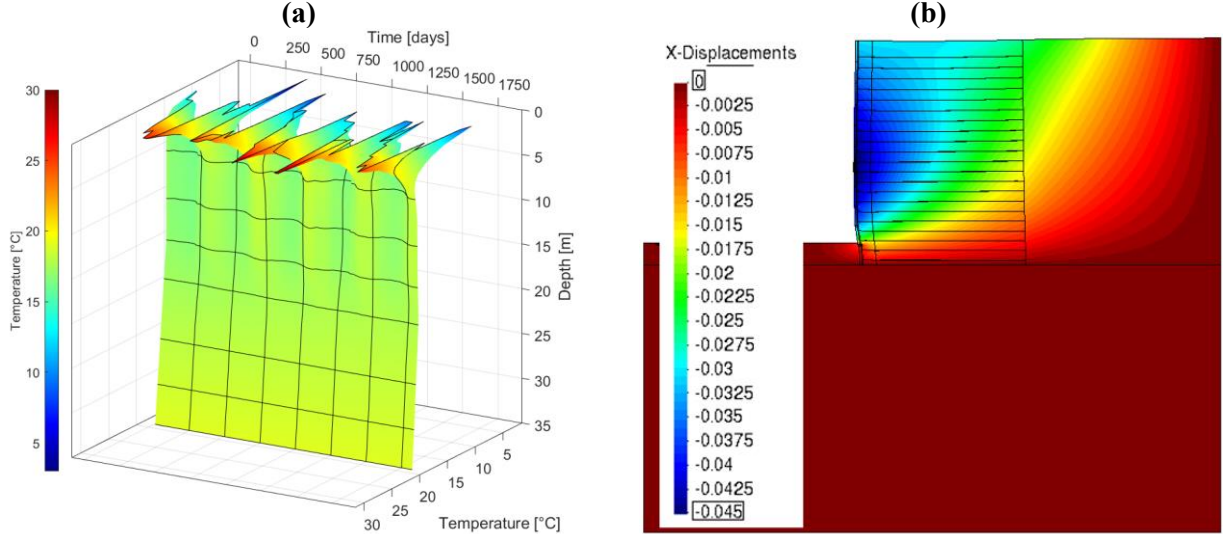
Figure 5. (a) In-soil temperature distribution over a 5-year period using Barcelona climate data and sand backfill model, and (b) horizontal outward displacements (m) and deformed mesh (amplification factor ×10) after 1 year analysis with an elastic coupled THM model with PET straps reinforcements (bi-linear elastic and VE model) using Barcelona 2020 atmospheric registry.

4   CONCLUSIONS

- A 2D THM model was implemented to evaluate the effects of prolonged ambient conditions on in-soil T and RH distributions on the backfill soil and long-term

behaviour of the embedded PET strap reinforcement layers used in MSE walls with different ambient environmental conditions.

- TH models gave results in accordance with previous studies [vii], [viii] for temperature distributions in-soil as a function of depth. The mean in-soil T can be approximated by the annual mean environmental (atmospheric) in-air values.
- Air saturation was achieved for extended periods for Barcelona and Toronto climate registry cases, with mean values of 94% and 97%, respectively. For desert conditions (Abu Dhabi), air saturation was scarcely observed (mean RH = 63%). Tropical conditions (Singapore) resulted in an almost constant RH = 86% with sporadic peaks of 100%.
- VE and VP models were fitted to creep master curves with satisfactory results for different grades of PET straps and UTS loads, incorporating T dependencies.

ACKNOWLEDGEMENTS

REFERENCES

[i] Jailloux, J.M., Nait-Ali, K.L., and Freitag, N. 2008. Exhaustive long-term study on hydrolysis of high-tenacity polyester–10-year results. In Proceedings of the 4th European Geosynthetics Conference, Edinburgh, UK, 6p.(CD-ROM–Paper 212).

[ii] Greenwood, J.H., Schroeder, H.F., and Voskamp, W.; 2012. Durability of Geosynthetics (Publication 243). CUR Committee C 187. Building and Infrastructure. ISBN 978-90-376-0533-4.

[iii] Olivella S, Gens A, Carrera J, Alonso E. 1996 Numerical formulation for a simulator (CODE_BRIGHT) for the coupled analysis of saline media. Engineering Computations 13(7), 87-112.

[iv] You-Kyum, K., Gyeong-Yun, S. 2018. Reliability assessment of polymeric straps (FASTEN FS) for soil reinforcement. H411-18-00067. GECO Industrial Co., Ltd. FITI Testing and Research Institute, Chungbuk, Korea.

[v] GECO 2021. GECO Industrial Co., Ltd. Gyeonggi-do, Republic of Korea. http://gecoind.com/en/product/fasten.php

[vi] WeatherOnline Ltd. Meteorological Services, viewed on March 2021, https://www.weatheronline.co.uk/

[vii] Kasozi, A.M., Siddharthan, R.V., and Mahamud, R. 2015. Temperature distribution in mechanically stabilized earth wall soil backfills for design under elevated temperature conditions. Journal of Thermal Science and Engineering Applications, 7(2).

[viii] Segrestin, P., and Jailloux, J.M. 1988. Temperature in soils and its effect on the ageing of synthetic materials. Geotex and Geomem, 7, 51-69.

NUMERICAL MODEL OF A TUNNEL EXCAVATED IN A ROCK MASS WITH CREEP BEHAVIOUR

Patricio Sanchez Farfán[*1]**, Alfonso Rodríguez Dono**[†*] **and Fei Song**[*2]

[*] Department of Civil and Environmental Engineering
Technical University of Catalonia (UPC)
Campus Nord UPC, 08034 Barcelona, Spain
[1]E-mail: patricio.sanchez@estudiantat.upc.edu
[2]E-mail : fei.song@upc.edu

[†] International Centre for Numerical Methods in Engineering (CIMNE)
Edificio C1, Campus Norte UPC
Gran Capitán s/n, 08034 Barcelona, Spain
E-mail: alfonso.rodriguez@.upc.edu

Key words: Time-dependency, Rock mechanics, Numerical validation, CODE_BRIGHT

Abstract. This investigation main focus is the simulation of the longitudinal displacement profile (LDP) obtained in the excavation of a real tunnel in a rock mass with creep behaviour, so the Burgers visco-elastic model is used to reproduce the time-dependency of the rock, also, is coupled with the perfect elastoplastic model that is recommended for low resistance rocks as is the case. The final model considers the time of excavation advances and the use of the shotcrete reinforcement in order to get closer to the real conditions in the project. For the calculation of viscous properties, a back analysis was realized considering: Maxwell, Kelvin and Burgers rheological models, it was also tried to reproduce the rock displacements considering just elastic and elastoplastic models, however, the values observed in the field could not be reached, not even reducing the resistance values below that recommended in the geotechnical characterization.

1. INTRODUCTION

A reasonable prediction of the displacements is fundamental to the design of tunnels to both in numerical and analytical methods, for that reason creep behavior can have a considerable importance in the calculation. Among all the methods in the bibliography, there is the convergence-confinement method (CCM) that allows an analytical design of the tunnel, for this purpose three characteristic curves are need: Longitudinal displacement profile (LDP), Ground Reaction Curve (GRC) and Support Characteristic Curve (SCC).

The response of the rock masses will differ depending on which model we choose to use, many researchers have studied the importance of time-dependency in rocks[123] and on these investigation we are going to simulate the LDP of a tunnel excavated in Solignano-Italia, of which we have the displacements along the time and the excavation distance from the face.

The rock presumed to have creep behavior for the shape of the LDP that shows important increments of displacement when there are no further excavations. Finally, we simulate the excavation using the Burgers rheological model, also compare with other time-dependent model and with elastic and perfect elastoplastic models.

2. CONSTITUTIVE MODEL

Most of the formulations found in the literature to solve a time dependent problem can be divided into three: analytical formulations, rheological formulations and general theory formulations.[2]

A rheological formulation development has been followed in this investigation, this consists of the use of elastic springs, viscous dampers and plastic limits, positioned in such a way that they can represent the behavior of viscous materials.

Model	Mechanical Analogue	Stress – Strain – time Relationship
Kelvin		$\varepsilon(t) = \dfrac{\sigma}{E_K}\left[1 - \exp\left(-\dfrac{E_K t}{3\eta_K}\right)\right]$
Maxwell		$\varepsilon(t) = \dfrac{\sigma}{E_M} + \dfrac{\sigma t}{3\eta_M}$
Burgers		$\varepsilon(t) = \dfrac{\sigma}{E_M} + \left[1 - exp\left(-\dfrac{E_K t}{3\eta_K}\right)\right] + \dfrac{\sigma t}{3\eta_M}$
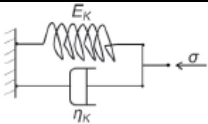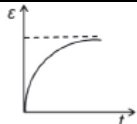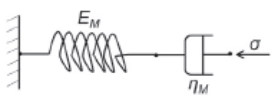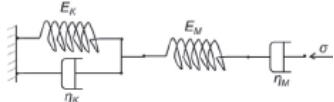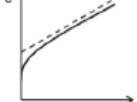
Table 1.   Rheological viscoelastic models [2]

3. DESCRIPTION OF THE IN-SITU DATA

The Marta – Giulia tunnel is an expansion of the Solignano – Osteriazza road that is located in the province of Parma, Italy. The tunnel is 4.2 km long; however, we will analyze in more detail km 0+417.50, which is located in a Flysch which has been characterized with the following range of mechanical properties shown in table 2.

The section of the tunnel is variable; however, the section studied have a radius of 6 m and a 20 cm shotcrete reinforcement.

The measurement results are displayed in figure 1, in a) is shown a graph of displacement versus time and in b) is shown a graph of displacement versus distance to the tunnel face where it can be appreciated that at a distance of approximately 16 m, there is an increase of radial displacement without any ground excavation so these may be a result of the creep behavior of the rock.

Properties	Min value	Max value	Units
Friction angle (ϕ)	34	40	°
Cohesion (c)	0.5	0.7	MPa
Elastic Modulus (E)	3000	4000	MPa
Poisson ratio (v)	0.25	0.35	-
Specific weight (γ)	2450	2550	kg/m^3
GSI	35	55	-

Table 2.   Results of the characterization of the Solignano flysch.
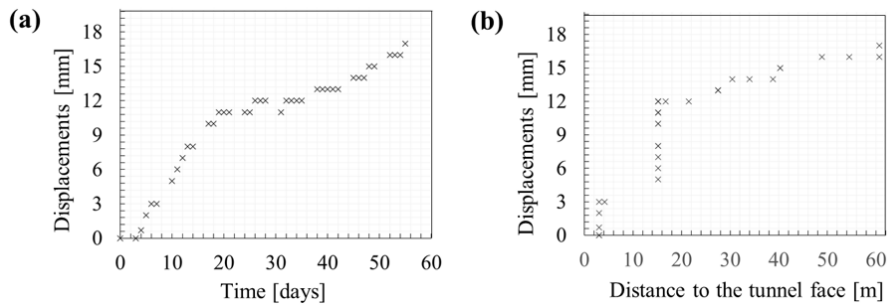
Figure 1. (a) The displacements versus time (Km. 0+417.50 section), and (b) The longitudinal deformation profile (Km. 0+417.50 section), of Solignano tunnel. Numerical simulations

4. NUMERICAL SIMULATIONS AND COMPARISONS

4.1. Numerical model

The model has been developed in 3D CODE_BRIGHT. The first consideration taken into account has been that the dimensions of the model are large enough so that they do not affect the behavior of the tunnel. Thus, the distances to the lower limit and the width of the mesh can be calculated with the Moller recommendations[4].

The boundary conditions are present on the external faces of the model, in such a way that they are restricted in the direction perpendicular to the movement, with the exception of the upper face, which is free, due to the consideration of gravity.

The model adds a part of the terrain prior to the beginning of the studied excavation and one after the end of the excavation, so that neither the beginning nor the end of the excavation is within the boundary conditions, these parts have a length of 20 meters. The position in the y-z and x-y plane of the studied key are shown in Figure 2.

The initial isotropic stresses were introduced in a linear manner, so that stress values are not available on the ground surface, while they increase to the bottom of the model as a function of the specific weight per depth.
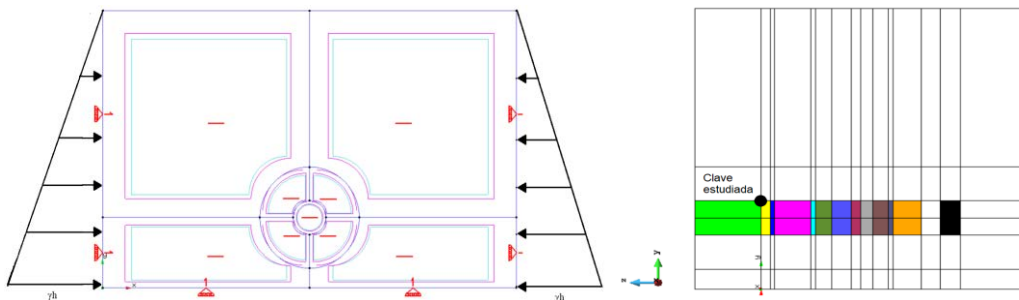
Figure 2.   Displacement versus time and advance to the tunnel face with different modulus of elasticity in an elastic model.

4.2. Parameter calibration

The geotechnical characterization measurement shows a range of results in properties, because, it is not a homogenous material, so we model the tunnel excavation trying elastic and elastoplastic, ignoring the creep behavior of the rock. As shown in Figure 3,4 the displacements are very small compared to the one that had been measured.

3
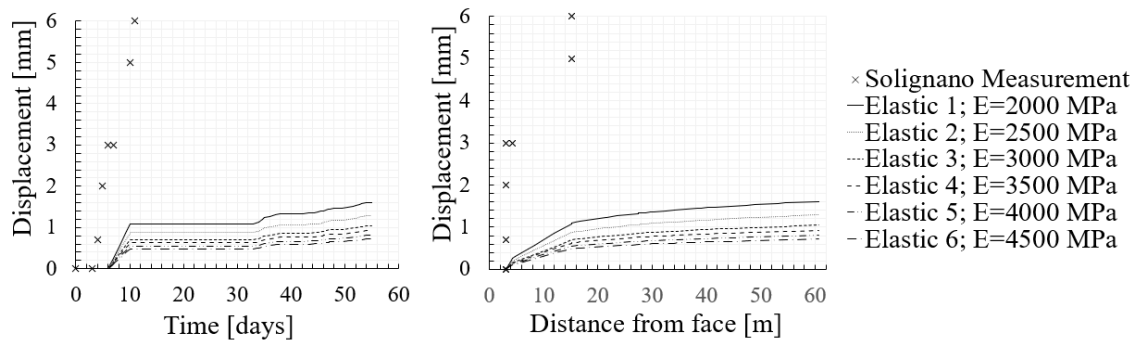
Figure 3. Displacement versus time and advance to the tunnel face with different modulus of elasticity in an elastic model.
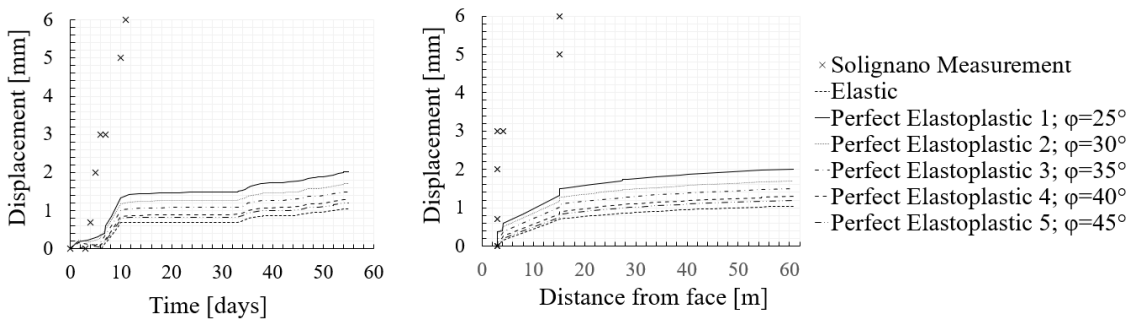
Figure 4. Displacement versus time and advance to the tunnel face with different friction angle in a perfect elastoplastic model.

The following models consider the time dependent behavior of the rock, but as we do not have laboratory values of viscosities, a back analysis was realized so it would fit the measure curve in an optimal way. Three rheological formulations were model Maxwell (Figure 5), Kelvin (Figure 6,7), Burgers (Figure 8).

In Maxwell (Figure 5) we can clearly see the linear behavior of the model in the time versus displacement graph, these will continue indefinitely, unlike in the Kelvin model (Figure 6) where the maximum displacement is limited with the Kelvin elasticity, in such a way that, with a value of 1000 MPa it can not reach the expected displacement, so in Figure 7 the Kelvin elasticity was reduced at a constant Kelvin viscosity and at 700 MPa we can achieve a similar curve. In Burgers (Figure 8) it was tried to simulate a curvy shape beginning and the a more linear form, so since Burgers is a combination of Kelvin and Maxwell, you can do back analysis to fit this.

The section of the tunnel was constructed with a 20 cm shotcrete as a reinforcement, so after modeling the different constitutive models we add this, and of course, these is perceived as a reduction of displacement. In figure 9 it appears the results of different viscosity models, after we reduced those values. The reduction of viscosity is reflected in an increment on the displacements. So finally considering a reduction of 25% of the viscosity we achieve a LDP that fits the displacements measured using the Burgers viscoelastic model, with perfect plasticity, bearing in mind, the real conditions of construction as excavation time and shotcrete reinforcement.

4
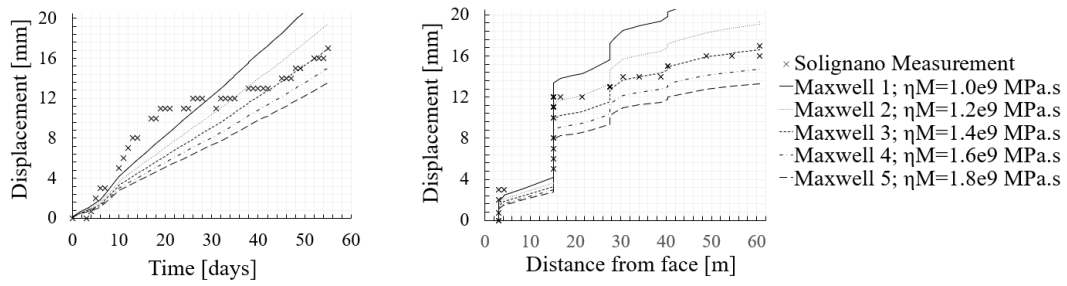
Figure 5. Displacement versus time and advance to the tunnel face with different viscosities in a Maxwell visco-elastic perfect elastoplastic model.
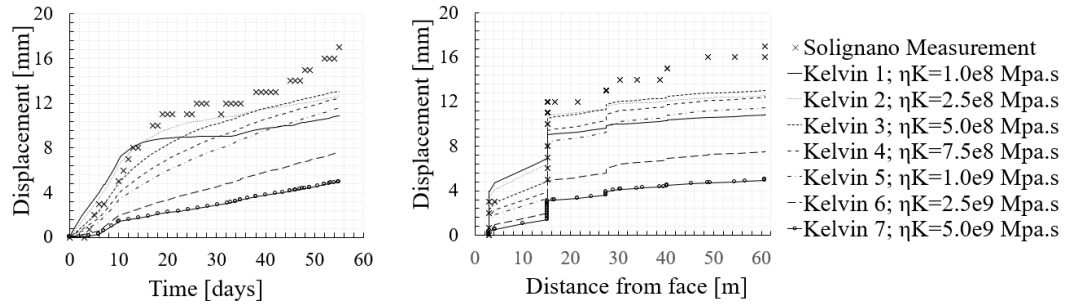
Figure 6. Displacement versus time and advance to the tunnel face with different viscosities in a Kelvin visco-elastic perfect elastoplastic model with a Kelvin elasticity modulus of 10^3 MPa
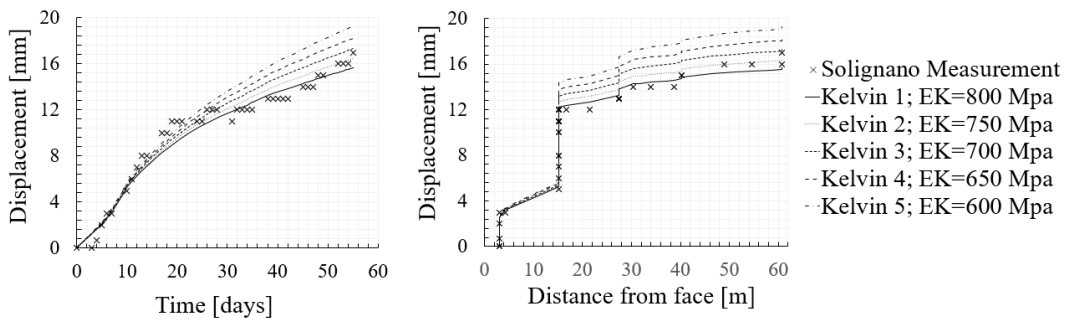
Figure 7. Displacement versus time and advance to the tunnel face with different Kelvin elasticity in a Kelvin visco-elastic perfect elastoplastic model with a Kelvin viscosity of 2.5 10^8 MPa.s
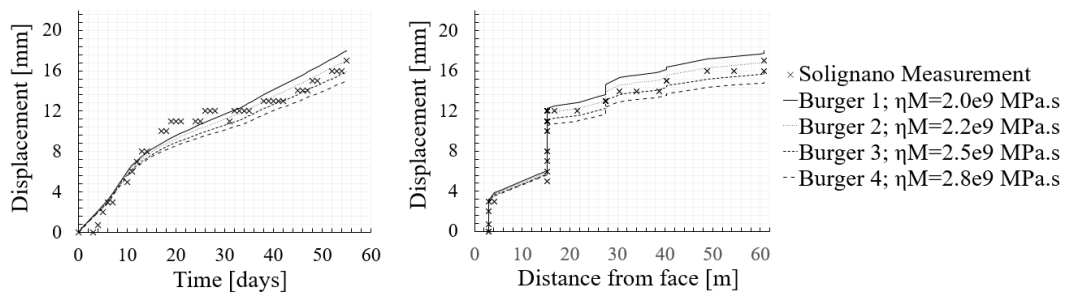
Figure 8. Displacement versus time and advance to the tunnel face with different Maxwell viscosities in a Burgers visco-elastic perfect elastoplastic model with a Kelvin elasticity modulus of 1.7 10^3 MPa and a Kelvin viscosity of 2.5 10^8 MPa.s
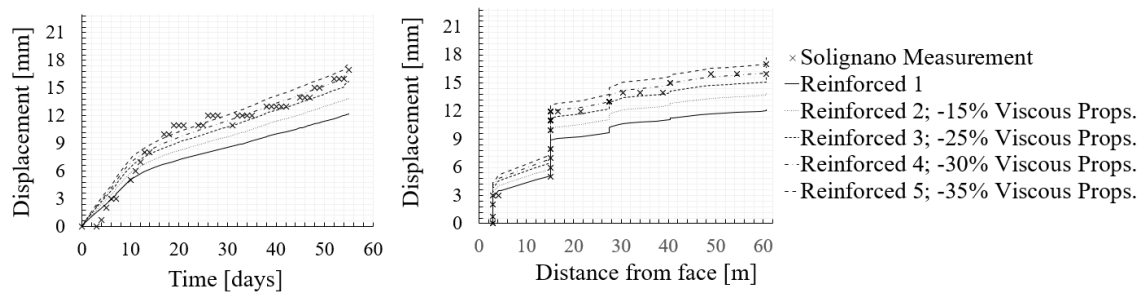
Figure 9.   Recalculation of the viscous properties considering the shotcrete reinforcement.

4.3. Numerical validation and comparisons

The numerical validation is made according to the values measured in situ, but numerically we check different meshes and in figure 10 we can see three different sizes, from the left to the right there are 49k, 160k and 286k elements in each one. In figure 11 it is appreciable that there is no huge difference between the results of each other's, 7.4% difference from b to a and 2.6% from b to c.

Also, extra measurements were taken in other sections of the tunnel so in figure 12 it is shown the difference between real and numerical behavior for the km. 0+439.95 section without changing the viscosity of the original model. The model can quite predict the displacements of a section that is almost 23 m ahead.
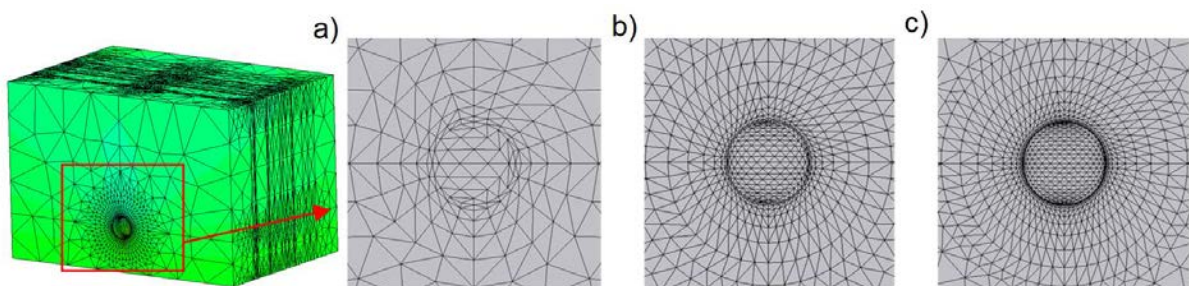
Figure 10.   Three different sizes of elements near the excavation
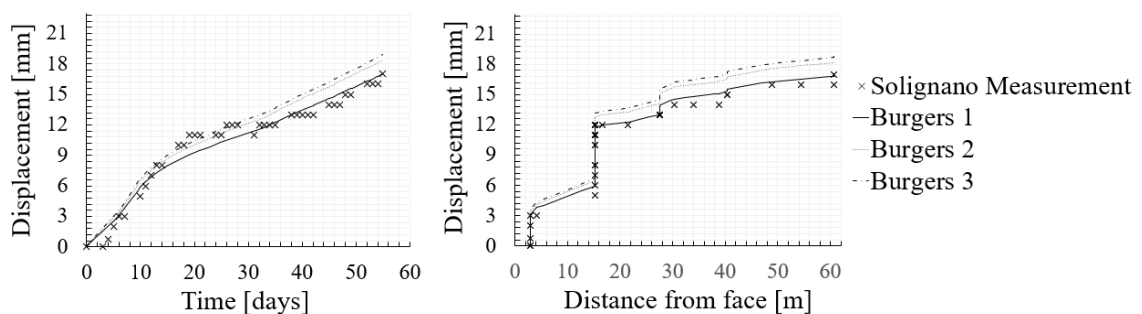
Figure 11.   Radial displacement versus distance from the face of the tunnel and time for different sizes of elements.
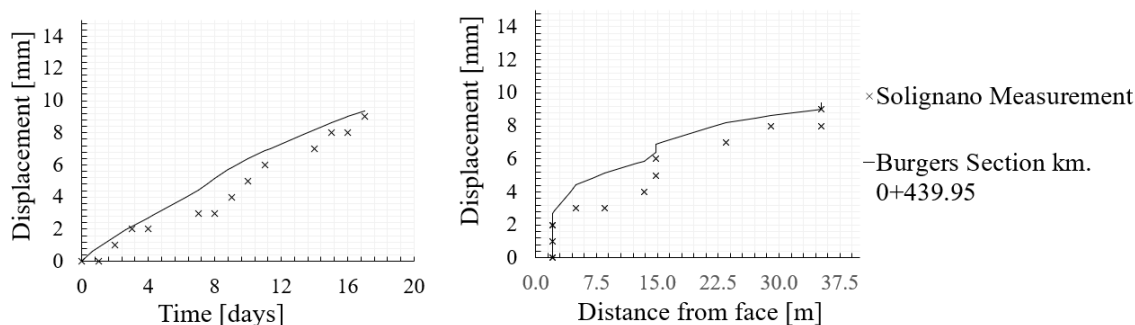
Figure 12. Radial displacement versus distance from the face of the tunnel and time for the section 0+439.95

5. CONCLUSIONS

The purpose of this work is the numerical modeling of a tunnel excavated in a rock mass with creep behavior. To obtain the viscous parameters of the model, a back-analysis has been carried out from the displacements obtained in the field. After the analysis carried out, it has been concluded that the Burgers rheological model can adequately simulate the excavation of the tunnel, obtaining similar results to the field measurements.

The first models were made considering only elastoplasticity, resulting in displacement values well below those observed in the field, even using the lowest strength and stiffness values from the geotechnical characterization report. The reason for this is that in the longitudinal deformation profile (LDP) prepared from the field data, it can be clearly observed that there are significant displacement increases even when there is no progress in the excavation, which is a clear indication of creep behavior, something that elastoplastic models cannot simulate.

For its part, in the creep model chosen, it has been observed that, among all the parameters of the material, the ones that have the greatest influence on the results are the viscous ones. This is because they are responsible for the vast majority of the total displacement, so modifying them will have a more appreciable consequence. However, the percentage of creep deformation with respect to the total will depend on each type of rock and its properties.

REFERENCES

1.   Song F, Rodriguez-Dono A, Olivella S, Zhong Z. Analysis and modelling of longitudinal deformation profiles of tunnels excavated in strain-softening time-dependent rock masses. *Comput Geotech*. 2020;125(April):103643. doi:10.1016/j.compgeo.2020.103643
2.   Paraskevopoulou C, Diederichs M. Analysis of time-dependent deformation in tunnels using the Convergence-Confinement Method. *Tunn Undergr Sp Technol*. 2018;71(November 2016):62-80. doi:10.1016/j.tust.2017.07.001
3.   Lee YK, Pietruszczak S, Zhang Q, et al. Analysis of time-dependent deformation in tunnels using the Convergence-Confinement Method. *Comput Geotech*. 2008;71(June):62-80. doi:10.1016/j.tust.2017.07.001
4.   Moller S. *Tunnel Induced Settlements and Structural Forces in Linings*.; 2006. http://www.uni-s.de/igs/content/publications/Docotral_Thesis_Sven_Moeller.pdf